UNIVERSITY OF BERGEN

Department of Physics and Technology

MASTER'S THESIS IN OCEAN TECHNOLOGY

A comparative study on the free vibration characteristics of submerged pipe structures

---

by Oskar Ask Ullestad

June 2023

Abstract

This thesis investigates the free vibration characteristics of submerged pipe-like structures using multiple added mass approaches. Traditional methods rely on constant added mass factors, which may lack accuracy for complex structures, particularly those with bends and multi-plane topology. To address this, the coupled acoustic-structural approach (CASA) is employed to verify the natural frequencies of submerged structures. The simulated CASA results are compared with experimental data for verification. Four experiments involving different geometric objects are chosen—a straight pipe, cantilever plates, a stiffened cylindrical shell, and a disk. CASA accurately predicts the first three eigenvalues compared to experimental results. It successfully simulates bending, torsional, twisting, ovality, and stretching mode shapes, with less than ten per cent differences compared to experimental results. Furthermore, various added mass approaches are investigated and compared to the CASA results. These approaches include the lumped mass, increased density, nonstructural mass, and ABAQUS/Aqua. ABAQUS and MATLAB are utilized for eigenvalue and mode shape simulations. Shell, beam, and elbow elements are employed to model the structures in the added mass approaches, while solid elements are used in the CASA models. The investigation covers a straight pipe, two single-planar jumpers, and two multi-planar jumpers.

The results indicate that adding mass to shell elements leads to inaccurate eigenvalue predictions compared to CASA. Torsional eigenvalues of the straight pipe and in-plane bending modes of single-planar jumpers cannot be correctly simulated using shell elements. However, shell elements perform well for lateral and out-of-plane bending modes. The results improve for multi-planar jumpers but still exhibit differences exceeding 16 per cent. On the other hand, adding mass with ABAQUS/Aqua to beam and elbow elements yields the most accurate results for single-planar jumpers, with differences compared to CASA below one per cent for all eigenfrequencies. For the straight pipe, it accurately predicts eigenfrequencies for both lateral bending and torsional modes. However, similar to shell elements, it encounters challenges in simulating multi-planar jumpers, accurately capturing eigenfrequencies for only one of the cases. Finally, a cost-effectiveness analysis is performed to assess the efficiency of different added mass approaches. Beam and elbow elements are thousands of times faster than CASA and several times faster than shell elements while demonstrating comparable memory usage.

Additionally, the effects of added mass on bend ovalities are examined using CASA and the nonstructural mass approach. The eigenfrequencies exhibit slight increases due to thickness changes and significant decreases when the cross-section changes.

Acknowledgment

This master's thesis has been carried out at the University of Bergen and Western Norway University of Applied Sciences. It is the results from my work in the study program Marine Constructions and Installations and ends my studies for the degree of Master of Science in Ocean Technology.

I want to thank my supervisor and associate, Dr Zhenhui Liu, for all his help and guidance during this work and for helping me understand the software. I would also like to thank Prof. Bjørn Tore Hjertaker for his advice and support throughout the working period. I appreciate the time you have spent helping me with the thesis.

Finally, I express my deepest gratitude to my family for their unwavering support throughout my academic journey. Their love, encouragement, and belief in me have been instrumental in my accomplishments. I am profoundly grateful for their constant motivation, understanding, and sacrifices they have made to provide me with a nurturing environment for learning and personal growth.

Contents

List of Figures

List of Tables

List of abbreviations

BE	Boundary Element
CASA	Coupled Acoustic-Structural Approach
EWD	Effective Water level Depth
FE	Finite Element
FFT	Fast Fourier Transform
FSI	Fluid-Structure Interaction
OD/TL	Outer Diameter to Total Length
SRJ	Subsea Rigid Jumper
VIV	Vortex-Induced Vibration

Chapter 1

Introduction

1.1 Background

The offshore industry is moving functionality from the platform to the bottom of the sea to achieve even greater productivity levels on smaller, less accessible oil and gas fields. As a result, subsea developments are the preferred solution for developing oil and gas fields in deep waters, marginal fields, and long step-out distances. These production facilities, located on the seabed, are called subsea factories. These factories use advanced technology to separate oil, gas, and water from the extracted mixture and then transport the oil and gas to the surface via pipelines.

A subsea production system has several vital components, as shown in Figure 1.1b. Manifolds connect multiple pipelines and allow the flow of oil, gas, and other fluids to be directed to and from different locations. Trees, also known as Christmas trees, are devices used to control the flow of oil and gas from the wellhead on the seafloor. Export sledges connect the subsea production system to a pipeline carrying the oil and gas to an onshore processing facility. These components are critical for offshore oil and gas production, enabling companies to safely and efficiently extract and transport valuable resources from beneath the ocean floor.

Over the years, different tie-in systems have been used to develop subsea facilities. Nowadays, subsea jumpers, shown in Figure 1.1a, are commonly used in various subsea oil and gas production systems, as explained by Kim (2015) [2]. A subsea jumper is a type of short pipe

***(a)** Typical M-shaped jumper, Li et al. (2022) [1]*

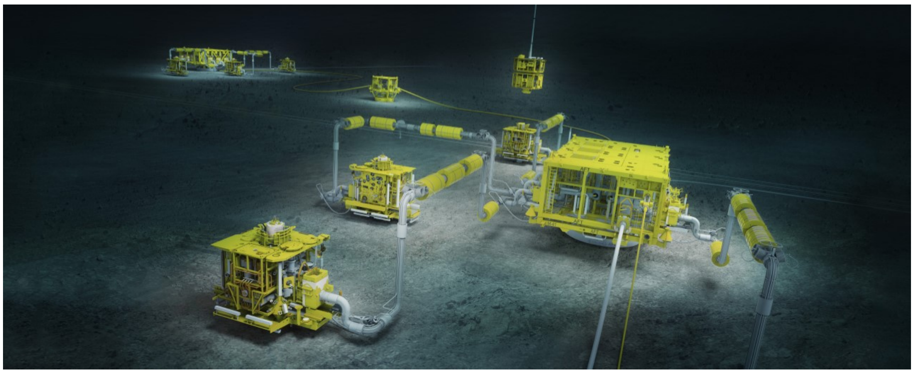

***(b)** Subsea production system connected with jumpers, by Aker Solutions AS.*

***Figure 1.1:** Subsea jumpers*

connector that transfers production fluid between two subsea components, such as a tree and manifold, manifold and manifold, or manifold and export sledge, as seen in Figure 1.1. To connect flow lines, umbilicals, and other applications in service, various horizontal and vertical tie-in systems and their corresponding connection tools are used [3].

The free vibration characteristics of subsea jumpers are essential inputs for the fatigue assessment caused by VIV (vortex-induced vibration), see Liu et al. (2019) [4]. Traditionally, the subsea jumpers are simulated by beam elements in commercial software like ANSYS, ABAQUS, or equivalents. However, it is recently found that the beam elements may incorrectly predict the free vibration modes due to the existence of bends [5]. This is a continuation of previous studies focusing on using more advanced elements, e.g., shell and acoustic elements.

Subsea jumpers are designed with bends, to accommodate potential thermal expansion, making them multi-planar structures. However, calculating their dynamic responses and free vibration characteristics can be challenging. During the manufacturing process, the bending of the straight mother pipe causes significant cross-sectional out-of-roundness at the curve centre (2.5 % ovality or higher) and wall thickness variation along the curve length (intrados wall thickening and extrados wall thinning) [6]. Ovality refers to the deviation of a cross-section from circularity, while thinning/thickening refers to the variation in thickness [7]. These changes may alter the eigenvalues and modes depending on the cross-section change. In Figure 1.2, the left picture shows an M-shaped jumper with bends (curved pipe part), and the right picture shows a jumper with mitre welds instead of bends.

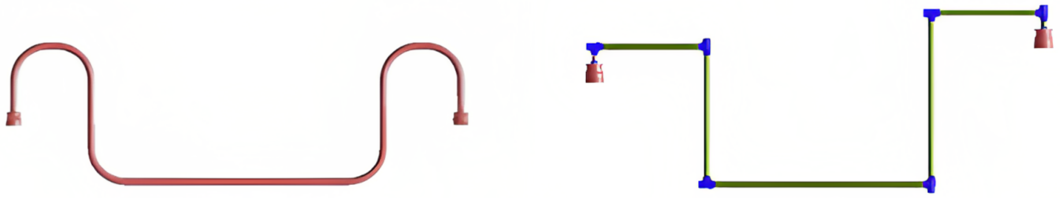

Figure 1.2: *Rigid jumper configurations, Koto (2017) [8]*

1.2 Aim and scope of the thesis

This thesis will conduct a comparative study on the free vibration characteristics of submerged pipe structures. The CASA will be used to simulate the added mass effect, which is a reliable but expensive method. The aim is to compare it with more cost-effective added mass approaches and develop a method that is as reliable as CASA but much less expensive.

This work uses beam, shell, and solid elements in the commercial software ABAQUS to produce natural frequencies and mode shapes for submerged pipe-like structures. ABAQUS [9] is used to do the simulation due to its strong flexibility in handling acoustic and structural elements. The lumped mass, nonstructural mass, increased density, and ABAQUS/Aqua approaches are performed to cost-effectively simulate the added mass effects. A solution for effective modelling will be presented with verification by comparing the results with CASA for submerged straight pipes and jumpers. Numerical models for submerged deformed bends will be investigated to understand how the added mass effects of the ovality of bends may change the eigenvalues and -modes depending on the rate of change of the cross-section.

The thesis is organized as follows: Chapter 2 presents the relevant theory and methodology. Chapter 3 presents the validation of CASA. Chapter 4 studies the added mass effects on a submerged straight pipe. Chapter 5 studies the added mass effects of the ovality of bends. Chapters 6 and 7 present two cases of single-planar and multi-planar jumpers, respectively, where different added mass approaches are studied and compared to CASA. Chapter 8 is a discussion, and the conclusions are given in chapter 9.

For each case, the structure modelling is presented first, followed by the results of the same case immediately afterwards. Mesh convergence studies are conducted on the structures in a vacuum for every case, using five mesh schemes to determine the optimal number of elements for accuracy and computational efficiency. The CASA cases involve two studies, one on the object in a vacuum and one on the acoustic elements representing the water domain. Results analysis determines the range of elements for a good balance between accuracy and efficiency. A final mesh scheme is selected based on these considerations.

1.3 Literature study

Ross (2001) has shown that the resonant frequencies of thin-walled structures decrease significantly when the structures are submerged in water, which is due to the existence of surrounding water [10]. When submerged in water, a structure's vibration is impacted by added mass, damping, and stiffness [11, 12]. Added mass refers to the mass of fluid that is accelerated by the structure's movement. Added stiffness refers to how the restoring force changes when the structure deflects. Finally, added damping is the energy that is taken from the structure by the fluid flow. It is important to note that added stiffness can typically be disregarded, but added mass and damping should be addressed as they are significant factors [13].

The idea of added mass is a way to simplify how the surrounding water affects the interaction between fluids and structures. [14, 15, 16, 17]. Blevins (2001) formulated the added mass term as a velocity potential function around vibrating structures [18]. Kramer et al. (2013) adopted Blevins's added mass term, originally formulated for analyzing the vibration of a submerged beam, to study the free vibration of submerged composite plates [19]. They used an analytical model based on composite beam and strip theory, making potential flow assumptions for the added mass. Their findings revealed that the added mass approach might not accurately predict eigenvalues for submerged plates with low aspect ratios (length/width). However, the predictions were in good agreement for plates with larger aspect ratios that resemble a beam-type geometry.

When analyzing the water effect on submerged disk and plate structures, the Raleigh-Ritz method is commonly used due to its ability to account for changes in mode shape. Using an empirical added mass formulation, Liang et al. (2001) presented a simple procedure and Rayleigh–Ritz method to analyze the vibration frequencies and mode shape of submerged cantilever plates [20]. The results were compared with Lindholm et al. (1962)'s experimental results and numerical data from pertinent literature [21]. According to that comparison, the error percentage remains nearly constant at 5 % in air and 10 % in water. Jeong et al. (2009) provided a theoretical method for a hydroelastic vibration of a clamped circular plate partially in contact with a liquid [22]. The Rayleigh-Ritz method is used to find the eigenvalue equation of the system, which helps calculate the wet natural frequencies and mode shapes for both symmetric and asymmetric modes. It was verified that the theoretical approach, based on an ideal liquid assumption and a half-liquid-contacting clamped plate, could predict the coupled natural frequencies well.

While the concept of added mass has been used to idealize the fluid-structure interaction (FSI) in numerical studies, others have adopted a more elaborate approach, namely the "coupled acoustic-structural approach" (CASA), in their numerical simulations [23]. In this approach, the coupling is a hybrid type where the oscillations of the structure act as a force on the acoustic medium, and the acoustic velocity induces oscillations on the structure. These structural acoustic models have gained significant attention in engineering and mathematical literature, see [24, 25, 26, 27, 28, 29, 30] and references therein. Analytical solutions for coupling problems are only accessible for models with simple geometries. Therefore, numerical methods are commonly used to solve practical problems involving complicated geometries and boundary conditions [31].

Rodriguez et al. (2012) used a numerical CASA model, checked its accuracy, determined its capability to predict natural frequency reduction due to nearby rigid surfaces, and compared this model against experimental data of submerged cantilever plates [32]. The researchers discovered that CASA could predict the natural frequencies of submerged structures near rigid surfaces with an average absolute error of 2.5 % in a frequency range of 0 Hz to 5000 Hz. Razi and Taheri (2014) ran numerical CASA simulations, and experimental verifications of a vibration-based damage detection strategy for health monitoring of submerged pipelines' girth-welds were presented [33]. This study used Piezoelectric transducers as both actuators and sensors to cause and measure pipe vibration. The researchers compared the results of their numerical simulations to experimental results and found that the damage detection measurements were similar in both cases. Razi and Taheri (2015) used Blevins' added mass formulation and the CASA to run numerical vibration analyses on a submerged straight pipe. The differences were limited to below 2 % in the lateral modes, whereas for the torsional mode, the differences approached 20 % [34]. The significant difference was due to the restricted assumption used in the added mass approach. Regarding the torsional mode, the pipe hardly interacts with the water around it, and its eigenvalues should be the same as if it were in the air. Although the CASA was able to replicate this accurately, the added mass approach was not successful. The Zeinoddini et al. (2012) study focused on the seismic behaviour of a free-spanning submarine pipeline [35]. They created a numerical finite-element model and tested the conventional added mass approach and the CASA method. The results showed that the simplified added mass approach was less accurate in predicting the free-spanning pipeline response than the CASA method. Zhang and Chen (2022) conducted numerical simulations using CASA to explore the impact of submerged blade disk structures' added mass effect [36]. The study discovered that different parts of the submerged blade disk structure could experience varying average added mass factors. This caused certain mode shapes, with significant blade disk interactions, to undergo significant changes when transitioning from vacuum to water, affecting the ideal design of submerged blade disk structures.

-This page is left initially blank-

Chapter 2

Theory and methodology

This chapter provides the fundamental theory of the different methods used to simulate the free vibration. The models have been developed in ABAQUS [9] and MATLAB [37]. Beam, shell and solid elements compare the eigenvalues of a submerged straight pipe, bend, and jumpers. Various added mass approaches and the CASA are being used. The main parameters used in finite elements (FE) and added mass analysis are discussed here.

2.1 Added Mass

Considering a spring-supported cylinder in a reservoir of otherwise stationary fluid, the cylinder can vibrate in the reservoir of an otherwise stationary ideal fluid. In this case, the cylinder is acted on only by the added mass force [18]. The equation of motion of the spring-supported cylinder responding to the fluid force is as follows

$$\frac{m\big(d^2X(t)\big)}{dt^2} + kX(t) = -\rho\pi r^2 \frac{dU(t)}{dt} \tag{2.1}$$

where $X(t)$ is the position of the cylinder, m is the mass per unit length, k is the spring constant per unit depth, r is the cylinder radius, $U(t)$ is stream flow, and ρ is the fluid density. Substituting $U(t) = dX/dt$, Equation (2.1) can be rearranged to give

$$(m + \rho\pi r^2)\frac{d^2X(t)}{dt^2} + kX(t) = 0 \tag{2.2}$$

In essence, the surrounding fluid imposes some extra mass onto the structure, or equivalently, the cylinder imparts part of its acceleration to the surrounding medium. The term $\rho\pi r^2$ is called the added mass, and, as shown in Blevins (2001), only applies to lateral bending for cylinders with circular or elliptic cross sections [18]. In general, added mass can be associated with the translation and rotation of a body. Blevins (1984) shows that for torsional vibration, the added mass moment of inertia is zero for objects with a circular cross-section [38].

During dynamic analysis, the effective structural mass increases due to the added mass of the fluid. The magnitude of the effect depends on the density of the fluid relative to the structure's mass. Thus, added mass is more significant in dense fluids like water rather than gases. When a rigid three-dimensional body accelerates from rest in a stationary fluid reservoir, the added mass force F_j is the total of all six rigid body accelerations' associated added mass forces

$$F_j = -\sum_{i=1}^{6} M_{ij} \frac{dU(t)}{dt} \tag{2.3}$$

where M_{ij} is the added mass matrix and i and j range over three translational orthogonal coordinates and three rotations about these coordinates. Theoretical principals show that the added mass matrix is symmetric, $M_{ij} = M_{ji}$ [39].

2.2 Finite element formulation of beam models

The jumpers can vibrate, bend, and rotate in three different dimensions. Consequently, the formulation of the beam element must also be three-dimensional, as shown in Figure 2.1.

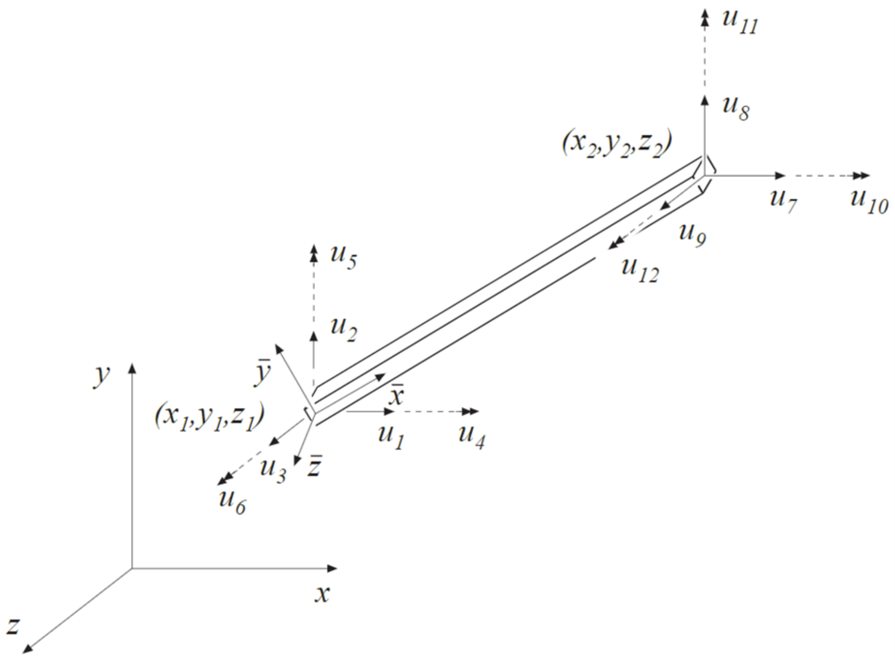

Figure 2.1: *Three-dimensional local beam element with coordinate system and nodal degrees of freedom, Lund Univerity (2022) [40]*

The pipes formulated with beam elements are assumed to be straight with a uniform cross-section capable of resisting axial forces, bending moments, and twisting moments around its centroidal axis. From Przemieniecki (1985), the stiffness axial, shearing, bending and twisting coefficients k are [41]

$$k_{axial} = \pm\frac{EI_i}{L} \tag{2.4}$$

$$k_{twist} = \pm\frac{GJ}{L} \tag{2.5}$$

$$k_{shear_1} = \pm\frac{12EI_i}{L^3(1+\Theta)} \tag{2.6}$$

$$k_{shear_2} = \pm\frac{6EI_i}{L^2(1+\Theta)} \tag{2.7}$$

$$k_{bend_1} = \pm\frac{6EI_i}{L^2(1+\Theta)} \tag{2.8}$$

$$k_{bend_2} = \pm\frac{(4+\Theta)EI_i}{L(1+\Theta)} \tag{2.9}$$

$$k_{bend_3} = \pm\frac{(2-\Theta)EI_i}{L(1+\Theta)} \tag{2.10}$$

where E is the longitudinal elasticity modulus, G is the transversal elasticity modulus, I_i is the moment of inertia on the i axis, A is the cross section area, L is the beam length, and J is the torsional inertia of the element. Θ represents the shear parameters as

$$\Theta = 24(1+\nu)\frac{A}{A_s}(\frac{r_g}{L})^2 \tag{2.11}$$

The effective shear cross-sectional area $A_s = A$ for a hollow cylinder and r_g in is the radius of gyration which can be calculated as

$$r_g = \sqrt{\frac{I_i}{A}} \tag{2.12}$$

If the ratio of the radius of gyration to element length r_g/L is small compared to unity, Θ can be assumed to be zero. Combining Equation (2.4) to Equation (2.10), the stiffness element matrix $\mathbf{K}_e$ used to estimate the eigenvalues of the pipe with 3D beam elements is shown as follows

$$\mathbf{K}_e = \begin{bmatrix} \mathbf{K_{11}} & \mathbf{K_{12}} \\ \mathbf{K_{21}} & \mathbf{K_{22}} \end{bmatrix} \tag{2.13}$$

where

$$\mathbf{K_{11}} = \begin{bmatrix} \frac{EA}{L} & 0 & 0 & 0 & 0 & 0 \\ 0 & \frac{12EI_z}{L^3(1+\Theta)} & 0 & 0 & 0 & \frac{6EI_z}{L^2(2+\Theta)} \\ 0 & 0 & \frac{12EI_y}{L^3(1+\Theta)} & 0 & \frac{6EI_y}{L^2(1+\Theta)} & 0 \\ 0 & 0 & 0 & \frac{GJ}{L} & 0 & 0 \\ 0 & 0 & \frac{-6EI_y}{L^2(1+\Theta)} & 0 & \frac{(4+\Theta)EI_y}{L(1+\Theta)} & 0 \\ 0 & \frac{6EI_z}{L^2(1+\Theta)} & 0 & 0 & 0 & \frac{(4+\Theta)EI_z}{L(1+\Theta)} \end{bmatrix} \tag{2.14}$$

$$
\mathbf{K_{21}} = \begin{bmatrix}
\frac{-EA}{L} & 0 & 0 & 0 & 0 & 0 \\
0 & \frac{-12EI_z}{L^3(1+\Theta)} & 0 & 0 & 0 & \frac{-6EI_z}{L^2(1+\Theta)} \\
0 & 0 & \frac{-12EI_y}{L^3(1+\Theta)} & 0 & \frac{6EI_y}{L^2(1+\Theta)} & 0 \\
0 & 0 & 0 & \frac{-GJ}{L} & 0 & 0 \\
0 & 0 & \frac{-6EI_y}{L^2(1+\Theta)} & 0 & \frac{(2-\Theta)EI_y}{L(1+\Theta)} & 0 \\
0 & \frac{6EI_z}{L^2(1+\Theta)} & 0 & 0 & 0 & \frac{(2-\Theta)EI_z}{L(1+\Theta)}
\end{bmatrix} \tag{2.15}
$$

$$
\mathbf{K_{22}} = \begin{bmatrix}
\frac{EA}{L} & 0 & 0 & 0 & 0 & 0 \\
0 & \frac{12EI_z}{L^3(1+\Theta)} & 0 & 0 & 0 & \frac{-6EI_z}{L^2(1+\Theta)} \\
0 & 0 & \frac{12EI_y}{L^3(1+\Theta)} & 0 & \frac{-6EI_y}{L^2(1+\Theta)} & 0 \\
0 & 0 & 0 & \frac{GJ}{L} & 0 & 0 \\
0 & 0 & \frac{6EI_y}{L^2(1+\Theta)} & 0 & \frac{(4+\Theta)EI_y}{L(1+\Theta)} & 0 \\
0 & \frac{-6EI_z}{L^2(1+\Theta)} & 0 & 0 & 0 & \frac{(4+\Theta)EI_z}{L(1+\Theta)}
\end{bmatrix} \tag{2.16}
$$

$$
\mathbf{K_{12}} = \mathbf{K_{21}}^T \tag{2.17}
$$

Following the same methodology and order used in constructing the stiffness matrix, the mass element matrix $\mathbf{M}_e$ used to estimate the eigenvalues of the pipe with 3D beam elements is given as follows, see Przemieniecki (1985) [41]

$$
\mathbf{M}_e = \rho AL \begin{bmatrix} \mathbf{M_{11}} & \mathbf{M_{12}} \\ \mathbf{M_{21}} & \mathbf{M_{22}} \end{bmatrix} \tag{2.18}
$$

where

$$
\mathbf{M_{11}} = \begin{bmatrix}
\frac{1}{3} & 0 & 0 & 0 & 0 & 0 \\
0 & \frac{13}{35} + \frac{6I_y}{5AL^2} & 0 & 0 & 0 & \frac{11L}{210} + \frac{I_y}{10AL} \\
0 & 0 & \frac{13}{35} + \frac{6I_y}{5AL^2} & 0 & -\frac{11L}{210} - \frac{I_y}{10AL} & 0 \\
0 & 0 & 0 & \frac{J_x}{3A} & 0 & 0 \\
0 & 0 & -\frac{11L}{210} - \frac{I_y}{10AL} & 0 & \frac{L^2}{105} + \frac{2I_z}{15A} & 0 \\
0 & \frac{11L}{210} + \frac{I_y}{10AL} & 0 & 0 & 0 & \frac{L^2}{105} + \frac{2I_z}{15A}
\end{bmatrix} \tag{2.19}
$$

$$\mathbf{M_{21}} = \begin{bmatrix} \frac{1}{6} & 0 & 0 & 0 & 0 & 0 \\ 0 & \frac{9}{70} - \frac{6I_z}{5AL^2} & 0 & 0 & 0 & \frac{13L}{420} - \frac{I_z}{10AL} \\ 0 & 0 & \frac{9}{70} - \frac{6I_z}{5AL^2} & 0 & -\frac{13L}{420} + \frac{I_z}{10AL} & 0 \\ 0 & 0 & 0 & \frac{J_x}{6A} & 0 & 0 \\ 0 & 0 & \frac{13L}{420} - \frac{I_z}{10AL} & 0 & -\frac{L^2}{140} - \frac{I_y}{30A} & 0 \\ 0 & -\frac{13L}{420} + \frac{I_z}{10AL} & 0 & 0 & 0 & -\frac{L^2}{140} - \frac{I_y}{30A} \end{bmatrix} \tag{2.20}$$

$$\mathbf{M_{22}} = \begin{bmatrix} \frac{1}{3} & 0 & 0 & 0 & 0 & 0 \\ 0 & \frac{13}{35} + \frac{6I_y}{5AL^2} & 0 & 0 & 0 & -\frac{11L}{210} - \frac{I_y}{10AL} \\ 0 & 0 & \frac{13}{35} + \frac{6I_y}{5AL^2} & 0 & \frac{11L}{210} + \frac{I_y}{10AL} & 0 \\ 0 & 0 & 0 & \frac{J_x}{3A} & 0 & 0 \\ 0 & 0 & \frac{11L}{210} + \frac{I_y}{10AL} & 0 & \frac{L^2}{105} + \frac{2I_z}{15A} & 0 \\ 0 & -\frac{11L}{210} - \frac{I_y}{10AL} & 0 & 0 & 0 & \frac{L^2}{105} + \frac{2I_z}{15A} \end{bmatrix} \tag{2.21}$$

$$\mathbf{M_{12}} = \mathbf{M_{21}^T} \tag{2.22}$$

where ρ is the material density.

Equation (2.13) and Equation (2.18) represent element matrices in Timoshenko beams, which apply theory for shear-dominated (or short) beams. In contrast, the Euler–Bernoulli beam theory is used to model the behaviour of flexure-dominated (or long) beams [42]. To transform Equation (2.13) and Equation (2.18) into Euler–Bernoulli element matrices, the shear parameter Θ, described in Equation (2.11), and the last terms in the mass matrix are set to zero. Euler–Bernoulli element matrices are formulated by Hidalgo (2014) [43].

In order to obtain the eigenvalues of the beam, $\mathbf{K}_e$ and $\mathbf{M}_e$ must be expressed in global coordinates. The equation of motion for free vibration becomes

$$\mathbf{M}\ddot{\mathbf{D}} + \mathbf{K}\mathbf{D} = 0 \tag{2.23}$$

where $\ddot{\mathbf{D}}$ is the acceleration vector, $\mathbf{D}$ is the displacement vector, and $\mathbf{K}$ is the total system stiffness matrix. $\mathbf{M}$ is the total system mass matrix given by

$$\mathbf{M} = \mathbf{M}_e + \mathbf{M}_{HydroD} \tag{2.24}$$

The hydrodynamic mass matrix $\mathbf{M}_{HydroD}$ is the added mass matrix from the surrounding water. The density in the hydrodynamic mass matrix can be calculated by

$$\rho_{HydroD} = \frac{m_{Tot} + m_{AddedMass}}{V_p} \tag{2.25}$$

where m_{Tot} is the total mass of the pipe, and V_p is the volume of the pipe. $m_{AddedMass}$ for a pipe is given as

$$m_{AddedMass} = \rho_f \pi \frac{D^2}{4} L_{Tot} \tag{2.26}$$

where ρ_f is the density of the surrounding fluid, L_{Tot} is the total length of the pipe

A lumped mass matrix could be used for the added mass matrix $\mathbf{M}_{Added}$. It is a diagonal matrix obtained by summing rows of the matrix in Equation (2.18) [44]. The discrete masses are chosen in such a way that the total mass of the element is preserved.

$$\mathbf{M}_{Added} = \frac{1}{2}\rho_f AL \begin{bmatrix} \mathbf{M^D_{11}} & [\mathbf{0}]_{6x6} \\ [\mathbf{0}]_{6x6} & \mathbf{M^D_{22}} \end{bmatrix} \tag{2.27}$$

where

$$\mathbf{M^D_{11}} = \begin{bmatrix} \mathbf{M^D_{1,1}} & 0 & 0 & 0 & 0 & 0 \\ 0 & \mathbf{M^D_{2,2}} & 0 & 0 & 0 & 0 \\ 0 & 0 & \mathbf{M^D_{3,3}} & 0 & 0 & 0 \\ 0 & 0 & 0 & \mathbf{M^D_{4,4}} & 0 & 0 \\ 0 & 0 & 0 & 0 & \mathbf{M^D_{5,5}} & 0 \\ 0 & 0 & 0 & 0 & 0 & \mathbf{M^D_{6,6}} \end{bmatrix} \tag{2.28}$$

$$\mathbf{M^D_{22}} = \begin{bmatrix} \mathbf{M^D_{7,7}} & 0 & 0 & 0 & 0 & 0 \\ 0 & \mathbf{M^D_{8,8}} & 0 & 0 & 0 & 0 \\ 0 & 0 & \mathbf{M^D_{9,9}} & 0 & 0 & 0 \\ 0 & 0 & 0 & \mathbf{M^D_{10,10}} & 0 & 0 \\ 0 & 0 & 0 & 0 & \mathbf{M^D_{11,11}} & 0 \\ 0 & 0 & 0 & 0 & 0 & \mathbf{M^D_{12,12}} \end{bmatrix} \tag{2.29}$$

where $\mathbf{M^D_{ii}}$ is the sum of the respected row in the matrix in Equation (2.18). Blevins (2001) showed that the added mass for lateral acceleration is equal to Equation (2.26) [18], while Blevins (1984) showed that the torsional added mass moment of inertia coefficient was equal to zero [38]. The water will have zero torsional added mass contribution on hollow cylinders. Hence the twisting moments are removed in Equation (2.27) and $\mathbf{M^D_{44}} = 0$ and $\mathbf{M^D_{1010}} = 0$.

In order to obtain a valid expression in the form of Equation (2.23), **M** and **K** have to be expressed in global coordinates. No transformation matrix is needed in a straight pipe that is modelled in only one direction. However, in a jumper, the elements are rotated relative to each other, and each local element and mass matrix must be transformed to relate to a global coordinate system. The element and mass relations are transformed into global coordinates by performing the transformations

$$\begin{aligned} \mathbf{M}_{gc}(i) &= \mathbf{T}^T\mathbf{M}(i)\mathbf{T} \\ \mathbf{K}_{gc}(i) &= \mathbf{T}^T\mathbf{K}(i)\mathbf{T} \end{aligned} \tag{2.30}$$

prior to assembly. The subscript gc indicates that the local matrices are expressed in global coordinates. The transformation matrix is given by

$$\mathbf{T} = \begin{bmatrix} \mathbf{R} & [\mathbf{0}]_{3x3} & [\mathbf{0}]_{3x3} & [\mathbf{0}]_{3x3} \\ [\mathbf{0}]_{3x3} & \mathbf{R} & [\mathbf{0}]_{3x3} & [\mathbf{0}]_{3x3} \\ [\mathbf{0}]_{3x3} & [\mathbf{0}]_{3x3} & \mathbf{R} & [\mathbf{0}]_{3x3} \\ [\mathbf{0}]_{3x3} & [\mathbf{0}]_{3x3} & [\mathbf{0}]_{3x3} & \mathbf{R} \end{bmatrix} \tag{2.31}$$

The rotation matrix **R** contains direction cosines computed as [40]

$$\mathbf{R} = \begin{bmatrix} n_{x\bar{x}} & n_{y\bar{x}} & n_{z\bar{x}} \\ n_{x\bar{y}} & n_{y\bar{y}} & n_{z\bar{y}} \\ n_{x\bar{z}} & n_{y\bar{z}} & n_{z\bar{z}} \end{bmatrix} \tag{2.32}$$

where

$$n_{x\bar{x}} = \frac{x_2 - x_1}{L_t} \tag{2.33}$$

$$n_{y\bar{x}} = \frac{y_2 - y_1}{L_t} \tag{2.34}$$

$$n_{z\bar{x}} = \frac{z_2 - z_1}{L_t} \tag{2.35}$$

$$n_{x\bar{z}} = \frac{x_{\bar{z}}}{L_{\bar{z}}} \tag{2.36}$$

$$n_{y\bar{z}} = \frac{y_{\bar{z}}}{L_{\bar{z}}} \tag{2.37}$$

$$n_{z\bar{z}} = \frac{z_{\bar{z}}}{L_{\bar{z}}} \tag{2.38}$$

$$n_{x\bar{y}} = n_{y\bar{z}} n_{z\bar{x}} - n_{z\bar{z}} n_{y\bar{x}} \tag{2.39}$$

$$n_{y\bar{y}} = n_{z\bar{z}} n_{x\bar{x}} - n_{x\bar{z}} n_{z\bar{x}} \tag{2.40}$$

$$n_{z\bar{y}} = n_{x\bar{z}} n_{y\bar{x}} - n_{y\bar{z}} n_{x\bar{x}} \tag{2.41}$$

$$L_t = \sqrt{(x_2 - x_1)^2 + (y_2 - y_1)^2 + (z_2 - z_1)^2} \tag{2.42}$$

$$L_{\bar{z}} = \sqrt{x\bar{z}^2 + y\bar{z}^2 + z\bar{z}^2} \tag{2.43}$$

The variables x_i, y_i, and z_i are the element nodal coordinates, and $(x_{\bar{z}},\ y_{\bar{z}},\ z_{\bar{z}})$ is a global vector parallel with the positive local z-axis, given in Figure 2.1. The global mass and stiffness matrices, $\mathbf{M}_{Global}$ and $\mathbf{K}_{Global}$, respectively, are then created by summing the local stiffness and mass matrices with global coordinates, $\mathbf{K_{gc}}$ and $\mathbf{M_{gc}}$, according to the direct stiffness method as follows, see Cook et al. (2002) [45]

$$\begin{aligned} \mathbf{M}_{Global}(i) &= \sum \mathbf{M}_{gc}(i) \\ \mathbf{K}_{Global}(i) &= \sum \mathbf{K}_{gc}(i) \end{aligned} \tag{2.44}$$

After the assembly process, boundary conditions can be applied by setting the relevant degrees of freedom to zero in the global stiffness matrix.

2.3 Finite element formulation of a shell element

An eight-noded curved isoparametric finite element is used to formulate the free vibration of shells. The element can be described in a coordinate system, as shown in Figure 2.2, where η and ξ are curvilinear coordinates in the shell mid-surface and ζ is the linear coordinate in the thickness direction. The shape functions N_i for the elements are given by [46]

$$N_i = \frac{1}{4}(1+\xi\xi_i)(1+\eta\eta_i)(\xi\xi_i+\eta\eta_i-1) \tag{2.45}$$

at the corner nodes, and

$$\begin{aligned} N_i &= \frac{1}{2}(1-\xi^2)+(1+\eta\eta_i), \\ N_i &= \frac{1}{2}(1+\xi\xi_i)+(1-\eta^2) \end{aligned} \tag{2.46}$$

at the middle nodes. The displacements at each node are three translations u, v, w in the directions of the local coordinates and two rotations α, β. This makes 40 degrees of freedom for each element.

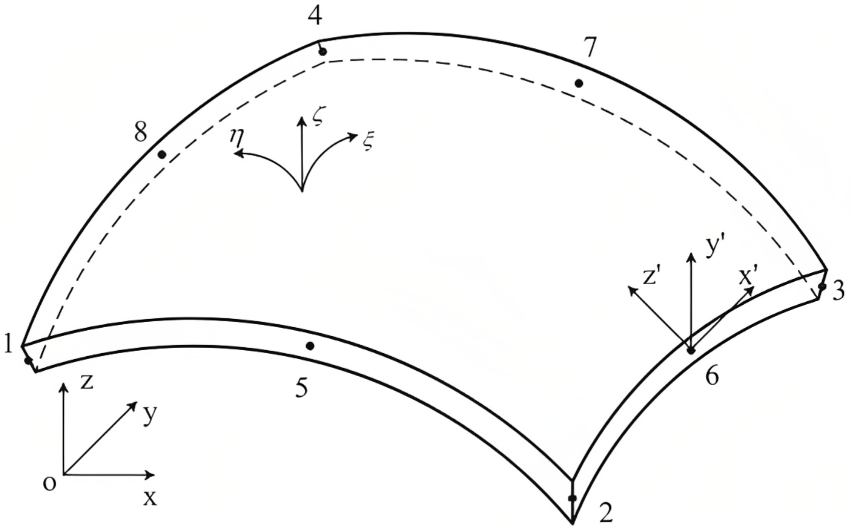

Figure 2.2: *Schematic of a curved shell element, Zhai et al. (2017) [47]*

The element stiffness matrix is calculated in two parts as

$$\mathbf{K}^e = \mathbf{K}_1^e + \mathbf{K}_2^e \tag{2.47}$$

This is due to additional matrices obtained from the strain energy similar to those given in Kumbasar and Aksu (1995) [48]. The matrices $\mathbf{K}_1^e$ and $\mathbf{K}_2^e$ represent the bending and shear effect element stiffness matrix and additional element stiffness matrix, respectively. The bending and additional terms are integrated according to the standard rule in selective reduced integration. In contrast, the shear term is integrated according to a lower-order rule [49, 50, 51].

From Zhai et al. (2017), the generalized and nodal velocity vectors are related with the help of shape functions as [47]

$$\dot{\mathbf{q}}^e = \Sigma_{i=1}^{n} \mathbf{N}\dot{\mathbf{q}}_{\mathbf{i}}{}^e \tag{2.48}$$

where $\dot{\mathbf{q}}_i^e$ is velocity components listed as:

$$\dot{\mathbf{q}}_{\mathbf{i}} = \{\dot{u}\,\dot{v}\,\dot{w}\,\dot{\alpha}\,\dot{\beta}\}^T \tag{2.49}$$

where $\dot{u}$, $\dot{v}$, and $\dot{w}$ are the tangential and normal velocity components of the middle surface, and $\dot{\alpha}$ and $\dot{\beta}$ are the rotational velocities. The kinetic energy is obtained in the matrix form as follows

$$T = \frac{1}{2}\dot{\mathbf{q}}_{\mathbf{i}}{}^{eT}\mathbf{M}^e\dot{\mathbf{q}}_{\mathbf{i}}{}^e \tag{2.50}$$

where the mass matrix of the element, $\mathbf{M}^e$ is given by

$$\mathbf{M}^e = \int_A \mathbf{N}^T\mathbf{P}\mathbf{N}dA \tag{2.51}$$

where $\mathbf{N}$ and $\mathbf{P}$ are shape and inertia function matrices, respectively. The inertia matrix is

$$\mathbf{P} = \begin{bmatrix} \rho I_1 & 0 & 0 & \rho I_2 & 0 \\ 0 & \rho I_1 & 0 & 0 & \rho I_2 \\ 0 & 0 & \rho I_1 & 0 & 0 \\ \rho I_2 & 0 & 0 & \rho I_3 & 0 \\ 0 & \rho I_2 & 0 & 0 & \rho I_3 \end{bmatrix} \tag{2.52}$$

where ρ is the mass density, I_1 is the in-plane inertia effects, and I_3 is the rotary inertia effects. I_2 is additional terms related to thickness stored outside the diagonal line. The equation of motion for one element becomes

$$\mathbf{M}^e \ddot{\mathbf{q}}_{\mathbf{i}}{}^e + \mathbf{K}^e \mathbf{q}_{\mathbf{i}}{}^e = 0 \tag{2.53}$$

Where $\ddot{\mathbf{q}}_{\mathbf{i}}{}^e$ and $\mathbf{q}_{\mathbf{i}}{}^e$ are the vectors of unknown accelerations and displacements, respectively. For the entire domain, the equation of motion is

$$\mathbf{M}\ddot{\mathbf{q}}_{\mathbf{i}} + \mathbf{K}\mathbf{q}_{\mathbf{i}} = 0 \tag{2.54}$$

The general solution of Equation (2.54), assuming harmonic motion, are

$$\mathbf{q} = \overline{\mathbf{A}} sin(\omega t + \theta) \tag{2.55}$$

where ω and $\overline{\mathbf{A}}$ are the natural frequencies and vibration modes, respectively. Substituting Equation (2.55) into Equation (2.54), the equation of motion for free vibrations can be written in the following form

$$\left(\mathbf{K} - \omega^2 \mathbf{M}\right)\overline{\mathbf{A}} = 0 \tag{2.56}$$

2.4 Elbow elements in ABAQUS

The design of piping systems heavily relies on elbows for flexibility, especially in response to thermal strains. Elbows exhibit shell-like behaviour, causing significant ovalization of the pipe cross-section and enabling elastic flexibility 5-20 times greater than straight pipes in bending [9]. Despite this understanding, the analysis of piping elbows remains challenging and costly due to the complex shell structure and severe stress gradients. Efforts to model piping elbows have included shell elements with various interpolation methods such as piecewise cubic [52] and Fourier series [53, 54]. Developments, such as implementing the classical von Karmann approach, using Fourier series for tangential displacements, and piecewise Lagrange cubic interpolation along the pipe, have shown promise in enabling detailed inelastic analysis of pipelines while balancing computational efficiency [55].

In ABAQUS, the experiences and insights have informed the development of a capability for detailed inelastic analysis of pipelines, striving for a reasonable balance between accuracy and computational cost. By leveraging the shell-like behaviour of pipe bends and considering the mild strain gradients along the pipe, the geometric modelling of elbow elements in ABAQUS optimizes the efficiency of nonlinear analysis for piping systems.

To model ovalization, it is assumed that the uniform radial expansion u^r is [9]

$$\begin{aligned} u^r = &\sum_{m=1}^{M} \overline{H}_m(S)(\overline{u}_V^r)^m \\ &+ \sum_{m=1}^{M} \sum_{p=1}^{P} \overline{H}_m(S) Q_{sym}(p\phi)(\overline{u}_I^r)_p^m \\ &+ \sum_{m=1}^{M} \sum_{p=1}^{P} \overline{H}_m(S) Q_{asym}(p\phi)(\overline{u}_0^r)_p^m \end{aligned} \tag{2.57}$$

where ϕ and S are material coordinates shown in Figure 2.3, $\overline{H}_m(S)$ is a linear polynomial interpolation function, P gives the order of Fourier interpolation, and $Q_{sym}(p\phi)$ and $Q_{asym}(p\phi)$ are

$$
\begin{aligned}
Q_{sym}(p\phi) &= \begin{cases} cos(p\phi) & \text{for } p \text{ even} \\ sin(p\phi) & \text{for } p \text{ odd} \end{cases} \\
Q_{asym}(p\phi) &= \begin{cases} sin(p\phi) & \text{for } p \text{ even} \\ cos(p\phi) & \text{for } p \text{ odd} \end{cases}
\end{aligned}
\tag{2.58}
$$

The uniform transverse expanansion u^t is

$$
\begin{aligned}
u^t = &\sum_{m=1}^{M}\sum_{p=2}^{P}\overline{H}_m(S)Q_{asym}(p\phi)(\overline{u}_I^t)_p^m \\
&+\sum_{m=1}^{M}\sum_{p=2}^{P}\overline{H}_m(S)Q_{sym}(p\phi)(\overline{u}_0^t)_p^m
\end{aligned}
\tag{2.59}
$$

and expansion for the direction **n**, γ^3 is

$$
\begin{aligned}
\gamma^3 = &\sum_{m=1}^{M}\overline{H}_m(S)(\overline{\gamma}_V^3)^m \\
&+\sum_{m=1}^{M}\sum_{p=1}^{P}\overline{H}_m(S)Q_{sym}(p\phi)(\overline{\gamma}_I^3)_p^m \\
&+\sum_{m=1}^{M}\sum_{p=1}^{P}\overline{H}_m(S)Q_{asym}(p\phi)(\overline{\gamma}_0^3)_p^m
\end{aligned}
\tag{2.60}
$$

Linear polynomials are chosen for $\overline{H}_m(S)$ to implement the formulation, referred to as element *ELBOW31*, and are the lowest order possible for such interpolation.

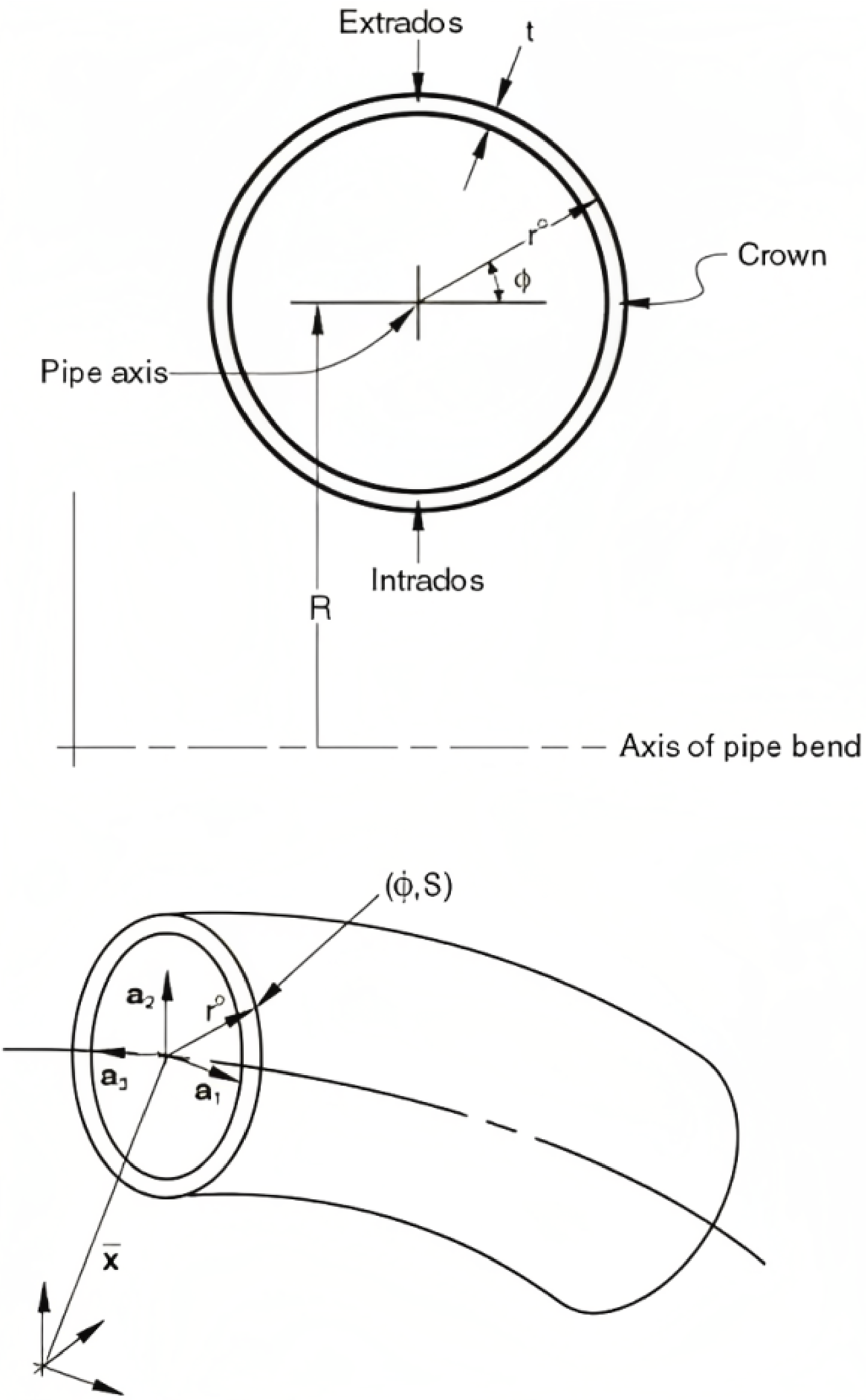

Figure 2.3: *Elbow geometry [9]*

2.5 Added mass approaches in ABAQUS

In ABAQUS, four different cost-effective approaches are tested to achieve added mass effects. It can be achieved with lumped masses (evenly distributed on the outer surface assigned to its corresponding nodes), nonstructural mass assigned to the model, increased material density, and the ABAQUS/Aqua command [9].

2.5.1 The lumped mass approach

For the lumped mass approach, point masses are created and evenly distributed on the outer surface of the model. First, a set containing all the model nodes is created. Then, using Equation (2.26), the added mass is determined and the magnitude is divided by the number of nodes and assigned to each point mass. To connect the lumped masses to the model, a tie constraint, with the nodes as slaves and the model surface as master, must be created. The point masses are then associated with the node's three translational degrees of freedom.

2.5.2 The nonstructural mass approach

A nonstructural mass contributes to the model mass from features with negligible structural stiffness [9]. It brings the net mass of the model to a known value. The nonstructural mass is spread over elements typically adjacent to the nonstructural feature and can be used on solid, shell, membrane, surface, beam, or truss elements. The nonstructural contribution affects the element mass and rotary inertia when a nonstructural mass is added to a shell or beam element with active rotational degrees of freedom. In ABAQUS, using a nonstructural mass definition to include the additional mass is generally easier than the lumped mass method. It is also more beneficial due to a higher time increment. The nonstructural feature is assumed to have no damping associated with it.

The value of the nonstructural mass is specified by using Equation (2.26). The total nonstructural mass is then distributed evenly over the region.

2.5.3 The increased density approach

The structural mass m and volume V are calculated using the model's mechanical properties and dimensions. After calculating the added mass $m_{AddedMass}$ with Equation (2.26), a new material density can be determined as in

$$\rho_{New} = \frac{m + m_{AddedMass}}{V} \tag{2.61}$$

Since ABAQUS has no built-in dimensions, ensuring that the density is given in consistent units is essential. The new structural mass is then the same as the sum of the old and added mass.

2.5.4 The ABAQUS/Aqua command approach

The ABAQUS/Aqua command is an additional feature in ABAQUS that calculates drag and buoyancy loads for offshore piping and floating platform structures [9]. It can model the effects of steady current, wave, and wind and has specific tools to analyze underwater beam-like structures subjected to water and wave loads [56]. This feature is suitable for structures that can be represented using line elements such as beam, pipe, and elbow. The added mass contribution due to distributed fluid inertia loading is

$$m_{Added} = \rho_w \frac{\pi D^2}{4} C_A \tag{2.62}$$

per unit length of the member in the directions transverse to the axis of the member-only where ρ_w is the mass density of the fluid, D is the effective outer diameter of the member, and C_A is the transverse added-mass coefficient [9].

2.6 Coupled acoustic-structural approach (CASA)

The problem of structure-fluid interaction is broad and covers many fluid forms. Suppose there are structural movements that affect and interact with the generation of pressure in a reservoir or container. In that case, it is possible to create the linearized dynamic equations of fluid behaviour around the hydrostatic state, as stated in [57].

$$\frac{\delta(\rho\mathbf{v})}{\delta t} \approx \rho_0 \frac{\delta\mathbf{v}}{\delta t} = -\nabla p + \mathbf{b} \tag{2.63}$$

where $\mathbf{v}$ is the fluid velocity, ρ is the fluid density, ρ_0 is the fluid density in the hydrostatic state, p is the pressure, $\mathbf{b}$ is the body force of gravity.

Numerical methods like the standard Galerkin discretization approach are used to solve the free vibration of a pipe in an acoustic medium. This involves applying the weak form of the fluid equation. The dynamics of the acoustic medium can be represented through this weak form as

$$\delta \prod_f = \int_{\Omega_f} \delta p \left[\frac{1}{c^2}\ddot{p} - \nabla^2 p \right] d\Omega = 0 \tag{2.64}$$

where

$$c = \sqrt{\frac{K}{\rho_0}} \tag{2.65}$$

and K is the bulk modulus of the fluid. By integrating by parts Equation (2.64) can be expanded to the following equation

$$\int_{\Omega_f} \left[\delta p \frac{1}{c^2}\ddot{p} - (\nabla\delta p)^T(\nabla p) \right] d\Omega + \int_{\Gamma_1} \delta p \rho_0 n^T \ddot{u} d\Gamma + \int_{\Gamma_3} \delta p \frac{1}{c}\dot{p}\Gamma + \int_{\Gamma_4} \delta p \frac{1}{c}\dot{p}\Gamma \tag{2.66}$$

where Ω_f is the fluid domain, Γ_i is the integral over the boundary part. In order to solve Equation (2.66) for a discrete domain, the nodal acoustic pressure and the displacement are approximated by

$$\begin{aligned} \mathbf{u} &\approx \mathbf{N}_u\tilde{\mathbf{u}} \\ p &\approx \mathbf{N}_p\tilde{\mathbf{p}} \end{aligned} \tag{2.67}$$

Where $\tilde{\mathbf{u}}$ and $\tilde{\mathbf{p}}$ are the nodal parameters of each field. $\mathbf{N}_u$ and $\mathbf{N}_p$ are appropriate shape functions. The discrete structural problem becomes

$$\mathbf{M}\ddot{\tilde{\mathbf{u}}} + \mathbf{C}\dot{\tilde{\mathbf{u}}} + \mathbf{K}\tilde{\mathbf{u}} - \mathbf{Q}\tilde{\mathbf{p}} + \mathbf{f} = \mathbf{0} \tag{2.68}$$

where the coupling term arises due to the pressures specified on the boundary as

$$\int_{\Gamma_t} \delta\mathbf{N}_u^T\bar{\mathbf{t}}d\Gamma = \mathbf{Q}\tilde{\mathbf{p}} \tag{2.69}$$

and

$$\mathbf{S}\ddot{\tilde{\mathbf{p}}} + \tilde{\mathbf{C}}\dot{\tilde{\mathbf{p}}} + \mathbf{H}\tilde{\mathbf{p}} + \rho_f\mathbf{Q}^T\ddot{\tilde{\mathbf{u}}} = \mathbf{0} \tag{2.70}$$

where

$$\begin{aligned} \mathbf{Q} &= \int_{\Gamma_t} \delta\mathbf{N}_u^T\mathbf{n}\mathbf{N}_p d\Gamma n \\ \mathbf{S} &= \int_{\Omega_f} \mathbf{N}_p^T\frac{1}{C^2}\mathbf{N}_p d\Omega \\ \tilde{\mathbf{C}} &= \int_{\Gamma_f} \mathbf{N}_p^T\frac{1}{C}\mathbf{N}_p d\Gamma \\ \mathbf{H} &= \int_{\Omega_f} \left(\nabla\mathbf{N}_p\right)^T\nabla\mathbf{N}_p d\Omega \end{aligned} \tag{2.71}$$

Matrices could then represent the free vibration of the coupled system. If free vibrations are considered, and all force and damping terms are omitted, the two equations Equation (2.68) and Equation (2.70) can be set as

$$\begin{bmatrix} \mathbf{M} & \mathbf{0} \\ \rho_0\mathbf{Q}^\mathbf{T} & \mathbf{S} \end{bmatrix} \begin{bmatrix} \ddot{\tilde{\mathbf{u}}} \\ \ddot{\tilde{\mathbf{p}}} \end{bmatrix} + \begin{bmatrix} \mathbf{K} & -\mathbf{Q} \\ \mathbf{0} & \mathbf{H} \end{bmatrix} \begin{bmatrix} \tilde{\mathbf{u}} \\ \tilde{\mathbf{p}} \end{bmatrix} = \mathbf{0} \tag{2.72}$$

The problem above is comparable to the one that arises in the vibration of rotating solids. Fortunately, there are available solution methods. Ohayon proposed a straightforward method to achieve the objective of symmetrization by implementing $\tilde{\mathbf{u}} = \breve{\mathbf{u}}e^{-i\omega t}$, $\tilde{\mathbf{p}} = \breve{\mathbf{p}}e^{-i\omega t}$ and rewriting Equation (2.72) as [58]

$$\begin{aligned} \mathbf{K}\breve{\mathbf{u}} - \mathbf{Q}\tilde{\mathbf{p}} - \omega^2\mathbf{M}\breve{\mathbf{u}} = \mathbf{0} \\ \mathbf{H}\tilde{\mathbf{p}} - \omega^2\mathbf{S}\tilde{\mathbf{p}} - \omega^2\rho_0\mathbf{Q}^{\mathbf{T}}\breve{\mathbf{u}} = \mathbf{0} \end{aligned} \tag{2.73}$$

and an additional variable $\breve{\mathbf{q}}$ such that

$$\breve{\mathbf{p}} = \omega\breve{\mathbf{q}} \tag{2.74}$$

After some substitution and manipulation, the new system can be written as

$$\left(\begin{bmatrix} \mathbf{K} & \mathbf{0} & \mathbf{0} \\ \mathbf{0} & \frac{1}{\rho_0}\mathbf{S} & \mathbf{0} \\ \mathbf{0} & \mathbf{0} & \mathbf{0} \end{bmatrix} - \omega^2 \begin{bmatrix} \mathbf{M} & \mathbf{0} & \mathbf{Q} \\ \mathbf{0} & \mathbf{0} & \frac{1}{\rho_0}\mathbf{S} \\ \mathbf{Q}^T & \frac{1}{\rho_0}\mathbf{S}^T & -\frac{1}{\rho_0}\mathbf{H} \end{bmatrix}\right) \begin{pmatrix} \breve{\mathbf{u}} \\ \breve{\mathbf{p}} \\ \breve{\mathbf{q}} \end{pmatrix} = \mathbf{0} \tag{2.75}$$

Which is a symmetric generalized eigenvalue problem.

Chapter 3

Validations of CASA

This chapter tries to evaluate the CASA in modal analysis comprehensively. ABAQUS is used to do the simulation due to its strong flexibility in handling the interface between acoustic and structural elements [9]. Four experiments have been analyzed, and the results are summarized and discussed [59].

3.1 Submerged straight pipe

Razi and Taheri (2014) presented numerical simulations and experimental verification of a vibration-based damage detection technique [33]. Before beginning the damage detection process, an experimental study was conducted in a laboratory tank to confirm the accuracy of the numerical model. Soft elastic ropes, mimicking a free-free boundary condition, were used to suspend an aluminium pipe in the tank. A chirp signal was propagated along the line using a piezoelectric transducer, and the pipe's vibration was recorded by another piezoelectric sensor, producing a voltage signal. The numerical model used was CASA, and the pipe's forced vibration signals from both the experiment and model were analyzed using a fast Fourier transform (FFT) to determine the submerged line's eigenvalues.

The straight pipe is modelled with 22000 linear hexahedral elements of type C3D8 (An 8-node linear brick [9]) and 33132 nodes. The translational degrees of freedom of the elements at both ends of the pipe are restrained to account for a clamped-clamped boundary condition. Table 3.1 shows the pipe's mechanical properties and dimensions.

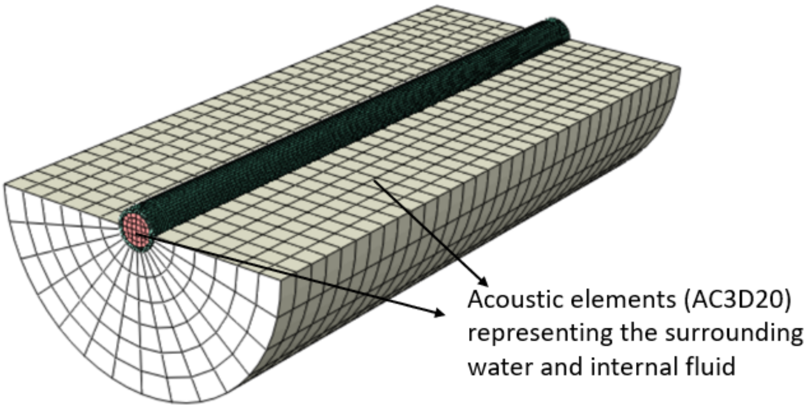

Figure 3.1: *Finite element model of the submerged straight pipe*

Table 3.1: *Mechanical properties and dimensions for the aluminium pipe*

Properties	Value	Unit
Elastic modulus	68.9	GPa
Density	2700	kg/m^3
Poisson's ratio	0.3	-
Length	1.0	m
Outer diameter	60.0	mm
Wall thickness	5.2	mm

ABAQUS's acoustic element, *AC3D20* (A 20-node quadratic acoustic brick), is used to model the water. The surrounding medium and internal fluid are modelled with 5544 elements with 25508 nodes and 3200 elements with 4141 nodes, respectively, as shown in Figure 3.1. Water's density and bulk modulus values are 997 kg/m^3 and 2.13 GPa, respectively. A radiation boundary condition is used as an exterior boundary of the water to establish an effective water level depth (EWD). A radiation boundary condition is chosen instead of a rigid wall so the acoustic waves will not reflect into the acoustic domain after they hit the rigid-wall boundary. The EWD (the outer radius of the simulated water) is equal to four times the outer diameter of the pipe, based on the results from Razi and Taheri (2014) [33].

For the other cases, the density and bulk modulus of the fluid are 1000 kg/m^3 and 2.13 GPa, respectively. A surface-based tie constraint is implemented in the interface region in the model to simulate the coupling between the object and water. This constraint correlated the object's outer surface nodal displacements with the neighbouring water elements' pressure degrees of freedom. In addition, a radiation boundary is employed for the water domain boundary, with varying EWD values.

The first three eigenvalues of the submerged straight pipe are obtained via the simulated CASA and experimental approach and compared in Table 3.2. A reasonable agreement between the experimental and numerical results confirms the integrity of the CASA model when used on a straight pipe.

Table 3.2: *Eigenvalues of the submerged straight pipe.*

Mode	CASA [Hz]	Experimental [Hz]	% Difference
1	198.5	200.0	1
2	526.6	542.8	3
3	983.7	1030.6	5

In Table 3.2, all the first three eigenmodes correspond to bending modes. In these modes, the pipe exchange energy with the surrounding, making the added mass effects obvious. CASA correctly simulates the mode shape order with reasonably predicted eigenfrequencies.

3.2 Submerged cantilever plates

Lindholm et al. (1962) examined the vibration of cantilever plates in the air and water [21]. The researchers tested fifteen submerged cantilever plates with varying plate aspect and thickness ratios. They compared the results with theoretical predictions using simple beam and thin-plate theories. To account for added mass, an empirical correction factor was included in both theories, based on chordwise hydrodynamic strip theory [60]. The natural frequencies of the first six modes were presented. Liang et al. (2001) used an empirical added mass formulation and Rayleigh-Ritz method to analyze submerged cantilever plates' vibration frequencies and mode shape [20]. Their numerical results were compared with Lindholm's experimental results and literature in air and water, revealing an error percentage of around 5 % in air and 10 % in water.

Four of the fifteen submerged cantilever plates, as in Figure 3.2, are chosen to test the CASA model. The plates are modelled with *C3D20* elements (A 20-node quadratic brick with reduced integration [9]). The four chosen plates have the same width $b = 0.2032$ m, with aspect ratios a/b values of 5, 1, 3, and 2, and thickness ratios h/b values of 0.124, 0.0238, 0.0131, and 0.009, respectively. The finite model of the first plate can be seen in Figure 3.3, and the mechanical properties can be seen in Table 3.3.

Table 3.3: *Mechanical properties for the cantilever plates*

Mechanical Properties	Value	Unit
Elastic modulus	207	GPa
Density	7800	kg/m^3
Poisson's ratio	0.3	-

To determine the required level of solid domain mesh refinement, the three mesh parameters, n_x, n_y, and n_z in Figure 3.3, are systematically varied for a dry case, comparing the results with the experimental air results obtained by [21]. An approximate global seed size for the plates of 0.01 m gave accurate dry results in all four cases. A large water domain, according to Kramer et al. (2013), is chosen to simulate the four cantilever plates in this study [19]. The mesh parameters x_B/L, y_B/L, and z_B/L became 0.5, 0.5 and 1.3, respectively. The water domain's approximate global seed size is 0.05 m with quadratic hexahedral elements of type

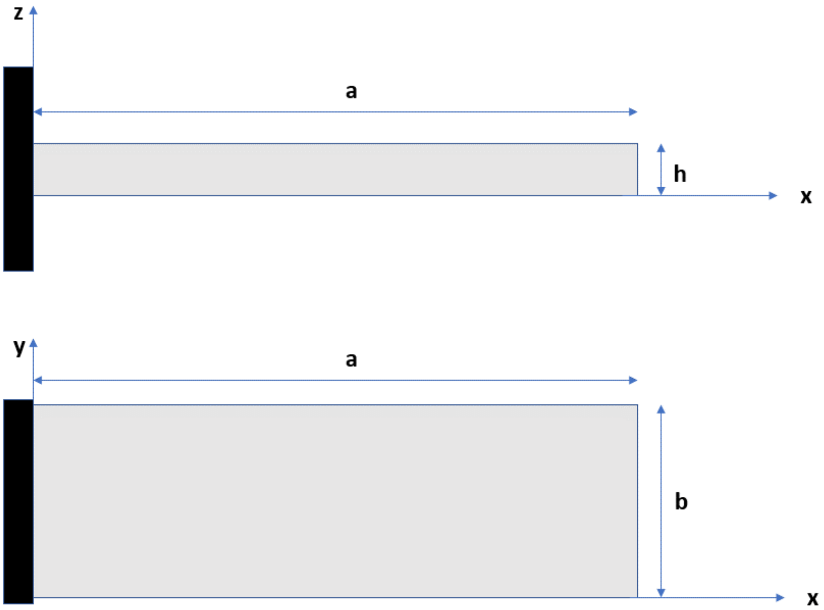

Figure 3.2: *Geometry configuration of submerged cantilever plate*

AC3D20. Table 3.4 shows the number of elements and nodes that simulate the water and cantilever plates.

Table 3.4: *Amount of elements and nodes used to simulate the four cantilever plates and water*

			Plate		Water	
No	a/b	h/b [$\cdot 10^2$]	Elements	Nodes	Elements	Nodes
1	5	12.4	6120	31949	39204	168123
2	1	2.4	400	3003	400	2253
3	3	1.3	1220	8948	8472	38233
4	2	0.9	820	6048	2816	13429

Table 3.5 shows that for cantilevers with high aspect ratios, the CASA model can capture results with an error percentage that remains nearly constant at 6 % for the first eigenmode and between 0.5 % and 3 % for eigenmodes two and three in water compared to Lindholm's experimental results. For the shorter plates, the error percentages are between 5 % and 7 % for all modes. According to Liang et al. (2001), the natural frequencies of all modes decrease with an increasing aspect ratio [20]. The eigenmodes are presented in Figure 3.4. The first three eigenmodes are bending and twisting modes. Compared to the modes of the straight pipe, all the first three eigenmodes of the cantilever plates exchange energy with the surrounding water, showing that CASA can predict the first and most necessary eigenvalues.

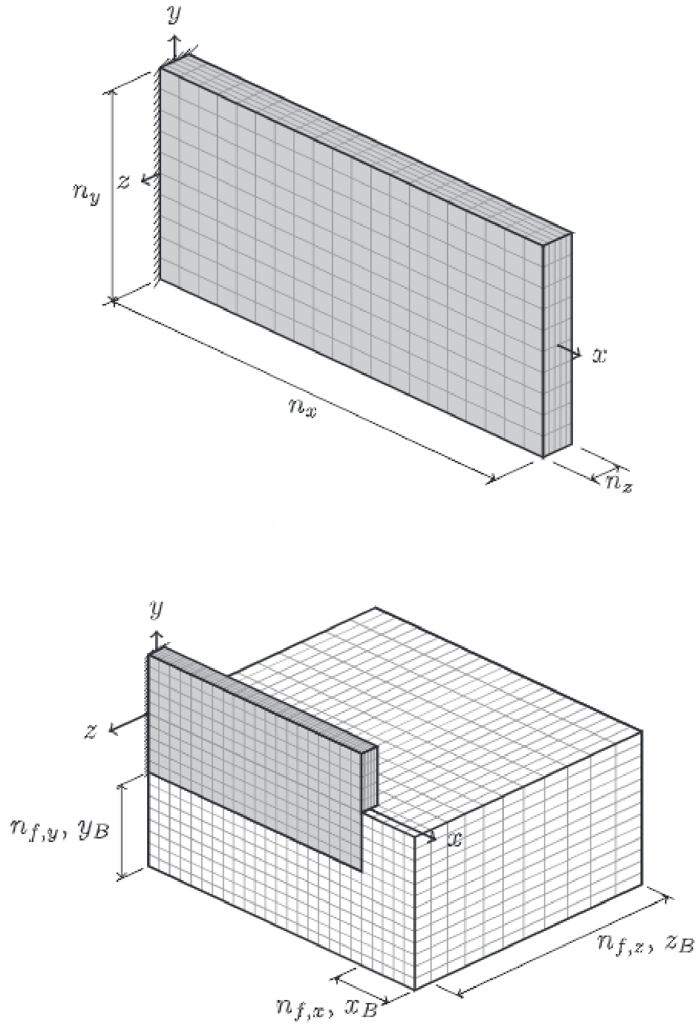

Figure 3.3: *Solid domain (grey) plus 1/4 of the fluid domain (white) not to scale, illustration from Kramer et al. (2012) [19]*

Table 3.5: *Comparison of CASA results with experimental results from Lindholm et al. (1962) of the four cantilever plates [21]*

			Mode 1 [Hz]		Mode 2 [Hz]		Mode 3 [Hz]	
No	a/b	h/b [$\cdot 10^2$]	CASA	Exp	CASA	Exp	CASA	Exp
1	5	12.4	15.6	14.6	171.0	166.0	98.3	96.0
2	1	2.4	55.2	51.4	163.0	154.0	373.0	355.0
3	3	1.3	2.1	2.3	19.8	20.6	14.6	15.4
4	2	0.9	3.4	3.1	20.0	18.8	22.7	21.1

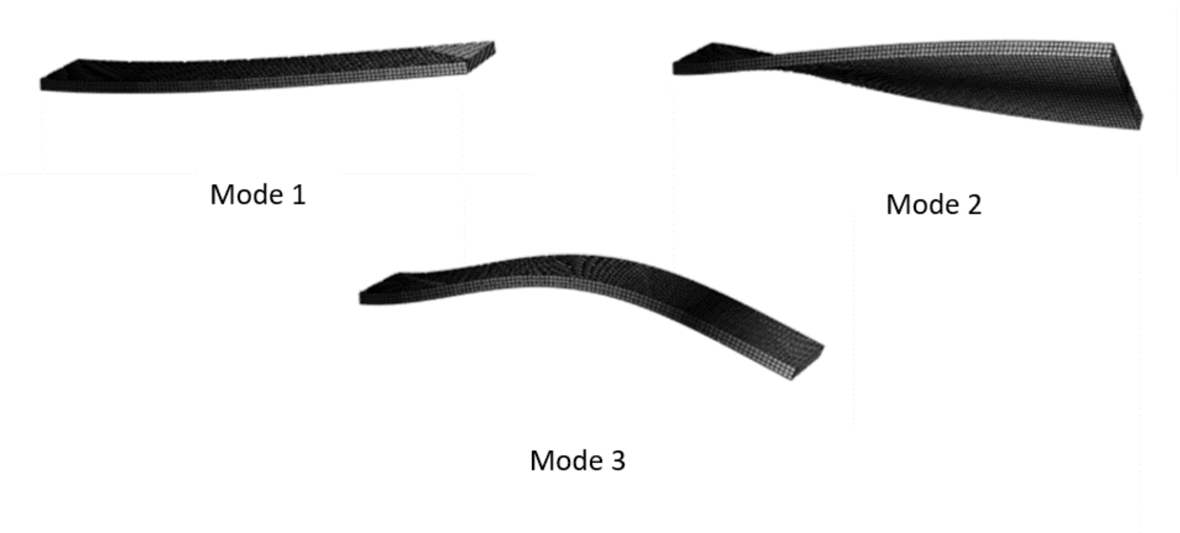

Figure 3.4: *First three modes of submerged cantilever plates*

3.3 Submerged cylindrical shell

Gao et al. (2022) measured the underwater vibration and sound radiation of a typical stiffened cylindrical shell structure under broadband excitation [61]. The test results were compared with those obtained from the numerical finite element/boundary element (FE/BE) coupling method to ensure accurate results. The established testing procedures and operation steps effectively controlled an underwater vehicle's vibration and sound radiation. The results revealed that the test results curve aligned well with the FE/BE coupling method results, with only slight differences in acceleration and sound pressure at the resonance peak value in the 500-2500 Hz band between the experimental and numerical results.

The general FE/BE method is adopted in the experiment to determine the stiffened cylindrical shell's vibroacoustic characteristics. The FE and BE model are shown in Figure 3.5 [61]. In the CASA model, the cylindrical shell assembly is identical as in Figure 3.5b. The EWD is set to four times the outer diameter of the cylindrical shell, with an approximate global mesh size of 0.02. This produced a total number of elements and nodes of 102976 and 147828, respectively. Water must be simulated at the ends because the cylindrical shell has closed ends and is not open like a pipe. With the same approximate mesh size, 3440 elements and 5604 nodes are produced for the sides.

In Figure 3.5a, the apparatus is placed 50 mm away from the centre line of the cylindrical shell, and the stiffener sections are (80 x 10) mm with 450 mm spacing. To balance gravity and buoyancy in the experiment, a 1400 kg iron ballast was connected at the bottom of the cylindrical shell with rings and wires [61]. This created a simulation quality of 900 kg, which is reached by setting the steel density to 10100 kg/m^3. Table 3.6 shows the material properties and the dimensions. For the cylindrical shell, a total of 19180 quadratic hexahedral elements of type *C3D20* and 10360 quadratic wedge elements of type *C3D15* are used to minimize errors in the mesh. This produced 154850 nodes. *C3D15* is a 15-node quadratic triangular prism and is often used together with hexahedrons when the geometry is too complicated to fill with hex elements only [9].

Finite element model

Boundary element model

Figure 3.5: *The finite and boundary element model of the cylindrical shell, Gao et al. (2022) [61]*

Table 3.6: *Mechanical properties and dimensions for the stiffened cylindrical shell*

Mechanical Properties	Value	Unit
Elastic modulus	210.0	GPa
Density	10.1	t/m^3
Poisson’s ratio	0.3	-
Length	1.8	m
Radius	0.6	m
Wall thickness	10.0	mm

Figure 3.6 shows six eigenmodes of the submerged stiffened cylindrical shell from Gao et al. (2022) [61]. The first, third, fourth and fifth modes all concern ovalities in the cylindrical shell.

The second and sixth are stretching modes. The vibration modes of the stiffened cylindrical shell determine its vibration form and distribution of radiation sound pressure under the excitation force of the corresponding frequency [61]. Table 3.7 shows the simulated CASA results compared to the results from Gao et al. (2022) [61]. Although their results were also obtained numerically, it was concluded that the test results were in good agreement with those obtained by FE/BE coupling method. Due to the existence of ring-stiffeners, the stiffness of the whole structure enhances, which also changes the stiffness of local structures, making axial modes more likely to appear. Even though none of the modes are bending, twisting or torsional modes, the CASA model simulated accurate results for all the first six eigenmodes.

Table 3.7: *Comparison of CASA results with experimental results from Gao et al. (2022) of the submerged stiffened cylindrical shell [61]*

mode	CASA [Hz]	FE/BE results from Gao et al. (2022) [Hz]	% Difference
1	192	178	8
2	205	210	3
3	251	257	2
4	257	266	3
5	287	282	2
6	395	395	0

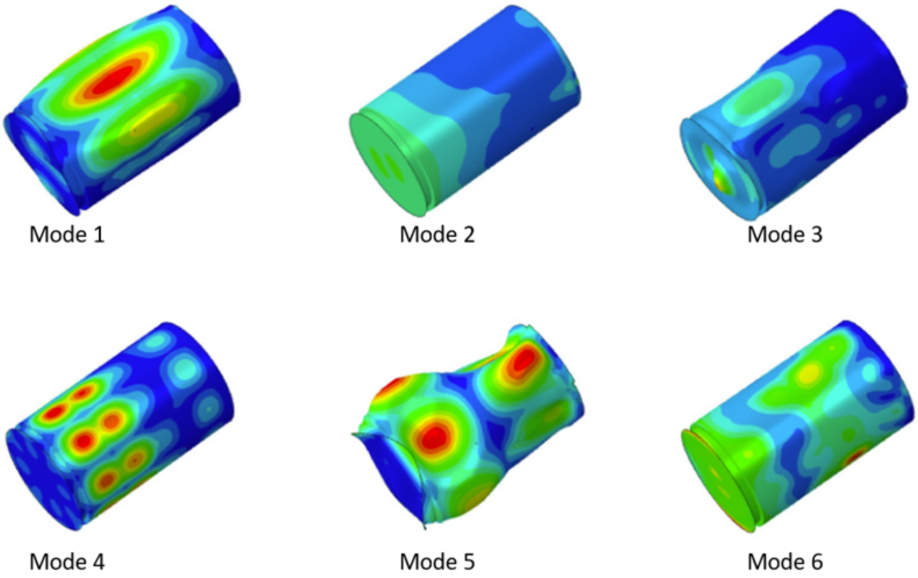

Figure 3.6: *Six mode shapes of submerged stiffened cylindrical shell, illustration from Gao et al. (2022) [61]*

3.4 Submerged disk

Valentín et al. (2017) used a test rig to comprise a stainless steel disk coupled to a shaft and confined with water in an aluminum tank [62]. The tank had a large thickness and mass to simulate rigid surfaces around the disk. The structures' response was measured using submersible accelerometers, with two installed on the disk and another two on the cover. Additionally, two pressure sensors were installed on the cover to measure pressure variations due to disk vibration. Signals from a hammer, accelerometers, and pressure sensors were computed and monitored. The disk's mode shapes were determined by first testing it in the air using the roving hammer impact method. The testing procedure in the water was practically the same as in the air.

The disk used in the test rig was a stainless steel disk coupled to a shaft and confined in water in an aluminium tank. The disk could be moved up and down along the shaft to evaluate the influence of the nearby rigid surface of the bottom surface (H_2) and top cover (H_1). The dimension and material properties are in Table 3.8.

Table 3.8: *Mechanical properties and dimensions of the submerged disk*

Properties	Value	Unit
Radius	125	mm
Thickness	3	mm
Disk density	7800	kg/m^3
Elastic modulus	207	GPa
Poisson's ratio	0.3	-

In the CASA model, the distance from the bottom surface and top cover is four times the disk diameter, $H_1 = H_2 = 0.5$ m. This becomes the EWD of the submerged disk. With an approximate global mesh size of 0.015, the water mesh produces 19765 quadratic hexahedral elements of type *AC3D20* and 402 quadratic wedge elements of type *AC3D15* for geometry purposes. This produced 86375 nodes. The disk is modelled with an approximate mesh size of 0.005, which produced 2377 quadratic quadrilateral elements of type *S8R* and 28 quadratic triangular elements of type *STRI65*. This produces 7344 nodes. The mesh for the medium with the lower wave speed should be the slave surface in a tie constraint. An exception is the case of fluids coupled to both sides of shell or beam elements. *S8R* and *STRI65* are shell elements, and the fluid is coupled to both sides, so the master and slave surfaces are appointed to the fluid and disk, respectively. The meshed model is in Figure 3.7. The disk is clamped at its centre, simulating the shaft of the experiment.

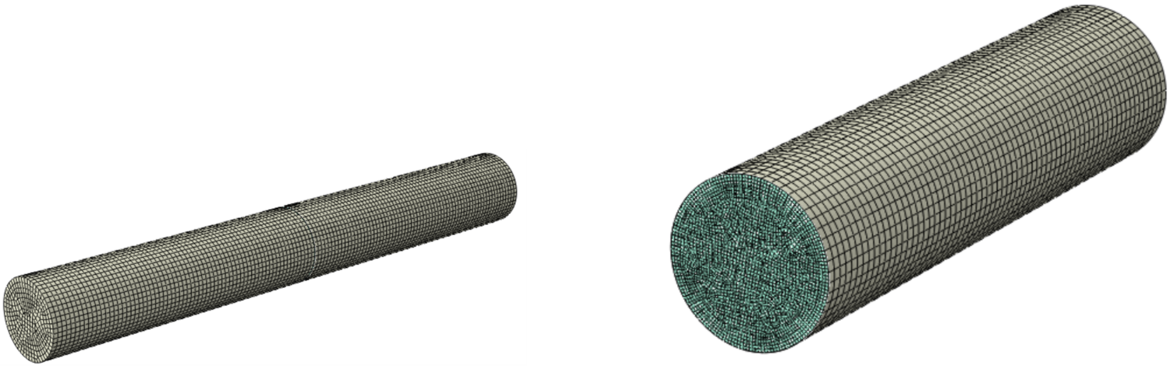

(a) The full CASA model *(b) The disk with one of the water domains*

Figure 3.7: *Visual of the meshed CASA model of the submerged disk*

The dynamic response of the submerged disk is heavily affected by the added mass and damping effects, as well as the proximity of solid boundaries. The CASA has proven in previous cases it is a trustworthy approach for simulating mode shapes where the added mass influence is large. In Valentín et al. (2017), the natural frequencies and mode shapes found within the testing frequency band were configurations where the added mass effect had less influence [62]. The mode shapes of the disk had no nodal circles ($m = 0$). The only modes Valentín et al. (2017) studied were the mode shapes with nodal diameters (n) because they were most prone to excitement [62]. $n = 0$ and $n = 1$ greatly influence boundary conditions, such as confinement and shaft displacement. Therefore modes $n = 2$ to $n = 6$ are the only ones considered. The modes can be seen in Figure 3.8.

Table 3.9: *Eigenvalues of the disk in water*

n	CASA [Hz]	Experimental [Hz]	% Difference
2	116	145	20
3	304	310	2
4	577	580	1
5	938	900	4
6	1386	1390	0

Table 3.9 shows the CASA and experimental results for the disk in water. The experimental

results were obtained by force applied by the hammer with $H_1 = 47$ mm and $H_2 = 60$ mm [62].

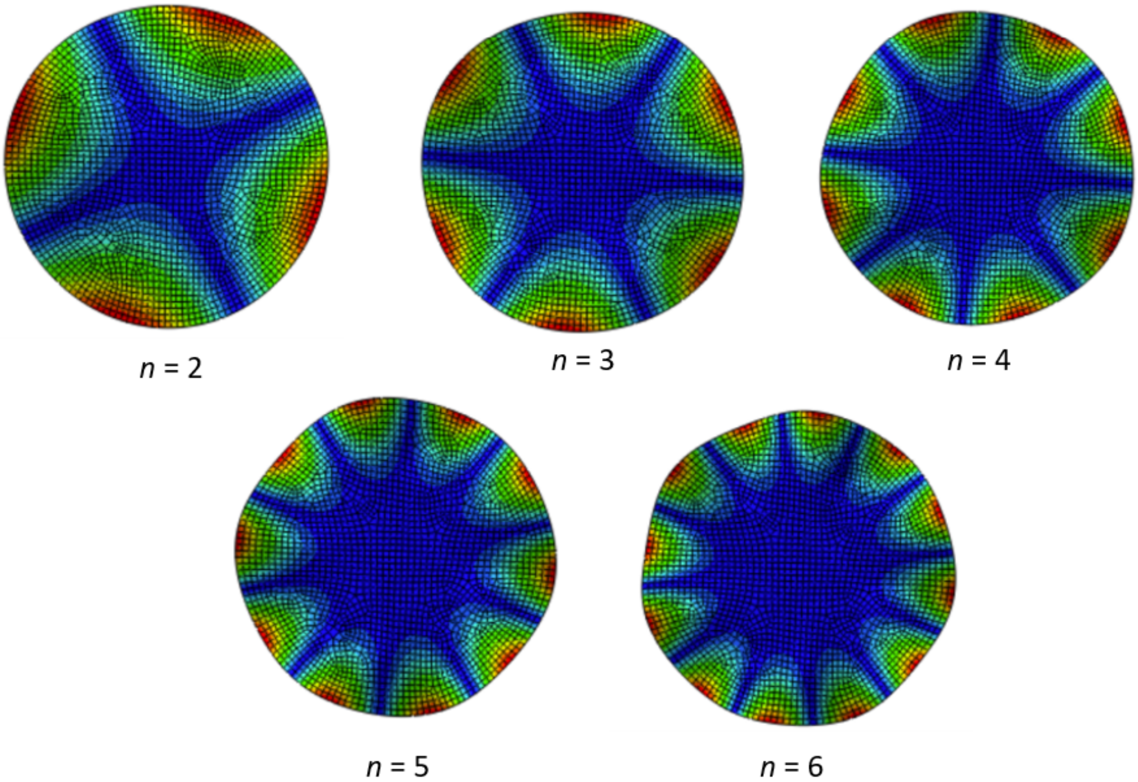

$n = 2$ $n = 3$ $n = 4$

$n = 5$ $n = 6$

Figure 3.8: *Mode shapes of the submerged disk, defined by its number of nodal diameters (n)*

Table 3.9 shows that the CASA model cannot accurately capture the first eigenvalue when the submerged object is a disk. The first eigenvalue produced by CASA has an error percentage of 19.71 %, while the rest have error percentages between 0.28 % and 4.20 %. In the experimental article by Valentín et al. (2017), no mechanical properties and no density or bulk modulus were given for the disk and water [62]. Furthermore, the experiment was conducted with different cover distances and different thicknesses of the covers. Multiple methods, such as the hammer signal and pressure sensors, were used to capture the natural frequencies. Both these methods yielded different results. The factors above contribute to producing different experimental results, which may be the cause of the low accuracy of the first CASA mode. However, CASA gives quite good predictions for higher modes.

Chapter 4

Submerged straight pipe

The same straight pipe used to verify the CASA in Section 3.1 is studied in this chapter. The pipe's dimensions and mechanical properties are listed in Table 3.1. It is fully constrained at both ends for boundary conditions. Different added mass approaches, with beam and shell elements, are discussed, and solutions for effective modelling are presented with verification by comparing the results with the CASA and the experimental results presented in Table 3.2.

In this case, it is important to note that there are both surrounding water and internal in the pipe. This makes the added mass formula described in Section 2.1 not accurate, as it only accounts for the surrounding fluid. Therefore, the added mass $m_{AddedMass}$ formulation must be adjusted to account for both fluids as

$$m_{AddedMass} = \rho_f \pi \frac{D^2 + d^2}{4} L_{Tot} \tag{4.1}$$

where ρ_f is the fluid density, D and d are the outer and inner diameter of the pipe, respectively, and L_{Tot} is the total length of the pipe.

4.1 Modelling the submerged straight pipe in ABAQUS

The pipe's eigenvalues are computed using ABAQUS with beam elements and compared to the results obtained from CASA. Commands from ABAQUS/Aqua are added to the input file, including coefficients for added mass in the eigenvalue analysis as described in Section 2.5.4. The added mass coefficient is set to 1.68 to take the internal fluid into account. The Lanczos solver is chosen for eigenvalue analysis as it is particularly effective in solving symmetrized eigen problems.

The lumped mass, increased density, and nonstructural mass approaches are tested with shell elements. The pipe is modelled with *S4* elements in the shell models. *S4* is a fully integrated, general-purpose, finite-membrane-strain shell element. The element's membrane response is treated with an assumed strain formulation that accurately solves in-plane bending problems. In areas where greater solution accuracy is required or for problems where in-plane bending is expected, *S4* will outperform element type *S4R* and *S8R* [9]. Accordingly, 2625 elements connected by 2646 nodes make up the pipe.

The beam models are designed using 20 *PIPE31* elements and 21 nodes. These elements simulate the hollow, thin-walled, circular shape of the pipe. They also consider the hoop stress caused by internal or external pressure, which affects the point's yield and causes an asymmetry in the section's response to inelastic bending. The hoop stress is assumed to be constant across any section and is calculated as the average stress in equilibrium with the internal and external pressure on the pipe section.

4.2 Modelling the submerged straight pipe in MATLAB

The added mass approach coded in MATLAB is described in Section 2.2, with the added mass formulation given in Equation (4.1). Boundary conditions are implemented conventionally by removing rows and columns of the augmented stiffness matrix related to the relevant degrees of freedom. In the case studied, both ends are fixed, and the first and last six (three translational and three rotational degrees of freedom) rows and columns are removed. Twenty elements are used to mesh the model.

4.3 Modal analysis results of the submerged straight pipe

4.3.1 CASA

A numerical study using CASA on a submerged straight pipe is conducted, and the first five eigenvalues are extracted. The first five eigenfrequencies are shown in Table 4.1, and the corresponding mode shapes are displayed in Figure 4.1.

Table 4.1: *The first five eigenfrequencies of the submerged straight pipe, simulated with CASA*

Mode	CASA [Hz]
1	198.5
2	526.6
3	983.7
4	1532.0
5	1544.0

Section 3.1 reported a close agreement between the CASA's predictions of the eigenvalues of a submerged straight pipe and its experimental results. Furthermore, Razi and Taheri (2015) recommended the CASA when considering VB-SHM of offshore pipelines [34]. Therefore, the simulated results in Table 4.1 will be trusted as good results.

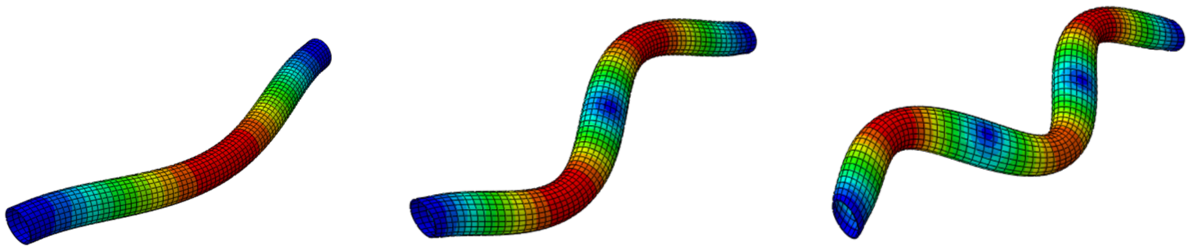

***(a)** Mode 1* ***(b)** Mode 2* ***(c)** Mode 3*

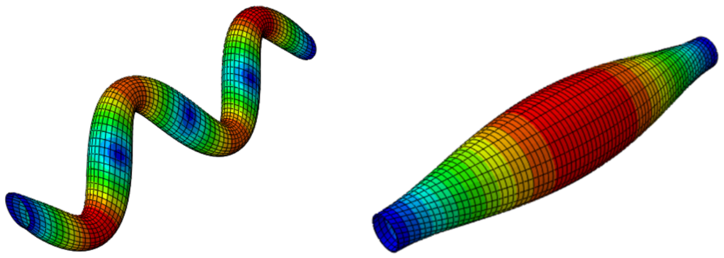

***(d)** Mode 4* ***(e)** Mode 5*

***Figure 4.1:** The first five eigenmodes of the submerged straight pipe*

4.3.2 Shell elements

The total added mass is calculated, using Equation (4.1), to be 4.745 kg. As a result, the density becomes 8000 kg/m^3, and the added mass per node is 1.793 $\cdot 10^{-3}$ kg for the increased density and lumped mass approach, respectively.

Table 4.2 shows the eigenvalues of the pipe in air, and the submerged pipe obtained via the three added mass approaches. ABAQUS primarily uses the nonstructural mass approach to simulate added mass shell structures [9]. The table indicates that the increased density and lumped mass approaches produce results nearly identical to the nonstructural mass simulations, making them suitable alternatives for programs lacking this function.

***Table 4.2:** The first five eigenfrequencies estimated for air and different added mass approaches with shell elements in ABAQUS*

	Eigenfreqencies [Hz]			
Mode	Increased density	Lumped mass	Nonstructural mass	Air
1	192.7	193.0	192.5	331.8
2	504.8	505.4	504.1	868.9
3	932.4	933.4	931.2	1605.0
4	1444.4	1445.3	1442.6	2486.4
5	898.1	896.0	897.0	1546.0

Table 4.3: *Comparison of the eigenfrequencies with shell elements in Table 4.2 and the CASA results in Table 4.1*

	% Difference to CASA		
Mode	Extra density	Lumped mass	Nonstructural mass
1	3	3	3
2	4	4	4
3	5	5	5
4	6	6	6
5	53	53	53

Table 4.3 shows that none of the three added mass approaches can correctly simulate the torsional (fifth) eigenvalue and that the difference between the added mass approaches and the CASA is over 50 %. In the torsional mode, the pipe exchanges almost no energy with the surrounding water and is expected to yield the same eigenvalues as if the pipe is in the air. Table 4.2 confirms this, as the difference between the fifth eigenfrequency predicted for the pipe in air and CASA is under 1 %. The CASA can simulate this condition correctly, while the added mass approaches cannot. In terms of the lateral bending modes, adding mass to shell elements predicts frequencies between 3 % and 6 % lower than the CASA.

4.3.3 Beam elements

Table 4.4 shows simulated eigenvalues of the pipe in air and the submerged pipe. The previous section showed that the added mass moment of inertia contributes to no rotary acceleration around the circular cross-section centre. Hence, the discrepancy associated with this approach is minimized only when the bending modes are dominant, and the contribution of the torsional modes could be ignored. Therefore should the torsional contribution in the added mass matrices be removed to align the torsional eigenfrequency of a submerged straight pipe with that of air.

Table 4.4: *First five eigenfrequencies estimated for air and the submerged pipe by added mass approaches with beam elements in MATLAB and ABAQUS*

	Eigenfrequencies [Hz]		
Mode	MATLAB	ABAQUS/Aqua	Air (ABAQUS)
1	216.4	191.7	332.6
2	576.5	502.7	869.0
3	1082.0	929.7	1600.3
4	1603.4	1441.7	2470.8
5	1548.7	1548.4	1548.4

Table 4.5 compares the results obtained in Table 4.4 and Table 4.1. Nevertheless, Table 4.5 shows that the ABAQUS/Aqua model can simulate accurate results for both lateral bending and torsional modes compared to CASA. The MATLAB model can also capture accurate results, with the largest difference of 9.5 % in the third eigenfrequency. The eigenmodes from MATLAB are in Figure 4.2.

Using beam elements for simulation is more cost-effective than using CASA. ABAQUS/Aqua produces simulated results with an error margin of around 5 % compared to CASA. Therefore, it is recommended to use the ABAQUS/Aqua command for the first five eigenvalues on a submerged straight pipe.

Table 4.5: *Comparison of the results obtained in Table 4.4 and Table 4.1*

	% Difference to CASA	
Mode	ABAQUS/Aqua	MATLAB
1	3	9
2	5	9
3	6	10
4	6	5
5	0	0

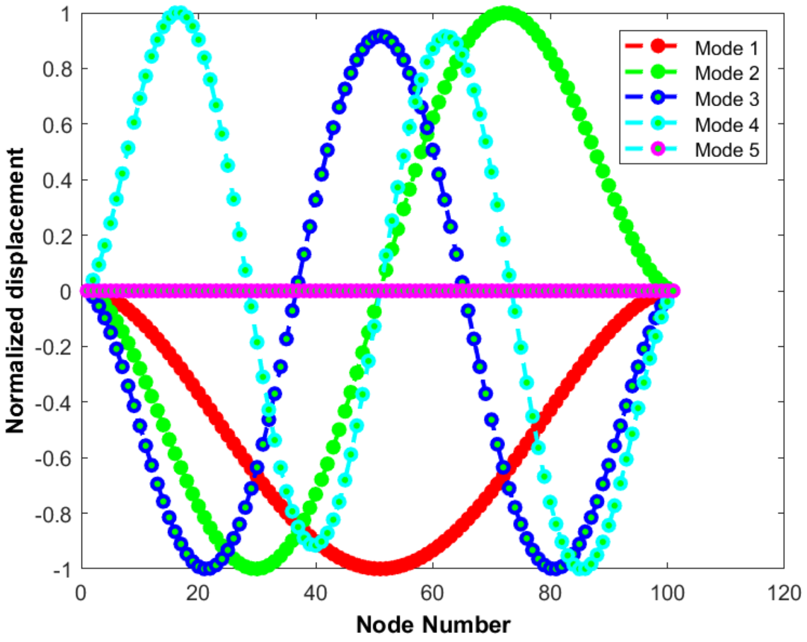

Figure 4.2: *Mode shapes of a submerged straight pipe, plotted in MATLAB*

Chapter 5

Submerged bends

Bends are used in piping systems because they ovalize more readily than straight pipes. Thus, they provide flexibility in response to thermal expansion and other loadings that impose significant displacements on the system. Ovalization is bending the pipe wall into an oval noncircular configuration. Thus, the bend behaves as a shell rather than as a beam. Straight pipe runs do not ovalize easily, so they behave like beams. Thus, complex interaction occurs between a bend and the adjacent straight pipe segments, even under pure bending. The bend causes some ovalization in the straight pipe runs, which tends to stiffen the bend. This interaction can create significant axial gradients of bending strain in the bend, especially in cases where the bend is very flexible.

This chapter provides details of the numerical models developed for investigating the vibration response of submerged bends. The models are developed in ABAQUS, and beam, shell, and solid elements are used to compare the eigenvalues of the pipe obtained via the CASA and nonstructural mass as the added mass approaches. To create the deformed cross-sections, the mesh of a deformed pipe is imported into the model. Nonstructural mass is then added to the imported mesh of the deformed bend. It is not possible to use a deformed bend with CASA. With CASA, the bend is modelled with shell elements and different thickness values are assigned to create a semi-oval cross-section. Finally, the eigenvalues of the deformed models are compared to the eigenvalues of non-deformed bends, simulated with beam elements.

5.1 Theory of a deformed bend with ovalities

By applying moments at each end, the pipe will open or close. As a result, the bend will experience ovalization and thickness change, and the cross-section will become semi-oval and elliptic, as shown in Figure 5.1.

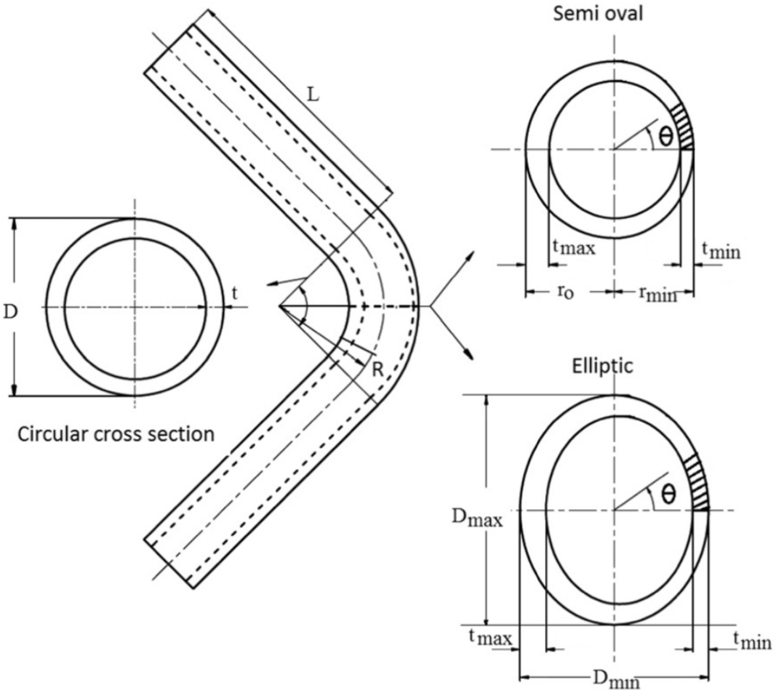

Figure 5.1: *90 ° pipe bend with attached straight pipe showing elliptical and semi-oval cross-sections. Illustration is from Sumesh et al. (2017) [7]*

The ovality value C_O can be defined as the difference between the significant and minor diameters, D_{Max} and D_{Min} respectively, divided by the nominal diameter of the pipe [7].

$$C_O = 2 \cdot \frac{D_{Max} - D_{Min}}{D_{Max} + D_{Min}} \tag{5.1}$$

Thickening appears at the intrados of the pipe bend, shown in Figure 5.2, and the thickening value C_{Thick} is denoted as the ratio of the difference between the nominal thickness t and the maximum thickness t_{Max} to the nominal thickness as [6]

$$C_{Thick} = \frac{t_{Max} - t}{t} \tag{5.2}$$

Thinning and appears at the extrados of the pipe bend, shown in Figure 5.2 and the thinning value C_{Thin} is denoted as the ratio of the difference between the nominal thickness t and the minimum thickness t_{Min} to the nominal thickness as

$$C_{Thin} = \frac{t - t_{Min}}{t} \tag{5.3}$$

The thickness change value C_t then becomes

$$C_t = C_{Thick} + C_{Thin} \tag{5.4}$$

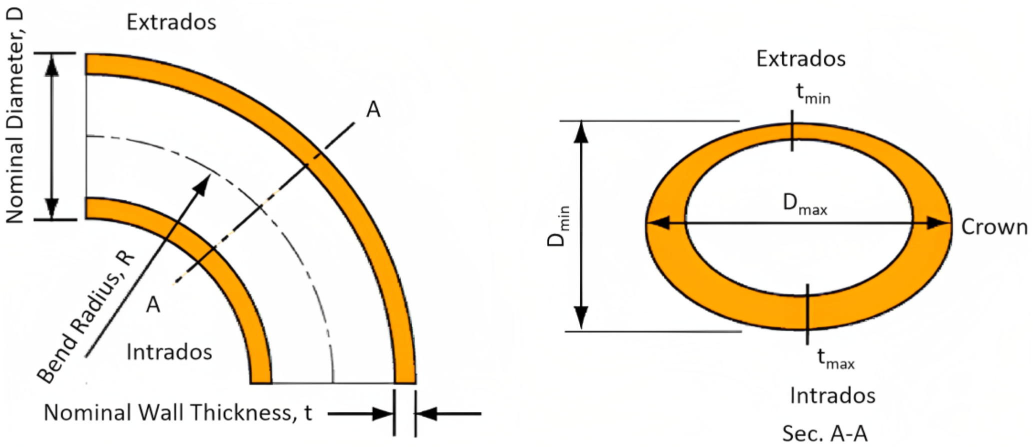

Figure 5.2: *Cross-Sectional Distortion of a Pipe Bend as viewed at Section A-A. Illustration from Sorour et al. (2019)[6]*

5.2 Modelling an ovalized pipe bend in ABAQUS

To understand how ovalization may change the results of modal analysis, thin and thick pipes with different ovality values are tested against a 90 ° bend with constant thickness and circular cross-section. A standard definition is that pipes with $D/t = 10$ and lower are thick-walled, while those with a larger ratio are thin-walled [5]. The D/t values are chosen to be 5 and 22, and the ovality values, given by Equation (5.1), are chosen to be 0 %, 3 % and 5 % to test the added mass effects on ovalized bends. The cross-section in the middle of thickness, 45 ° into the bend, is measured to acquire ovality values.

Table 5.1: *Thickness properties of the bend*

	$D/t = 5$	$D/t = 22$
Inner diameter [mm]	36.00	55.00
Wall thickness [mm]	12.00	2.75

The thin pipe is the same as ExxonMobil used to run experimental tests on an M-shaped jumper [63]. The outer diameter of the pipe is 0.0605 m. The bend is modelled with a bending radius of five times the pipe's outer diameter, resulting in a bending radius of 0.302 m and an arch length of 0.4752 m. The thickness properties are given in Table 5.1, and the mechanical properties are given in Table 5.2. The structure model of the pipe is visualized in Figure 5.3.

Table 5.2: *Mechanical properties of the pipe*

Property	Value	Unit
Elastic modulus	69	GPa
Shear modulus	26	GPa
Density	2700	kg/m^3

While the added mass approach can simulate ovalization with both ovality, thinning and thickening values, the CASA model will only have thinning and thickening values. The CASA model is therefore modelled with shell elements, while the added mass model used solids.

By bending the pipe, the circular cross-section becomes semi-oval and elliptic, as shown in Figure 5.1 where the diameter and the thicknesses change. ABAQUS can simulate both variables with solid and shell elements by selecting the field outputs U (translations and rotations) for the elliptic cross-section and STH (section thickness for shell elements) for the semi-oval cross-section.

The deformed pipe with an elliptic cross-section from the simulated obd-file can be imported as a new part of a new ABAQUS model. That way, the new part is a deformed pipe, and added mass simulations can be run with the nonstructural mass approach to test its effect on an elliptic cross-section. To model the thickness change in the shell models, a mapped analytical field can be created to add the different thicknesses, and nodal distribution can be chosen in the shell thickness section. The correct coordinates and section thickness of each node of the simulated obd-file has to be imported into the mapped field, defining the thickness of each node. In modal analysis, the original and deformed parts are tested with varying section thicknesses to test the effects of semi-oval cross sections.

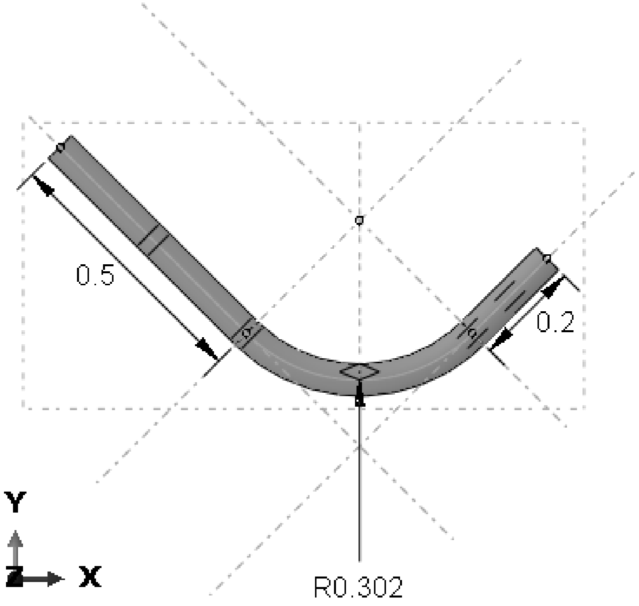

Figure 5.3: *Model of the pipe structure with dimensions in meters*

The pipe in the CASA model consists of 9360 linear quadrilateral elements of type *S4* and 9400 nodes. The water domain is modelled with a radiation boundary and a radius four times larger than the outer diameter of the pipe. Forty elements are applied along the outer and inner diameters of the water domain, and the approximate global mesh size is 0.02 m. This created 25872 quadratic hexahedral elements of type *AC3D20* and 112014 nodes. The mesh of the water domain is visualized in Figure 5.4.

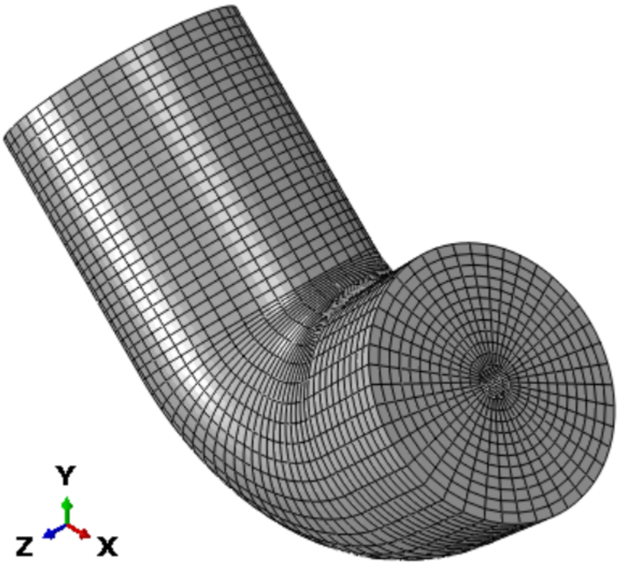

Figure 5.4: *Visual of the water domain mesh*

The added mass model is modelled with 40 elements along the outer and inner diameter and four elements as thickness. Four elements are chosen as the thickness to accurately calculate the ovality values by studying the movements of the nodes in the middle, as seen in Figure 5.5. From the mesh convergence study, the approximate global mesh size is 0.006 m, creating 30880 linear hexahedral elements of type *C3D8* and 38800 nodes. Clamped boundary conditions are assigned to the shortest end of the pipe, while the longer end is free.

For comparison purposes, beam models are also studied. The beam models are modelled with 24 *PIPE31* elements and 25 nodes. The cross-section and thickness will remain constant during the dynamic analysis. The nonstructural mass approach is used to add mass.

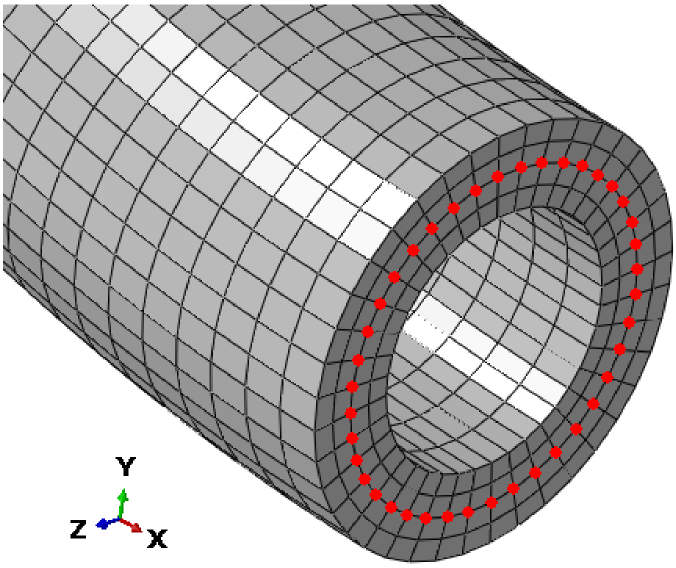

Figure 5.5: *Set of nodes chosen to study the ovality value.*

5.3 Ovality and thickness change results

Five per cent ovality is achieved on the thickest bend by applying a moment of 70 kNm on each side to close the pipe. The largest diameter $D_{Max} = 0.0619$ m and minor diameter $D_{Min} = 0.0587$ m creates a bend with an ovality value of $C_O = 5$ % using Equation (5.1). For the thinner pipe, a bending moment of 1.3 kNm on each side is required to close the pipe with an ovality value equal to $C_O = 5$ %. Three per cent ovality values are achieved with 50 kNm and 0.8 kNm for the thick and thin bend, respectively.

The different thickness values of the thick pipe with an ovality value of 5 % are in Figure 5.6, which created a thickness change value, using Equation (5.2), equal to $C_t = 5$ %. Figure 5.6 shows the thickness variation along the curve length and how thickening happens in intrados and thinning in extrados. The thick pipe's ovalization and thickness change values are equal for both 5 % and 3 %. The different thickness values of the thin pipe with 5 % ovality value are $t_{Max} = 2.76 \cdot 10^{-3}$ m and $t_{Min} = 2.74 \cdot 10^{-3}$ m, creating a thickness change value equal to $C_t = 0.5$ % using Equation (5.2). The thickness change value is ten times less than the ovality value for the thin pipe. The same applies when the ovality value of the thin pipe is $C_O = 3$ %, the thickness change value becomes $C_t = 0.3$ %.

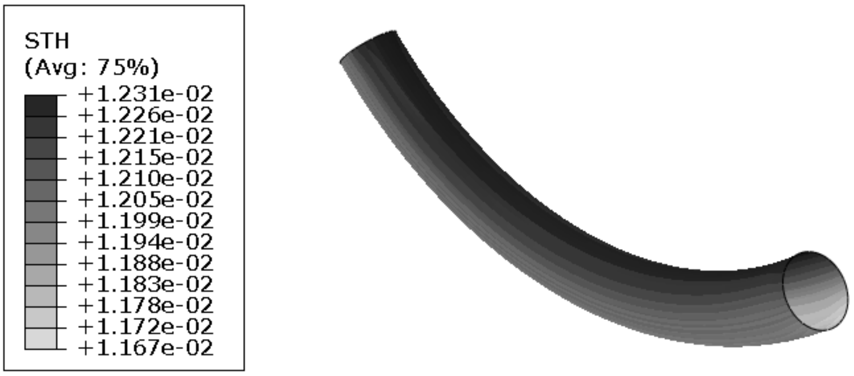

Figure 5.6: *Section thickness of 90 ° bend with an ovality value of 5 %*

5.4 Added mass effects on the ovalities in bends study with CASA

This section compares the results of a modal analysis performed on the 90 ° bend with and without ovalities submerged in water using CASA. The ovality values compared are 0 %, 3 %, and 5 %. The pipe is modelled using shell elements, while the water domain uses solid acoustic elements. The first six mode shapes are identical for the thick and thin pipe and are displayed in Figure 5.7. In-plane bending modes are represented by the second, fourth, and fifth modes, while out-of-plane bending or twisting modes are represented by the first, third, and sixth modes. Table 5.3 and Table 5.4 display the first six eigenvalues of the thick and thin pipes, respectively, at different thickness change values.

Table 5.3: *Eigenfrequencies obtained by CASA of a thick pipe with a 90 ° bend with different thickness change values*

	Eigenfrequencies [Hz]		
Mode	$C_t = 0$ %	$C_t = 3$ %	$C_t = 5$ %
1	31.81	31.82	31.83
2	35.68	35.69	35.69
3	130.5	130.5	130.5
4	134.4	134.5	134.5
5	399.3	399.5	399.6
6	458.1	458.2	458.2

Table 5.4: *Eigenfrequencies obtained by CASA of a thin pipe with a 90 ° bend with different thickness change values*

	Eigenfrequencies [Hz]		
Mode	$C_t = 0\,\%$	$C_t = 0.3\,\%$	$C_t = 0.5\,\%$
1	21.86	21.86	21.86
2	25.77	25.77	25.77
3	91.81	91.81	91.81
4	109.5	109.5	109.5
5	284.4	284.4	284.4
6	324.3	324.3	324.3

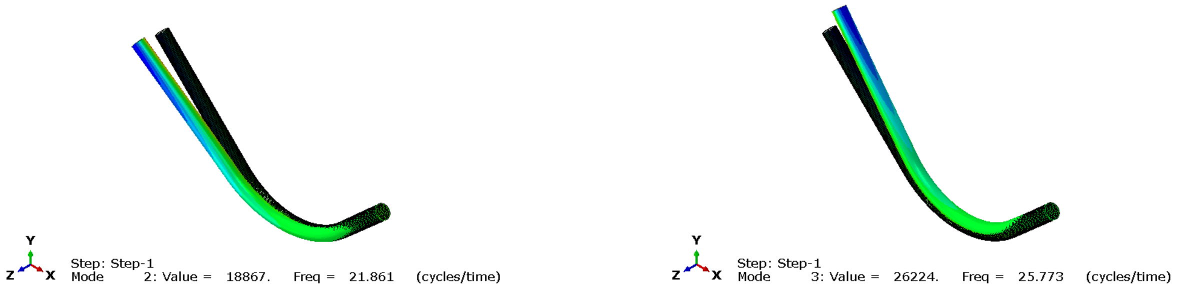

(a) *Mode 1* ***(b)*** *Mode 2*

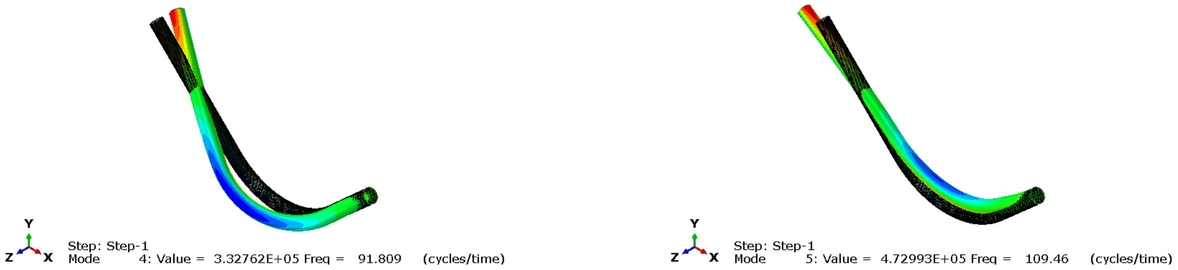

(c) *Mode 3* ***(d)*** *Mode 4*

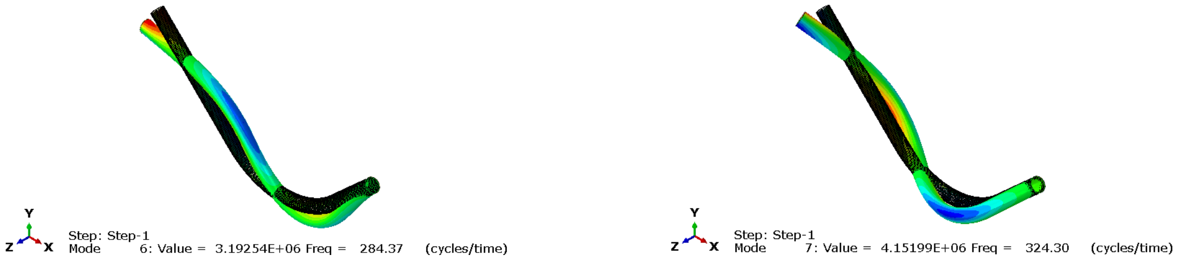

(e) *Mode 5* ***(f)*** *Mode 6*

Figure 5.7: *Eigenmodes 1 to 6 of a submerged thin pipe with a 90 ° bend without ovalities, obtained by CASA in ABAQUS*

The mode shapes are identical for all simulations. The eigenfrequencies slightly increase when the bend experience thickening in intrados and thinning in extrados. The difference between the ovalized pipes compared to the non-ovalized is less than 0.05 % for both the thick and thin pipes. Based on the analysis, the eigenvalues are unaffected when a pipe bend submerged in water experiences 5 % or less thickness change values, with a constant cross-section.

5.5 Added mass effects on the ovalities in bends study by adding mass to solid elements

This subsection compares the results of a modal analysis performed on the 90 ° bend with and without ovalities submerged in water using solid elements with the nonstructural mass approach to achieve the added mass effects. The different ovality values compared are 0 %, 3 % and 5 %. The deformed bends tested have both a semi-oval and elliptic cross-section. The models studied are described in Section 5.1 and Section 5.3. The first six mode shapes are the same as in Section 5.4 and are shown in Figure 5.7. Table 5.5 and Table 5.6 show the first six eigenvalues of the thick and thin pipe, respectively, with different ovality and thickness change values.

Table 5.5 shows that for the thick pipe, the eigenvalues decrease in the first six modes. The previous subsection, Table 5.3, showed that the eigenvalues slightly increase when the bends experience thinning and thickening. This indicates that changes in cross-section have a more significant impact on eigenvalues than changes in thickness. Figure 5.8 shows the differences between the ovalized thick pipes and the non-ovalized. The graphs show the peak differences in the third and fifth eigenmodes, with a 15 % difference for the bend with $C_O = 3$ % and a 17.5 % difference for the bend with $C_O = 5$ %, respectively.

Table 5.5: *Eigenfrequencies obtained with solid elements of a thick pipe with a 90 ° bend with different ovality values*

	Eigenfrequencies [Hz]		
Mode	$C_O = C_t = 0$ %	$C_O = C_t = 3$ %	$C_O = C_t = 5$ %
1	28.08	25.61	25.32
2	30.41	27.81	27.45
3	108.8	93.41	94.81
4	114.8	101.9	105.3
5	347.2	301.8	291.4
6	401.2	350.8	342.3

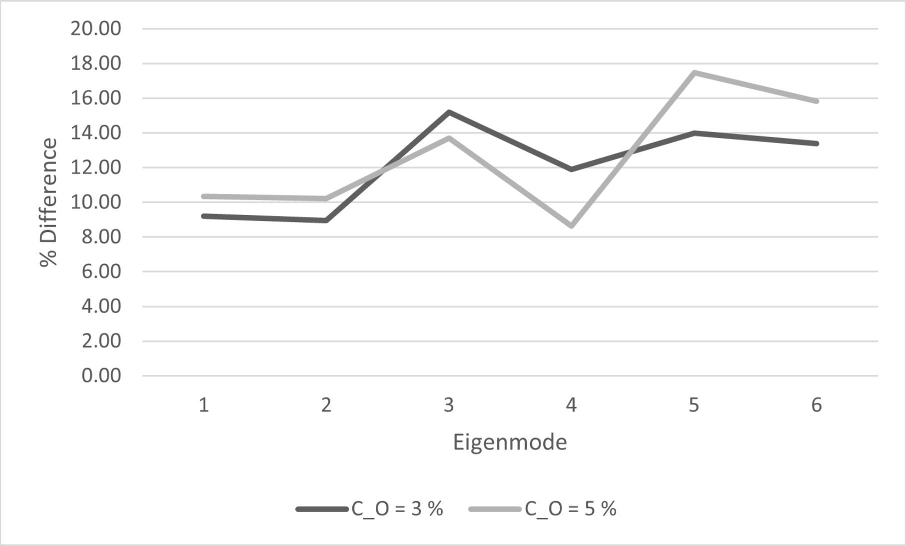

Figure 5.8: *Per cent differences of the eigenfrequencies of a thick pipe bend with different ovality and thickness change values compared to those of a thick pipe bend with no ovality and thickness change values*

Table 5.6 shows the eigenvalues of the thin pipe with different ovality and thickness values, and Figure 5.9 shows the differences. When comparing ovalized and non-ovalized pipes, the differences are more noticeable in thick pipes than in thin pipes. The thin pipe experiences ovality values ten times greater than the thickness change values. As shown in Table 5.6, the elliptical cross-section dominates the ovalization effects, resulting in smaller eigenfrequencies for ovalized pipes compared to non-ovalized pipes. Figure 5.9 demonstrates that the eigenvalues decrease significantly in the second and fifth eigenmodes for ovalized pipes compared to non-ovalized pipes. However, there is little difference between the eigenfrequencies of the two ovalized pipes.

Table 5.6: *Eigenfrequencies obtained with solid elements of a thin pipe with a 90° bend with different ovality values*

	Eigenfrequencies [Hz]		
Mode	$C_O = C_t = 0$ %	$C_O = 3$ % and $C_t = 0.3$ %	$C_O = 5$ % and $C_t = 0.5$ %
1	20.54	18.42	18.44
2	21.04	18.63	18.50
3	76.37	69.82	69.71
4	85.29	79.32	79.73
5	250.2	220.5	220.0
6	294.9	268.0	268.2

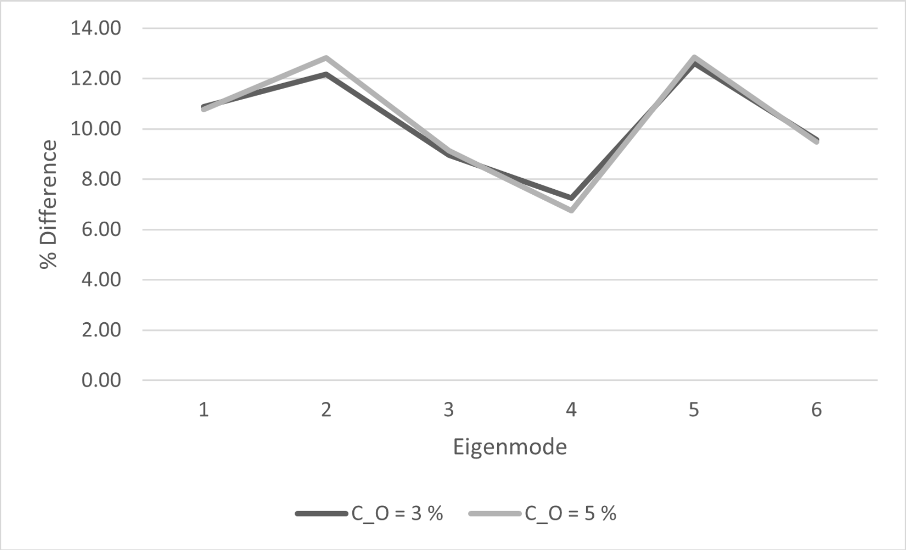

Figure 5.9: *Per cent differences of the eigenfrequencies of a thin pipe bend with different ovality and thickness change values compared to those of a thin pipe bend with no ovality and thickness change values*

5.5.1 Comparison to beam elements

Table 5.7 shows the eigenfrequencies of the thick and thin pipe simulated with beam elements. The third and fourth mode shapes are switched in order for both the thin and thick pipe, compared to those simulated with solid and shell elements, shown in Figure 5.7. The per cent difference between the eigenfrequencies simulated with beam elements in Table 5.7 and the ovalized pipes simulated with solid elements in Table 5.5 and Table 5.6 are shown in Table 5.8. The results indicate that for thin pipes, the difference in eigenfrequencies between ovalized and non-deformed pipes ranges from 5 % to 24 %, whereas for thick pipes, the differences are between 0 % and 18 %.

Table 5.7: *The first six eigenfrequencies of the thick and thin bend, simulated with beam elements*

	Eigenfrequencies [Hz]	
Mode	Thick	Thin
1	27.25	21.80
2	29.59	23.67
3	111.68	88.56
4	105.29	83.49
5	335.03	262.12
6	389.69	305.85

Table 5.8: *Comparison of the eigenfrequencies of a deformed pipe with ovalities simulated with solid elements, and a non-deformed pipe simulated with beam elements*

	% Difference to beam elements			
	Thick		Thin	
Mode	$C_O = 3\ \%$	$C_O = 5\ \%$	$C_O = 3\ \%$	$C_O = 5\ \%$
1	6	7	17	17
2	6	7	24	24
3	18	16	24	24
4	3	0	5	5
5	10	14	17	17
6	10	13	13	13

-This page is left initially blank-

Chapter 6

Submerged single-planar jumpers

This chapter examines the eigenvalues of jumpers with a single-planar geometry in two scenarios. Four cost-effective added mass techniques are examined and compared to CASA. A method, which is as reliable as CASA but much less expensive, is presented to simulate the natural frequencies and mode shapes.

6.1 Submerged M-shaped jumper

ExxonMobil performed model tests using an M-shaped jumper model to verify potential VIV prediction methods [63]. Uniform bottom currents were simulated to reduce velocities that excite the target vibration modes. The model had an arch length of 13.96 m and a scale ratio of 4.525. The tests included using a one-meter straight cylinder section to measure drag forces and assess the sensitivity to Reynolds number changes. Static pull tests were conducted to excite and identify the first modes. The jumper model had 13 tri-axial accelerometers and three strain gauges installed along its length, and the test setup is shown in Figure 6.1. The tests were performed at flow angles of ten and 45 °, with current velocities ranging from 0.05 to 0.98 m/s. For a flow angle of 90 °, data was measured for current rates up to 0.79 m/s. When the model was towed with a 10 ° orientation to the model plane, the following observations were made: At a towing speed of 0.412 m/s, a typical cross-flow VIV response occurred, with out-of-plane vibration observed at a frequency close to the model's out-of-plane natural frequency (first mode). In-plane vibration (second mode) occurred at a towing speed of 0.206 m/s, close to the model's in-line natural frequency. Finally, out-of-plane twist vibration (third mode) was observed at a towing rate of 0.527 m/s and close to the jumper's out-of-plane twist vibration natural frequency. The response amplitudes for all accelerometers were provided for these three cases.

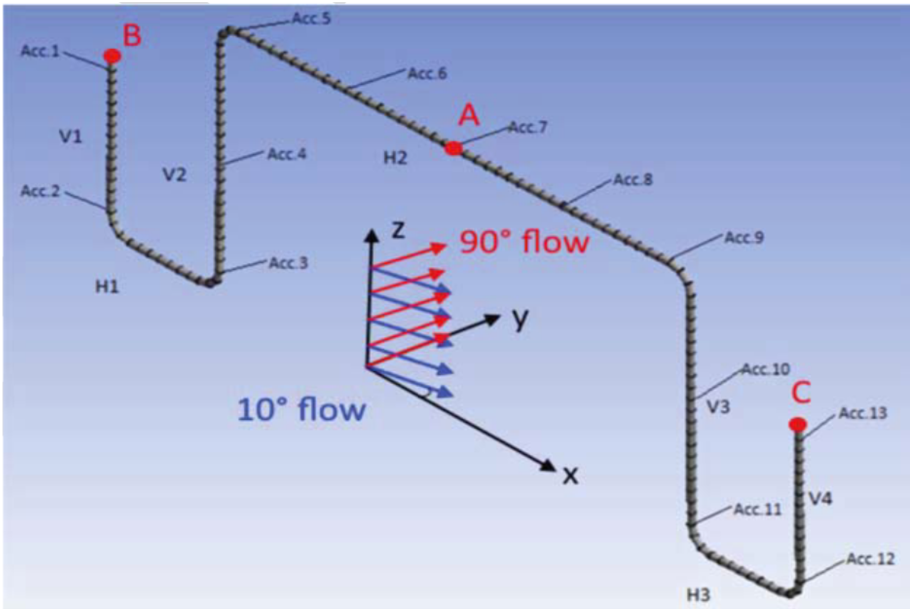

Figure 6.1: *Jumper model with locations of accelerometers, strain gauges and pipe segments and the current directions, Liu et al. (2019) [4]*

Sieber et al. (2021) used the jumper in Figure 6.1 and ran simulations with the ABAQUS beam element types *PIPE31* and *ELBOW31B* [5]. The segment lengths of the jumper can be seen in Table 6.1. *PIPE31* is an elastic pipe element for which plane stress is assumed. All degrees of freedom are uncoupled from hoop stresses and hoop strains since they are known from shell theory. *ELBOW31B* is a bend element type implemented with reference to Bathe, [64]. It can account for the deformation of the cross-section and kinematic non-linearity. In contrast to Bathe's bend elements, *ELBOW31B* is only linear-elastic.

In the simulation, Sieber et al. (2021) got that the *ELBOW31B* results were generally lower than the ones from the *PIPE31* models. Eigenmode two and three were switched in order, where the *ELBOW31B* results correlated with the observations from the model test done by ExxonMobil. This gives a relevant reason to use elbow elements in the analysis of subsea jumpers. Thus, obtaining the correct order of mode shapes and modal frequencies is essential.

In the experiment done by ExxonMobil, the use of thin-walled aluminium pipe meant that

Table 6.1: *Segment lengths of the jumper model*

Segment name	Length [m]
Vertical 1	1.495
Horizontal 1	1.000
Vertical 2	2.323
Horizontal 2	4.327
Vertical 3	2.323
Horizontal 3	1.000
Vertical 4	1.495
Total length	13.96

the model jumper was relatively less massive than the thick-walled steel prototype [63]. Low-density oil and high-density sugar were contained within the prototype, and lead weights were distributed evenly along the length to add mass. This increased the final mass ratio of the model to 2.33. Table 6.2 shows the model properties of the simulated jumper model.

Table 6.2: *Simulated model properties*

Parameter	Value	Unit
Total length	13.50	m
Unit mass	6.66	kg/m
Outer diameter	60.50	mm
Inner diameter	55.00	mm
Elastic modulus	69.00	GPa
Shear modulus	26.10	GPa

The 90 ° corners are modelled as curved fillets for the case scenario. The bending radius is three times the pipe's outer diameter, resulting in a bending radius of 0.1815 m and an arch length of 0.2851 m. This made the model's total length decrease to 13.50 m.

From Table 6.2, the total mass of the jumper becomes 89.9 kg. The material density is increased to reach this magnitude in the simulation. The volume of the jumper is $6.73 \cdot 10^{-3}$ m^3, making the material density 13350 kg/m^3.

6.1.1 Modelling the submerged M-shaped jumper in ABAQUS

The CASA model represents the jumper using 26920 quadratic hexahedral elements labelled as *C3D20* (An 8-node linear brick [9]), along with 53880 nodes. The choice of *C3D8* over *C3D8R* is due to the latter being less stiff in bending. For both ends, fully restrained boundary conditions (clamped) are assigned. The water domain is modelled using 244509 quadratic tetrahedral elements named *AC3D10* (acoustic three-dimensional 20-node elements with one degree of freedom per node), connected by 356869 nodes. The fluid's density and bulk moduli are 1000 kg/m^3 and 2.13 GPa, respectively.

Three approaches are utilized to add mass to the models with shell elements: lumped mass, nonstructural mass, and increased density, which are explained in Section 2.5.1, Section 2.5.2 and Section 2.5.3, respectively. The jumper is modelled with 66870 quadratic quadrilateral elements of type *S4* and 66900 nodes.

PIPE31 elements are used to model the beam models. The approximate global mesh size is 0.05 m, creating 272 linear line elements of type *PIPE31* and 273 nodes. Because of the bends, the nonstructural mass and increased density approaches are used.

In their study, Sieber et al. (2021) demonstrated the importance of choosing between traditional pipe elements and elbow elements when conducting modal analysis for a jumper model [5]. Elbow elements can account for the cross-section deformation, as described in Section 2.4, and additional strain terms due to bending, allowing for adding mass using the ABAQUS/Aqua command. The straight sections of the jumper model are represented by the *PIPE31* element, while the bends are modelled using either *ELBOW31*, *ELBOW31B*, or *ELBOW31C* elements. For two-node elements, *ELBOW31* is the most comprehensive, as it has continuous warping and ovalization with the deforming cross-section and linear interpolation along the pipe. *ELBOW31B* is a simplified version of the pipe in space, with ovalization only where axial gradients of the ovalization are ignored. *ELBOW31C* is similar to *ELBOW31B*, except that only the first term in the Fourier interpolation around the pipe is included. According to the ABAQUS manual, it is recommended to specify six Fourier modes and 18 additional integration points around the circumference for ovalization [9]. The elbow models employed ABAQUS/Aqua commands to replicate the surrounding water.

6.1.2 Modelling the M-shaped jumper in MATLAB

The jumper is modelled in MATLAB as described in Section 2.2. The MATLAB function *eigs* calculates the eigenfrequencies and mode shapes. It is meshed with 20 elements per straight part, creating 160 elements and 161 nodes. Boundary conditions are implemented conventionally by removing rows and columns of the augmented stiffness matrix related to the relevant degrees of freedom. In the case studied, both ends are fixed, and the first and last six rows and columns are removed.

6.1.3 CASA

Table 6.3 shows the first nine eigenfrequencies simulated by the CASA. The mode shapes for each eigenvalue are shown in Figure 6.2 to Figure 6.10. It is vital to obtain the correct order of mode shapes in modal analysis, and the first three eigenmodes correlate with the experimental results obtained experimentally by ExxonMobil [63]. This confirms the integrity of the CASA model.

Table 6.3: *Eigenfrequencies of the submerged M-shaped jumper simulated with the CASA*

Mode	CASA [Hz]
1	0.846
2	1.988
3	2.162
4	2.506
5	3.387
6	3.555
7	3.772
8	6.354
9	6.756

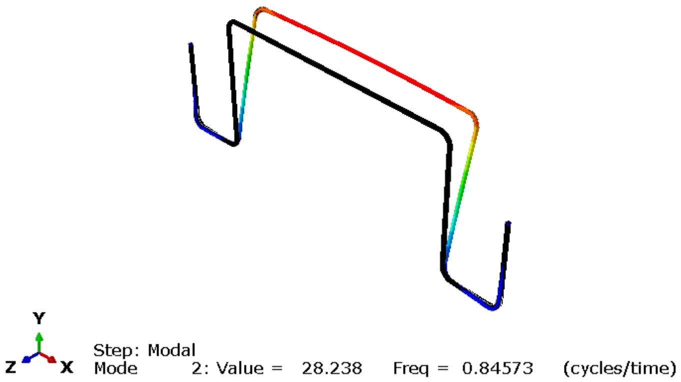

Figure 6.2: *Mode one of the submerged M-shaped jumper. out-of-plane bending in the z-direction with the largest displacement at the top horizontal*

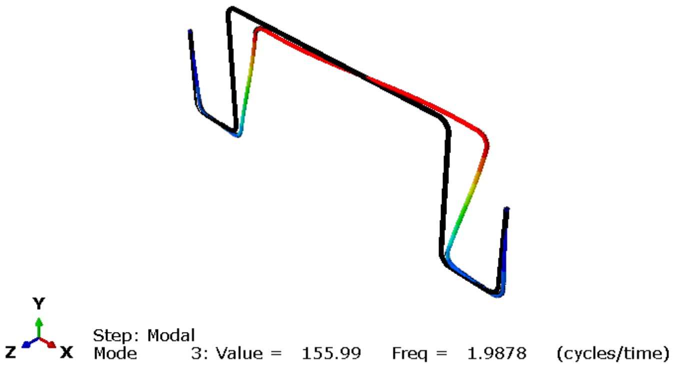

Figure 6.3: *Mode two of the submerged M-shaped jumper. In-plane bending in the x-direction.*

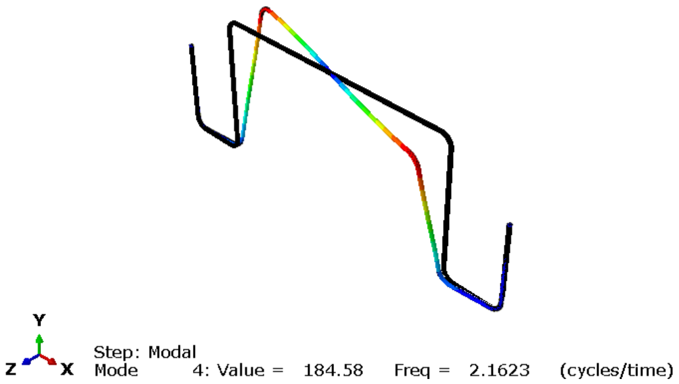

Figure 6.4: *Mode three of the submerged M-shaped jumper. Out-of-plane twist.*

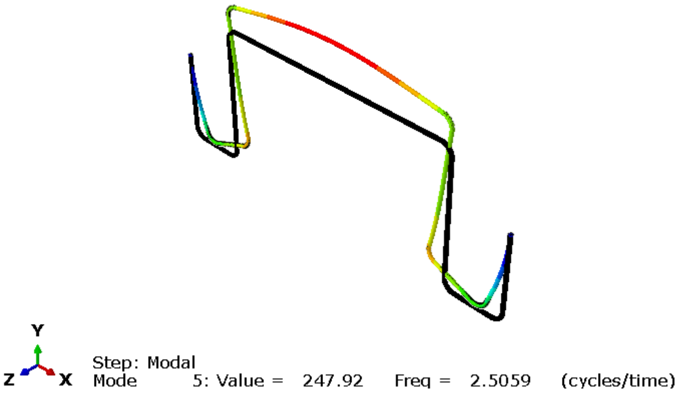

Figure 6.5: *Mode four of the submerged M-shaped jumper. In-plane bending in the y-direction.*

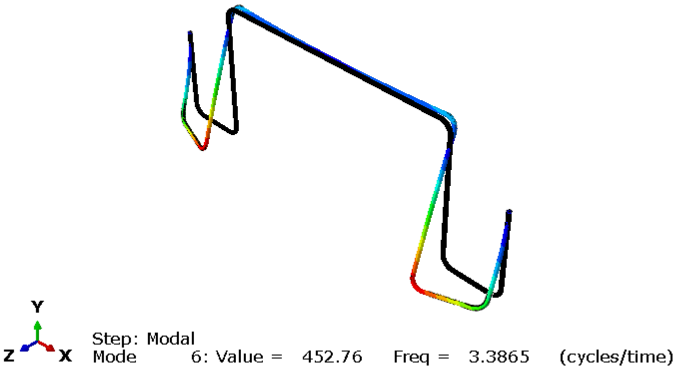

Figure 6.6: *Mode five of the submerged M-shaped jumper. Symmetric out-of-plane bending of the two bottom segments in the z-direction.*

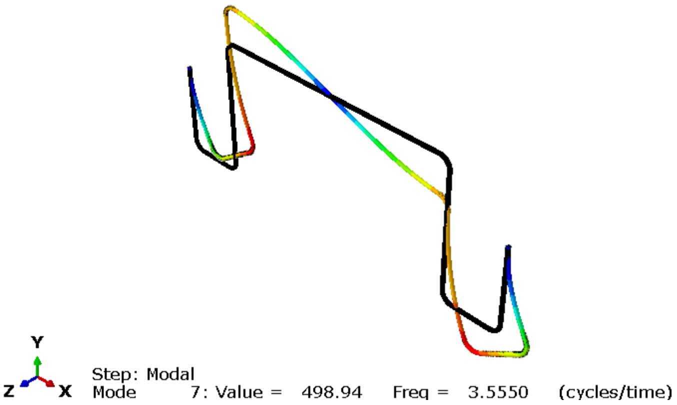

Figure 6.7: *Mode six of the submerged M-shaped jumper. Diagonal distortion in both x and y-direction.*

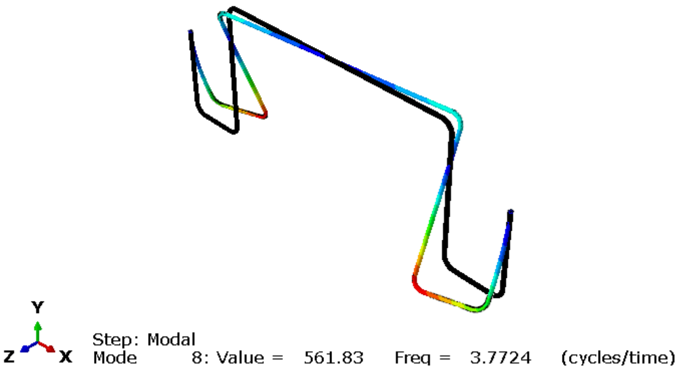

Figure 6.8: *Mode seven of the submerged M-shaped jumper. Asymmetric out-of-plane bending of the two bottom segments in the z-direction.*

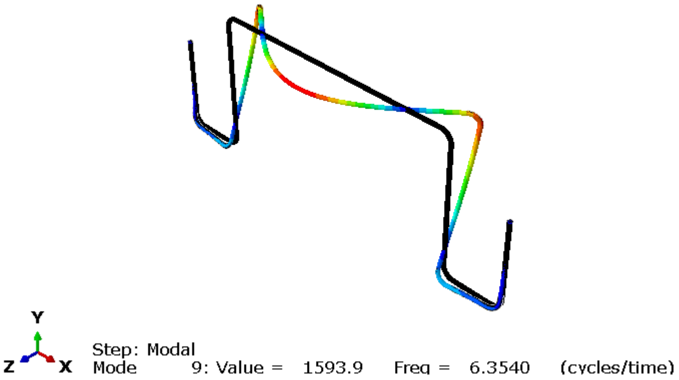

Figure 6.9: *Mode eight of the submerged M-shaped jumper. Out-of-plane bending in the z-direction. The largest displacement occurs as buckling of the top horizontal.*

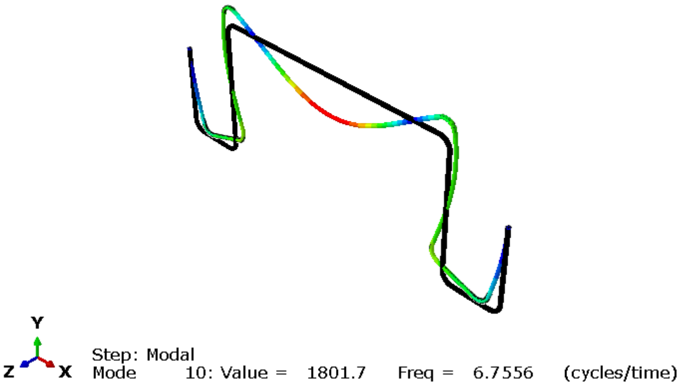

Figure 6.10: *Mode nine of the submerged M-shaped jumper. In-plane bending in the y-direction. The largest displacement occurs as buckling of the top horizontal.*

6.1.4 Shell elements

Various approaches are being tested for the shell models, including lumped mass, increased density, and nonstructural mass. Using Equation (2.26), the total added mass is determined to be 38.80 kg, where the added mass coefficient is one. The model is divided into 49200 nodes, and the lumped mass approach indicates an added mass of 0.001128 kg per node. Additionally, the increased density is specified to be 19110 kg/m^3.

Table 6.4 shows the eigenfrequencies obtained with the different added mass approaches. Compared to the CASA model, eigenmode five and six are switched in order so that in-plane bending occurs at a lower frequency than the symmetric out-of-plane bending. When following the DNV GL response model procedure, FEA modal results are utilized for fatigue analysis, too [5]. Thus, obtaining the correct order of mode shapes and modal frequencies is essential. Compared to the CASA results, the per cent differences are in Table 6.5.

Table 6.4: *The first nine eigenfrequencies of the M-shaped jumper, estimated with different added mass approaches with shell elements in ABAQUS*

	Eigenfrequencies [Hz]		
Mode	Nonstructural mass	Increased density	Lumped mass
1	0.847	0.843	0.849
2	1.807	1.777	1.807
3	2.151	2.156	2.155
4	2.409	2.357	2.404
5	3.417	3.187	3.423
6	3.256	3.379	3.239
7	3.799	3.762	3.806
8	6.440	6.334	6.451
9	6.474	6.337	6.393

Table 6.5 reveals reasonable estimations for the out-of-plane mode shapes and noticeably worse estimations for the in-plane bending modes. The shell models give very similar results, underestimating the CASA estimations between 4 % and 11 % in the in-plane bending modes.

Table 6.5: *Comparison of the results obtained in Table 6.4 and Table 6.3*

	% Difference to CASA			
Mode	Nonstructural mass	Increased density	Lumped mass	Type of bend/twist
1	0.2	0.3	0.4	Out of plane
2	9.5	11.2	9.5	In-plane
3	0.5	0.3	0.3	Out of plane
4	4.0	6.1	4.1	In-plane
5	0.9	0.2	1.1	Out of plane
6	8.8	10.9	9.3	In-plane
7	0.7	0.3	0.9	Out of plane
8	1.3	0.3	1.5	Out of plane
9	4.3	6.4	5.5	In-plane

6.1.5 Beam elements

Table 6.6 displays the estimated eigenfrequencies using the nonstructural mass and increased density approach in ABAQUS, as well as the results obtained from running the MATLAB script. Table 6.7 compares the results from Table 6.6 to the CASA results in Table 6.3. In the ABAQUS models, eigenmodes five and six are switched, causing in-plane bending to occur at a lower frequency than symmetric out-of-plane bending. Nonetheless, the ABAQUS models produce reasonable results for both the out-of-plane and in-plane bending modes. Table 6.7 shows none of the estimations have an error percentage over 5 % compared to CASA. MATLAB's *eigs* command can accurately simulate the first, fifth and sixth eigenfrequencies. In the first eigenmode, the difference between the eigenfrequencies is almost 1 %, while for the second and third modes, the differences are over 60 %. However, MATLAB can simulate the first seven mode shapes in the correct order as shown in Figure A.1. It is worth noting that the jumper in MATLAB is designed with corners instead of bends, which can cause notable variations in eigenfrequencies.

Table 6.6: *The first nine eigenfrequencies of the M-shaped jumper, estimated with different added mass approaches with beam elements in ABAQUS and MATLAB*

	Eigenfrequencies [Hz]		
Mode	Nonstructural mass	Increased density	MATLAB
1	0.885	0.884	0.837
2	2.066	2.063	0.993
3	2.260	2.257	1.152
4	2.507	2.504	2.783
5	3.447	3.444	3.336
6	3.397	3.393	3.674
7	3.838	3.834	4.050
8	6.457	6.450	5.419
9	6.810	6.803	4.804

Table 6.7: *Comparison of the results obtained in Table 6.6 and Table 6.3*

	% Difference to CASA			
Mode	Nonstructural mass	Increased density	MATLAB	Type of bend/twist
1	4.5	4.4	1.0	Out of plane
2	3.8	3.7	66.7	In-plane
3	4.4	4.3	60.9	Out of plane
4	0.0	0.1	10.5	In-plane
5	1.8	1.7	1.5	Out of plane
6	4.6	4.7	3.3	In-plane
7	1.7	1.6	7.1	Out of plane
8	1.6	1.5	15.9	Out of plane
9	0.8	0.7	33.8	In-plane

6.1.6 Elbow elements

Table 6.8 shows the eigenfrequencies produced with the different elbow models in ABAQUS. The mode shapes are identical for all the elbow models as to CASA, shown in Figure 6.2 to Figure 6.10. Table 6.9 shows the maximum relative error of eigenvalue results occurs for mode two with the *ELBOW31* model with 1.19 %, compared to CASA. However, the errors for other models and modes are below one per cent, which is a good correlation. The CASA model uses solid elements for both the pipe and water, while the elbow models use beam elements and shell theory is applied to model the cross-section deformation. By utilizing the ABAQUS/Aqua command to apply added mass, the simulation of elbow models is significantly less expensive than the CASA model. This presents a valid reason to use elbow elements in the analysis of subsea jumpers.

Table 6.8: *The first nine eigenfrequencies of the ELBOW31, ELBOW31B, ELBOW31C model*

	Eigenfrequencies [Hz]		
Mode	*ELBOW31*	*ELBOW31B*	*ELBOW31C*
1	0.843	0.844	0.844
2	1.964	1.970	1.975
3	2.158	2.160	2.162
4	2.500	2.501	2.504
5	3.395	3.397	3.398
6	3.543	3.546	3.551
7	3.783	3.784	3.785
8	6.374	6.376	6.377
9	6.730	6.744	6.753

Table 6.9: *Comparison of the three elbow models to the CASA model*

	% Difference to CASA		
Mode	*ELBOW31*	*ELBOW31B*	*ELBOW31C*
1	0.3	0.2	0.2
2	1.2	0.9	0.6
3	0.2	0.1	0.0
4	0.2	0.2	0.1
5	0.3	0.3	0.3
6	0.3	0.2	0.1
7	0.3	0.3	0.3
8	0.3	0.3	0.4
9	0.4	0.2	0.0

6.2 Submerged S-shaped jumper

The use of ABAQUS/Aqua to add mass to beam and elbow elements yielded similar results to the CASA method for the M-shaped jumper. The M-shaped jumper tested was a smaller model in a lab with a scale ratio of 4.525. A new full-scale jumper with a different geometry is simulated to validate the added mass with the elbow elements approach. Various approaches to add mass to shell, beam, and elbow elements, will be compared to the CASA method. An efficient modelling approach will also be presented that produces almost identical results to the CASA method.

The Subsea Rigid Jumper (SRJ) plays a crucial role in Ultra Deep Water (UDW) projects, connecting manifolds, riser bases, and well heads. In a study by Bruschi et al. (2017), they addressed the VIV phenomenon in complex 3D SRJs to assess fatigue damage caused by potential stress intensification [65]. The study focused on a specific SRJ with 2D shape geometry, where both ends were fixed. This geometry is shown in Figure 6.11, and its material properties and dimensions are listed in Table 6.10.

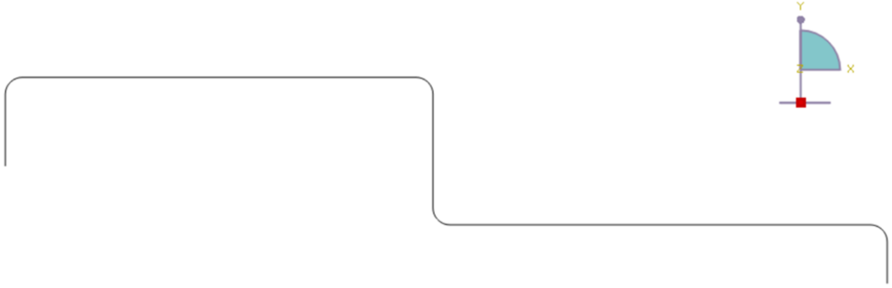

Figure 6.11: *S-shaped jumper Geometry*

The 90 ° bends are modelled as five times the outer diameter, resulting in a bending radius of 0.5715 m and an arch length of 0.8977 m. With this configuration, the total length of the jumper is 38.92 m, and its total mass is 1712 kg. The material density is set to 10290 kg/m^3 to achieve these values in the simulation.

Table 6.10: *Mechanical properties and dimensions of the S-shaped jumper*

Mechanical properties	Value	Unit
Elastic modulus	206.0	GPa
Mass per unit length	44.0	kg/m
Poisson's ratio	0.3	-
Outer diameter	114.3	mm
Wall thickness	13.5	mm
Vertical 1	3.0	m
Horizontal 1	14.5	m
Vertical 2	5.0	m
Horizontal 2	15.4	m
Vertical 3	2.0	m

6.2.1 Modelling the submerged S-shaped jumper in ABAQUS

The jumper in the CASA model is created using 56958 linear hexahedral elements of type *C3D8* and 113960 nodes. The EWD is chosen to be five times the outer diameter of the water surrounding it. To create the model, an approximate global mesh size of 0.06 m is used, resulting in 155496 quadratic hexahedral elements of type *AC3D20* for the straight parts and 97817 quadratic tetrahedral elements of type *AC3D10* for the bends. The water domain consists of 827135 nodes with a bulk modulus of 2.13 GPa and a density of 1025 kg/m^3. The jumper and water domain are fully restrained with clamped boundary conditions on both ends.

Three added mass approaches are tested to add mass to shell elements: the lumped mass, nonstructural mass, and increased density approaches. The jumper is modelled with an approximate mesh size of 0.016 m for the shell element models, creating 49180 linear quadrilateral elements of type *S4* and 49200 nodes.

The beam models are modelled with 326 linear line elements of type *PIPE31*. The elbow models are modelled with elbow elements for the bends, creating 309 linear line elements of type *PIPE31* and 20 linear line elements of type *ELBOW31*. The elbow model is the only one that employed ABAQUS/Aqua commands to replicate the surrounding water. In contrast, the other beam models used increased density and nonstructural mass to add mass since they contained bends instead of corners.

6.2.2 CASA

Table 6.11 shows the first six eigenfrequencies simulated by the CASA. The mode shapes for each eigenvalue are shown in Figure 6.12 to Figure 6.17. Mode two and four, pictured in Figure 6.13 and Figure 6.15 respectively, show in-plane bending modes, while the rest are out-of-plane mode shapes.

Table 6.11: *The first six eigenfrequencies of the S-haped jumper simulated with the CASA model*

Mode	CASA
1	0.333
2	0.373
3	0.799
4	1.699
5	1.857
6	1.972

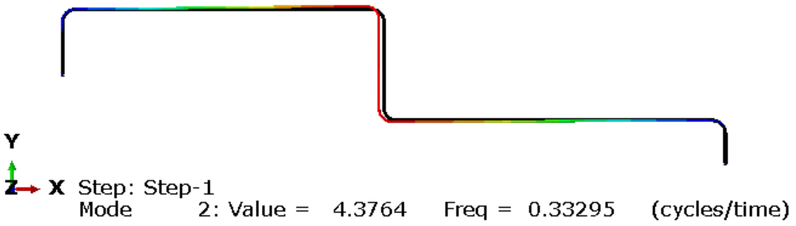

(a) *Front view*

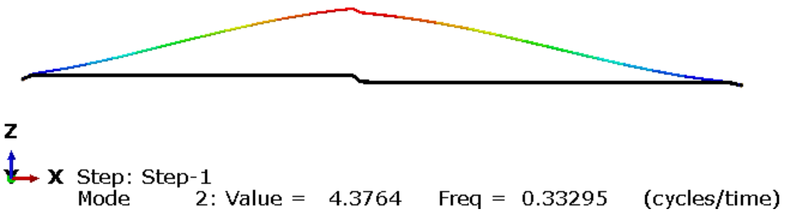

(b) *Top view*

Figure 6.12: *Mode one of the S-shaped jumper. Out-of-plane bending in z-direction*

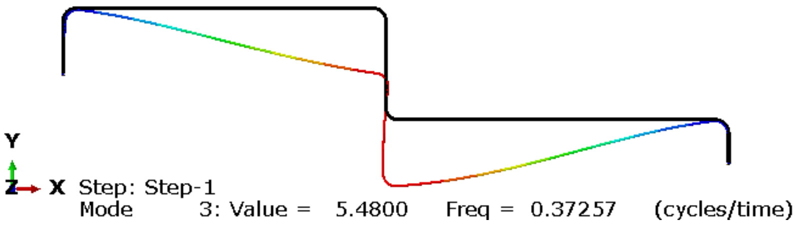

(a) *Front view*

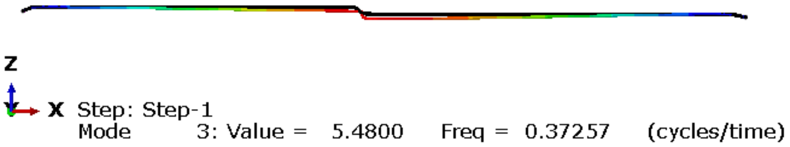

(b) *Top view*

Figure 6.13: *Mode two of the S-shaped jumper. In-plane bending in y-direction*

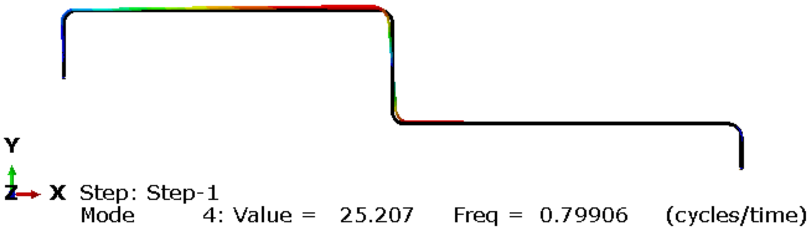

(a) *Front view*

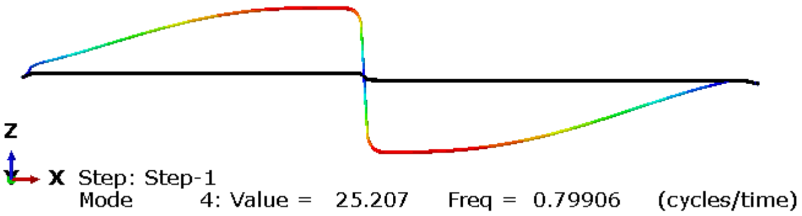

(b) *Top view*

Figure 6.14: *Mode three of the S-shaped jumper. Out-of-plane twist with the largest displacement at the middle vertical*

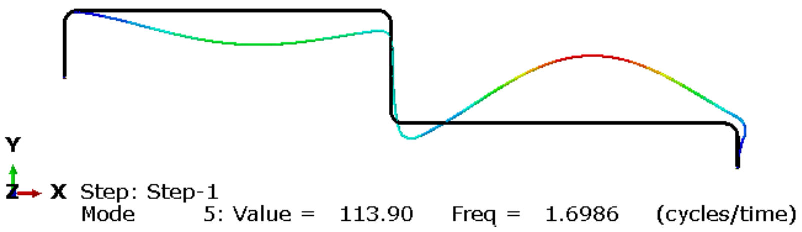

(a) *Front view*

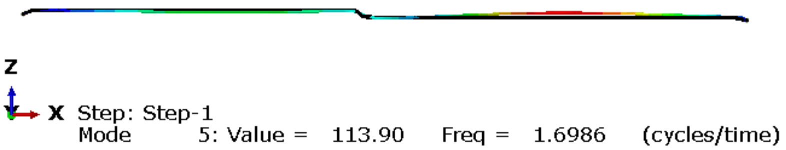

(b) *Top view*

Figure 6.15: *Mode four of the S-shaped jumper. In-plane bending in the y-direction with the largest displacement at the lower horizontal*

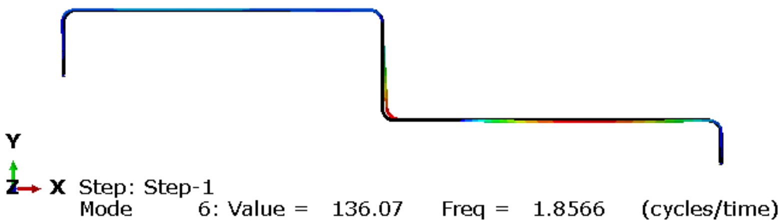

(a) *Front view*

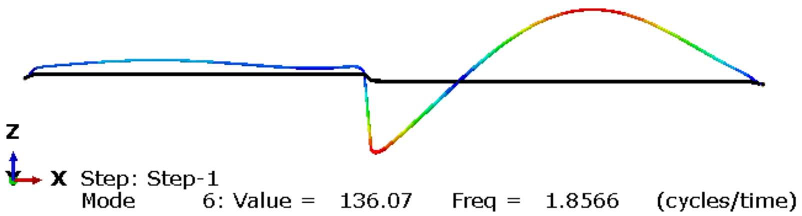

(b) *Top view*

Figure 6.16: *Mode five of the S-shaped jumper. Out-of-plane bending in the z-direction with the largest displacement at the lower horizontal*

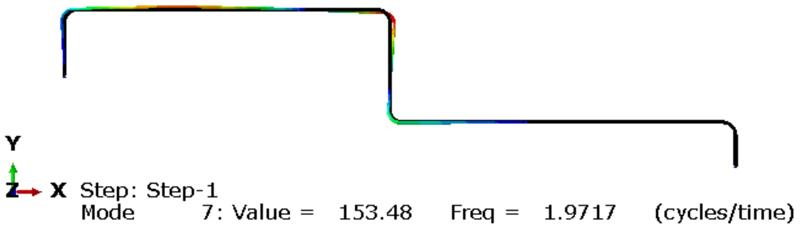

***(a)** Front view*

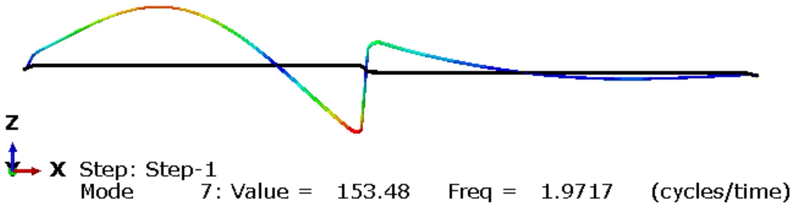

***(b)** Top view*

***Figure 6.17:** Mode six of the S-shaped jumper. Out-of-plane bending in the z-direction with the largest displacement at the top horizontal*

6.2.3 Shell elements

Various approaches are being tested for the shell models, including lumped mass, increased density, and nonstructural mass. Based on Equation (2.26), the total added mass is 409.3 kg, with added mass coefficients set to one. The model is meshed with 49200 nodes, and the lumped mass approach shows an added mass of 0.008320 kg per node. The increased density is set to 12750 kg/m^3.

***Table 6.12:** The first six eigenfrequencies simulated with the lumped mass, increased density and nonstructural mass approach with shell elements*

	Eigenfrequencies [Hz]		
Mode	Lumped mass	Increased density	Nonstructural mass
1	0.330	0.330	0.330
2	0.358	0.358	0.358
3	0.792	0.792	0.792
4	1.666	1.667	1.666
5	1.839	1.840	1.839
6	1.953	1.954	1.953

Table 6.12 shows the first six eigenfrequencies obtained via the three added mass approaches. Table 6.13 shows the per cent comparisons to CASA. The mode shapes estimated with the three added mass approaches are in the exact order as estimated with CASA. Compared to

Table 6.13: *Comparison of the results simulated with the three added mass models with shell elements in Table 6.12 to the CASA results in Table 6.11*

	% Difference to CASA		
Mode	Lumped mass	Increased density	Nonstructural mass
1	0.9	0.9	0.9
2	4.0	4.0	4.0
3	0.9	0.9	0.9
4	1.9	1.9	1.9
5	0.9	0.9	0.9
6	0.9	0.9	0.9

the added mass results with shell elements for the M-shaped jumper, Table 6.13 shows good results. The out-of-plane bending modes are estimated with an error percentage under 1 %, and the in-plane estimations with a maximum error percentage of 4 %.

6.2.4 Beam elements

The different added mass approaches used to simulate the surrounding water with beam elements are the nonstructural mass and increased density approaches for the *PIPE31* modes and ABAQUS/Aqua for the elbow model.

Table 6.14: *The first six eigenfrequencies simulated with the increased density and nonstructural mass approach for the beam models, and ABAQUS/Aqua approach for the elbow models*

	Eigenfrequencies [Hz]		
Mode	Nonstructural mass	Increased density	Elbow
1	0.333	0.333	0.333
2	0.363	0.363	0.372
3	0.798	0.798	0.798
4	1.684	1.684	1.696
5	1.853	1.854	1.854
6	1.967	1.967	1.969

Table 6.14 shows the first six eigenfrequencies obtained via the three added mass approaches. Table 6.15 shows the per cent comparisons to CASA. The order of the mode shapes estimated through three added mass approaches in ABAQUS matches the order estimated through CASA. Compared to the added mass results with shell elements, Table 6.15 demonstrates more promising results for the beam and elbow simulations. The maximum error percentage for the *PIPE31* models is observed in the second eigenmode and is 2.65 %. The errors for all

Table 6.15: *Comparison of the results simulated with the three added mass models with beam elements in Table 6.14 to the CASA results in Table 6.11*

	% Difference to CASA		
Mode	Nonstructural mass	Increased density	Elbow
1	0.0	0.0	0.0
2	2.7	2.6	0.1
3	0.1	0.1	0.1
4	0.8	0.8	0.2
5	0.2	0.2	0.1
6	0.2	0.2	0.1

eigenvalues of the elbow model remain under 0.2 %. For both the submerged single-planar jumpers, adding mass with ABAQUS/Aqua to beam and elbow elements produces nearly identical results to CASA.

6.3 Cost-effectiveness analysis

The previous sections provided details on the accuracy of adding mass to different elements compared to the CASA. Both Section 6.1 and Section 6.2 show that adding mass to a combination of beam and elbow elements using the ABAQUS/Aqua command is the most accurate approach on single-planar jumpers. However, despite the focus on accuracy, it is important to consider the cost-effectiveness of the methods employed. The question arises regarding efficient resource allocation: What method is the most cost-efficient?

The information presented in Table 6.16 displays the duration of each job and the estimated memory usage by ABAQUS. The results indicate that for the M-shaped jumper, the elbow model is significantly faster than the CASA model by a factor of 2157 and 17 times faster than the shell models. Additionally, the elbow model requires significantly less memory usage compared to the CASA model by over 700 times and over 40 times less than the shell models. The same pattern follows for the S-shaped jumper, where the analysis duration with the elbow model is only one second, which is 4151 and 26 times less than the CASA and the shell models, respectively. In addition, the memory usage of the elbow model compared to the CASA model is 880 times less and over 50 times less than the shell models.

Table 6.16: *The time and estimated memory usage of each analysis on adding mass with the CASA, shell elements, and beam and elbow elements on submerged single-planar jumpers performed by ABAQUS*

	M-shaped jumper		S-shaped jumper	
	Wallclock time (s)	Memory [MB]	Wallclock time (s)	Memory [MB]
CASA	2157	36213	4151	47602
Shell	17	2061	26	2887
Elbow	1	50	1	54

When running a modal analysis, adding mass to beam and elbow elements using the ABAQUS/Aqua command is recommended for submerged single-planar jumpers. With both the M- and the S-shaped jumper, it is more cost-effective and as reliable as adding mass with the CASA.

-This page is left initially blank-

Chapter 7

Submerged multi-planar jumpers

This chapter studies the eigenvalues of jumpers with multi-planar geometry in two cases. Four cost-effective added mass approaches are compared to the CASA. For jumpers in a 2D plane, the beam and elbow elements produced results closest to the CASA. With elbow elements, the mode shapes were simulated in the correct order, and the eigenfrequencies were almost identical to CASA. The in-plane bending modes simulated with shell elements could not estimate accurate eigenfrequencies. There are no in-plane bending modes with multi-planar jumpers, and shell elements may produce more accurate results than beam and elbow elements.

7.1 Submerged multi-planar Z-shaped jumper

Li et al. (2022) presented an experimental investigation and numerical model of flow-induced vibration in a multi-planar subsea jumper [66]. The researchers examined the flow pattern of the Z-shaped jumper and installed pressure and displacement sensors near the elbows to record the jumper's vibration and pressure response. The jumper parameters and dimensions are shown in Figure 7.1 and in Table 7.1.

In the simulated scenario, the 90 ° corners are represented as curved fillets. The bending radius is three times the pipe's outer diameter, which equals a bending radius of 0.1560 m and an arch length of 0.2450 m. Due to this, the total length of the model has decreased to 4.898 m.

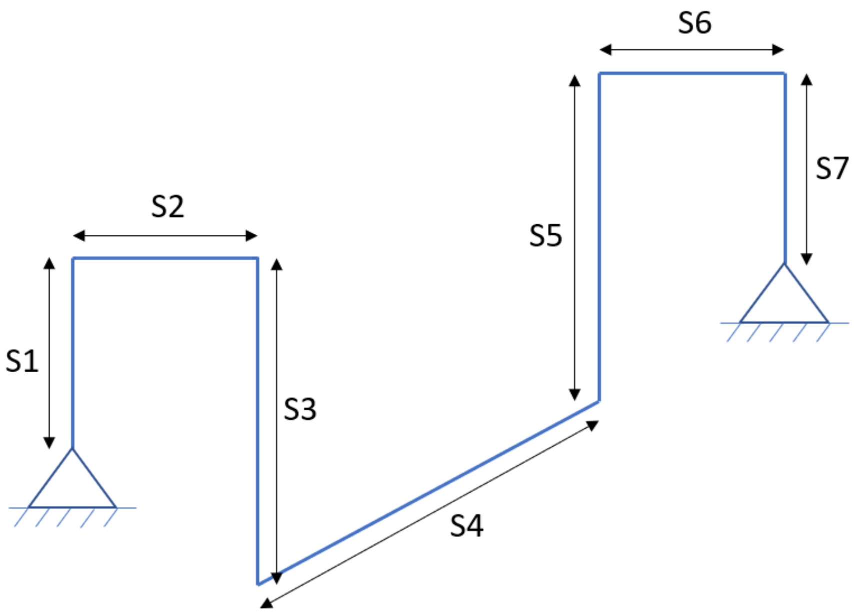

Figure 7.1: *Detailed Z-shaped jumper model*

Table 7.1: *Parameters of the Z-shaped jumper model*

Parameter	Value	Unit
Outer diameter	52.0	mm
Wall thickness	2.0	mm
S1, S2, S6, S7	0.5	m
S3, S5	0.8	m
S4	2.0	m
Density	7850	kg/m^3
Poisson's ratio	0.3	-
Elastic Modulus	206	GPa

7.1.1 Modelling of the submerged multi-planar Z-shaped jumper in ABAQUS

The jumper in the CASA model is modelled with 204926 linear hexahedral elements of type *C3D8* (An 8-node linear brick) and 410010 nodes. A dense mesh is achieved with an approximate size of 0.002 m. The EWD is three times the outer diameter for the surrounding water domain. The water domain is modelled with an approximate mesh size of 0.015 m, creating 320736 quadratic hexahedral elements of type *AC3D20* and 1365104 nodes. Tetrahedron elements are commonly used to model thick bends. However, this creates too many errors in the intersection between the water domain and the jumper. To achieve a mesh without errors, the model must be heavely partitioned, as shown in Figure 7.2. A visual of the mesh is shown in Figure 7.3. The density and bulk modulus are 1025 kg/m^3 and 2.13 GPa. Both ends are fully restrained with clamped boundary conditions for the jumper and water domain.

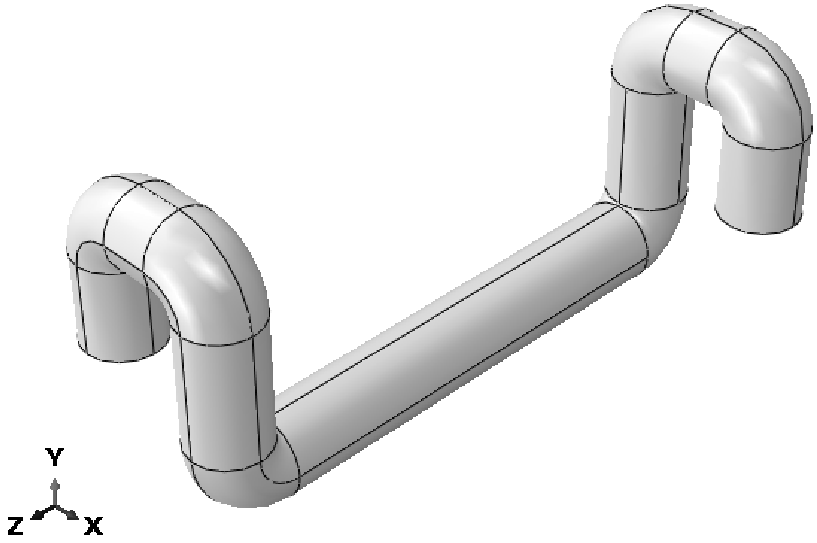

Figure 7.2: *Partitioned model of the water domain*

Three approaches for adding mass to the shell elements are tested: the lumped mass, non-structural mass, and increased density. The shell models consist of 17503 linear quadrilateral elements of the type *S4* and 17526 nodes.

The beam models are modelled with 256 linear line elements of type *PIPE31*. The nonstructural mass and increased density approaches are tested. The elbow model contains 184 linear line elements of type *PIPE31* for the straight sections and 72 linear line elements of type *ELBOW31* for the bends. ABAQUS/Aqua is being utilized to account for the added mass in the

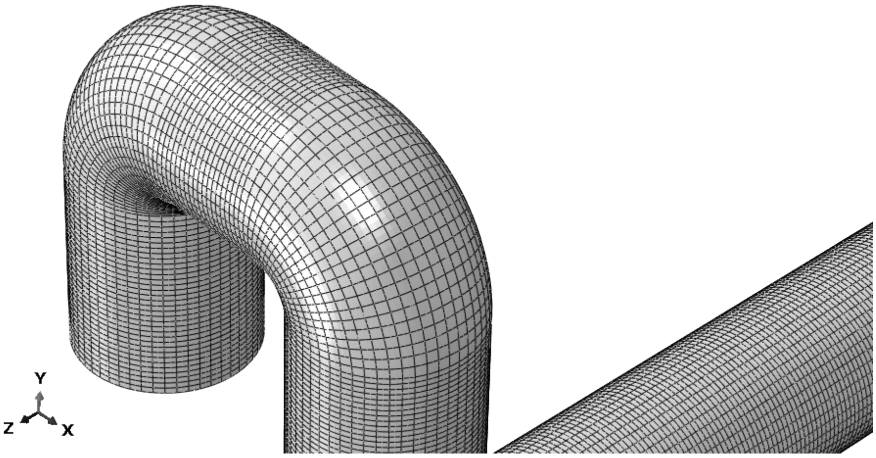

Figure 7.3: *Visual of the water domain mesh*

elbow model.

7.1.2 CASA

Table 7.2 shows the first five eigenfrequencies simulated by CASA, where its corresponding mode shapes are shown in Figure 7.4 to Figure 7.8. Notice that the second and third eigenvalues in Table 7.2 are nearly identical.

Table 7.2: *Eigenfrequencies of the multi-planar jumper simulated with the CASA*

Mode	CASA
1	8.64
2	17.27
3	17.48
4	26.48
5	32.09

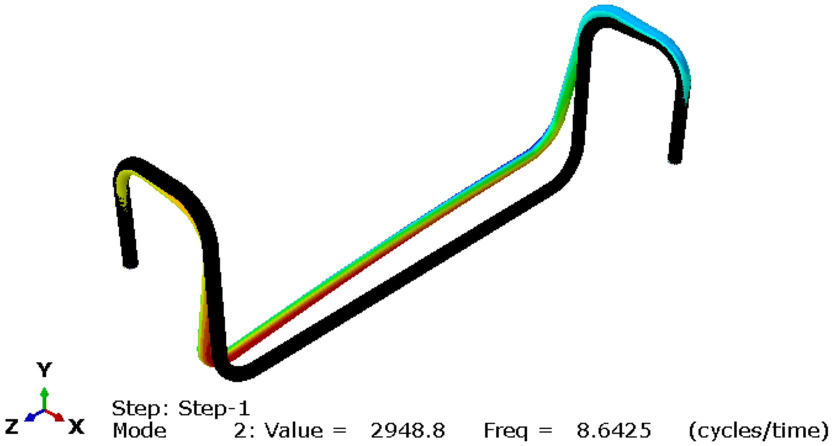

Figure 7.4: *Mode one of the Z-shaped jumper. Displacement in the x-direction*

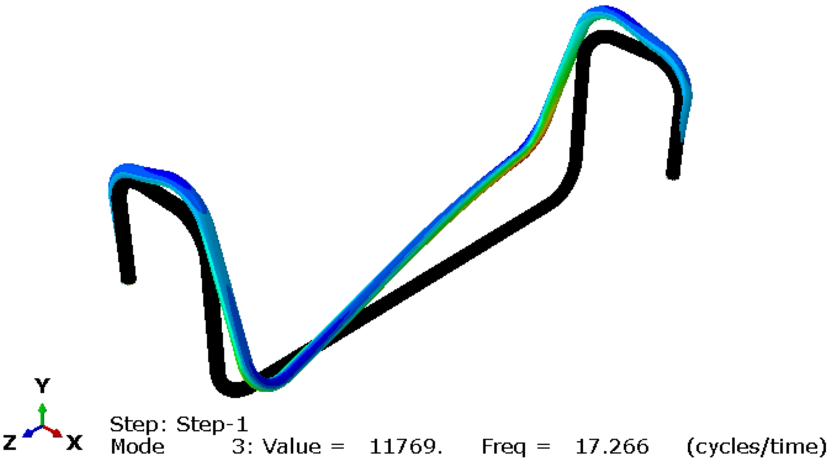

Figure 7.5: *Mode two of the Z-shaped jumper. Twist about the y-axis*

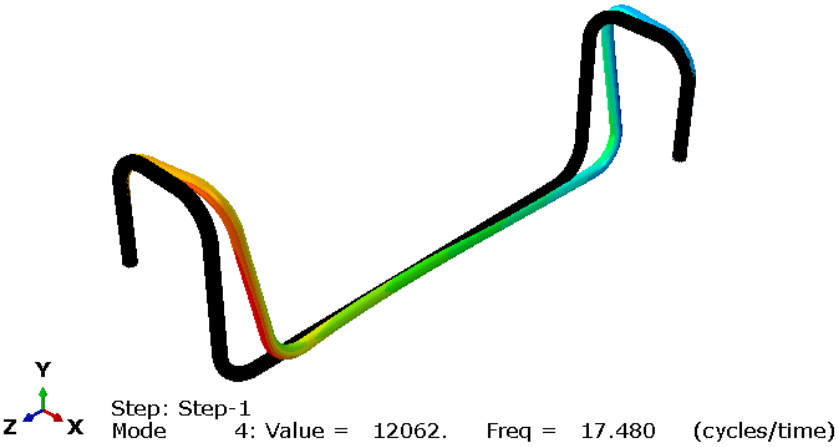

Figure 7.6: *Mode three of the Z-shaped jumper. Displacement in the z-direction*

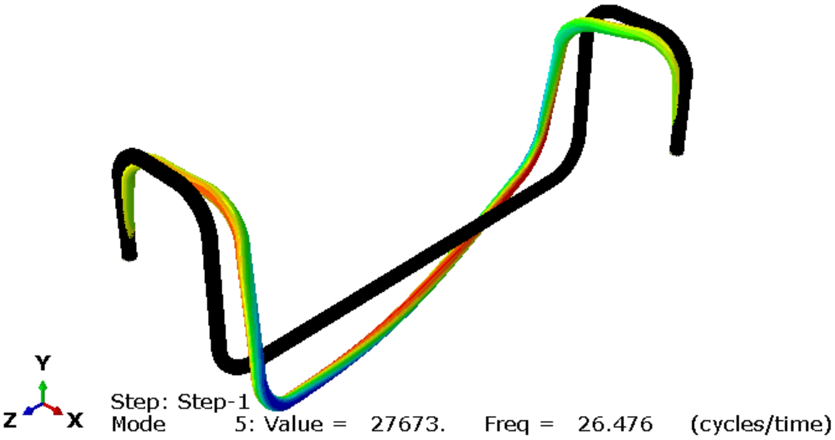

Figure 7.7: *Mode four of the Z-shaped jumper. Twisting about the y-axis and bending in the y-direction.*

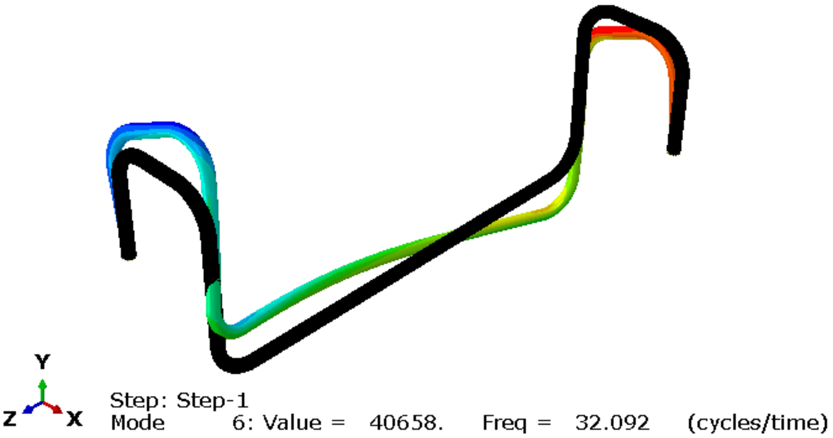

Figure 7.8: *Mode five of the Z-shaped jumper. Bending in the x-direction and twisting about the x-axis*

7.1.3 Shell elements

For the shell models, the added mass coefficients are set equal to one, making the total added mass, calculated with Equation (2.26), 10.40 kg. The model is meshed with 16790 nodes, making the added mass per node, for the lumped mass approach, $61.96 \cdot 10^{-4}$ kg. The increased density is set to 14610 kg/m^3.

Table 7.3 shows the first five eigenfrequencies obtained via the three added mass approaches. All the added mass approaches with shell elements estimate similar results where the second and third eigenmode are switched compared to CASA. Table 7.4 shows the per cent comparisons to CASA. The most significant error margins happen in the third and fifth mode shapes, shown in Figure 7.6 and Figure 7.8, respectively. In these modes, the error margins differ between 15 % and 16.4 % for the third mode and 12 % and 13.3 % for the fifth mode.

Table 7.3: *The first five egenfrequencies simulated with the lumped mass, increased density and nonstructural mass approach with shell elements in ABAQUS*

		Eigenfrequencies [Hz]	
Mode	Lumped Mass	Increased density	Nonstructural mass
1	8.70	8.64	8.75
2	16.74	16.66	16.87
3	14.83	14.85	15.04
4	27.02	26.78	27.13
5	28.45	28.09	28.45

Table 7.4: *Comparison of the results simulated with the three added mass models with shell elements in Table 7.3 to the CASA results in Table 7.2*

	% Difference to CASA		
Mode	Lumped Mass	Increased density	Nonstructural mass
1	1	0	1
2	3	4	2
3	16	16	15
4	2	1	2
5	12	13	12

7.1.4 Beam elements

Table 7.5 shows the eigenfrequencies estimated with beam and elbow elements. Compared to CASA, eigenmode two and three are switched in order, where the displacement in the z-direction mode is estimated with a lower frequency than the y-axis twisting mode. A possible reason for this could be the near-identical values of the second and third eigenvalues as seen in Table 7.2. The increased density and nonstructural mass approach produced almost identical results for the first five mode shapes. Table 7.6 shows the per cent differences to CASA. Unlike the single-planar jumpers tested in Chapter 6, the added mass approaches with beam elements produce vastly different results to the CASA. None of the models can accurately estimate the first eigenvalue, where the error percentage reigns from 21 % to over 28 %. In the third and fifth eigenmode, the increased density and nonstructural mass approaches have good results with error percentages less than 3 % compared to CASA. The minor error percentage estimation happens in eigenmode 3 with 8.74 % for the elbow elements. The MATLAB script produce eigenvalues closest to CASA for all modes, except for the third, when compared to the other beam models. The eigenmodes produced by MATLAB are shown in Figure A.2. They show that the second and thrid modes are swithced, compared to CASA.

Table 7.6 shows that the added mass approaches simulated with beam elements cannot produce reliable estimations for the first five modes. None of the added mass approaches can estimate the correct order of mode shapes or good eigenfrequencies for all first mode shapes compared to CASA. While the added mass models simulated with shell elements estimated bad results in the third and fifth eigenmodes, the added mass models simulated with beam elements produced good results in these modes.

Table 7.5: *The first five egenfrequencies simulated with the increased density and nonstructural mass approach for the beam models, and ABAQUS/Aqua approach for the elbow model*

	Eigenfrequencies [Hz]			
Mode	Increased density	Nonstructural mass	Elbow	MATLAB
1	11.35	11.50	10.70	7.25
2	20.37	20.64	20.88	16.61
3	16.96	17.19	17.25	15.01
4	31.73	32.16	30.11	23.91
5	32.59	33.02	32.80	31.34

Table 7.6: *Comparison of the results simulated with the three added mass models with beam elements in Table 7.5 to the CASA results in Table 7.2*

	% Difference to CASA			
Mode	Increased density	Nonstructural mass	Elbow	MATLAB
1	27	28	21	18
2	16	18	19	4
3	3	2	1	15
4	18	19	13	10
5	2	3	2	2

7.2 Submerged non-symmetrical multi-planar jumper

This section simulates a longer jumper with a different geometry to study the added mass approaches with shell, beam and elbow elements. The jumper being tested is a full-sized model that measures almost 120 m long and has a unique 3D multi-planar geometry that is not symmetrical. The different added mass approaches with shell, beam, and elbow elements will be compared and verified with CASA.

Bruschi et al. (2015) presented a jumper with a 3D non-symmetrical geometry with both ends clamped [67]. The jumper is in Figure 7.9.

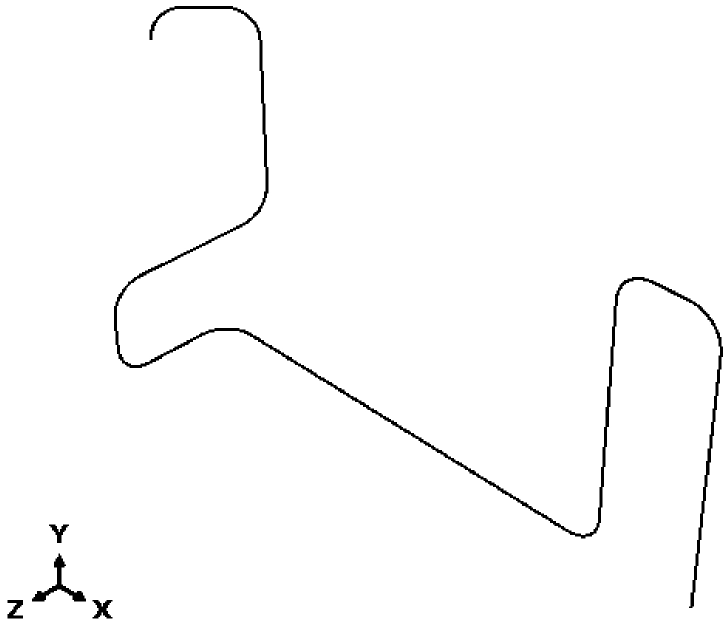

Figure 7.9: *Non-symmetrical jumper geometry*

The jumper dimensions are in Figure 7.10 and Figure 7.11, while the jumper properties are in Table 7.7. The bends are modelled as five times the outer diameter, creating a bending radius equal to 2.286 m. The arch length is 3.591 m, making the total length 118.9 m.

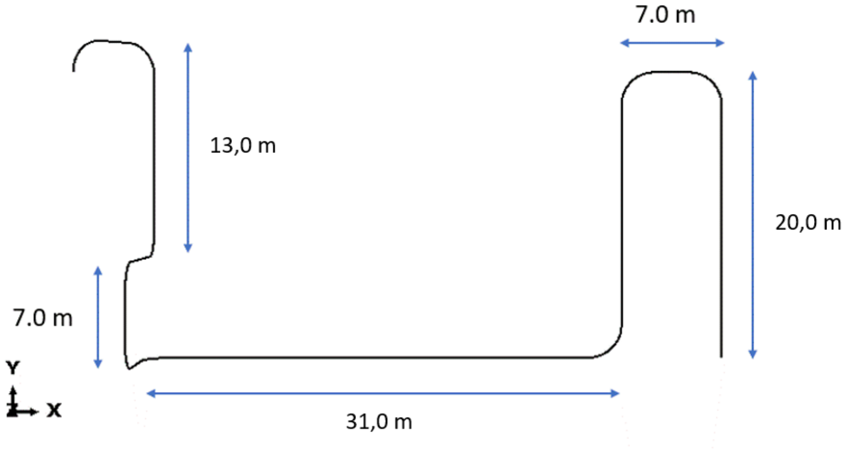

Figure 7.10: *Non-symmetrical jumper dimensions in the XY-plane*

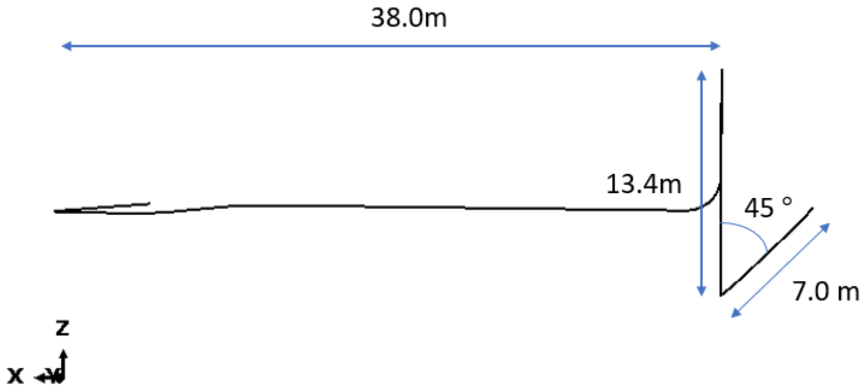

Figure 7.11: *Non-symmetrical jumper dimensions in the XZ-plan*

Table 7.7: *Non-symmetrical jumper properties*

Properties	Value	Unit
Outer diameter	457.2	mm
Thickness	31.8	mm
Elastic Modulus	206.0	GPa
Poisson's ratio	0.3	-
Mass per unit length	555.0	kg/m

7.2.1 Modelling the submerged non-symmetrical multi-planar jumper in ABAQUS

In the CASA model, the jumper is meshed with an approximate mesh size of 0.03 m, creating 184184 linear hexahedral elements of type *C3D8* and 368456 nodes. The EWD of the water domain is four times the outer diameter of the jumper. The model must be heavily partitioned to accurately mesh the water domain, as shown in Figure 7.12. The water domain is meshed using an approximate global mesh size of 0.15 m, resulting in 343178 quadratic hexahedral elements of type *AC3D20* and 1467636 nodes. A visualization of the mesh is in Figure 7.13. The water's bulk modulus and density values are 2.13 GPa and 1000 kg/m^3, respectively. Both ends of the jumper and water domain are fully restrained with clamped boundary conditions.

Three added mass approaches are tested with shell elements: the lumped mass, nonstructural mass, and increased density approaches. The shell models are modelled with an approximate mesh size of 0.05 m, creating 68661 linear quadrilateral elements of type *S4* and 68688 nodes.

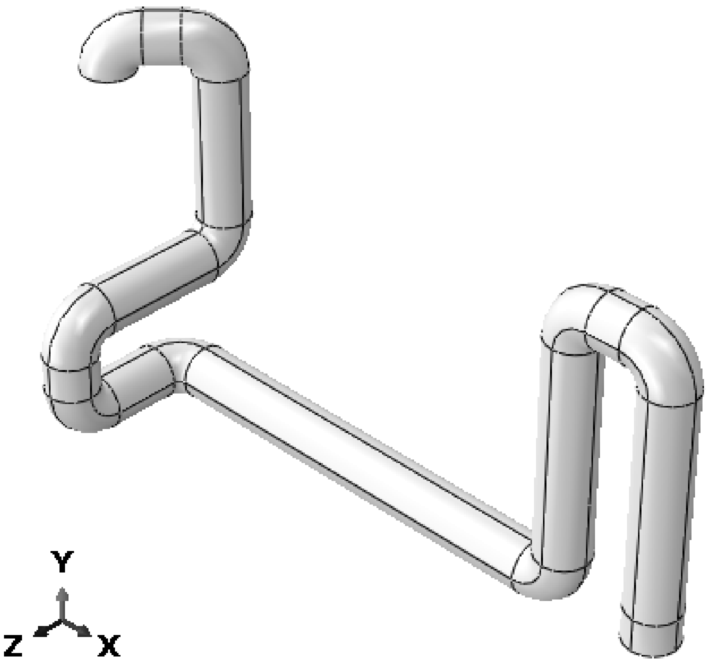

Figure 7.12: *Partitioned model of the water domain*

The beam models are modelled with 315 linear line elements of type *PIPE31*. The nonstructural mass and increased density approaches are tested. The elbow model contained 234 linear line elements of type *PIPE31* for the straight sections and 81 linear line elements of type *ELBOW31* for the bends. ABAQUS/Aqua simulates the added mass in the elbow model.

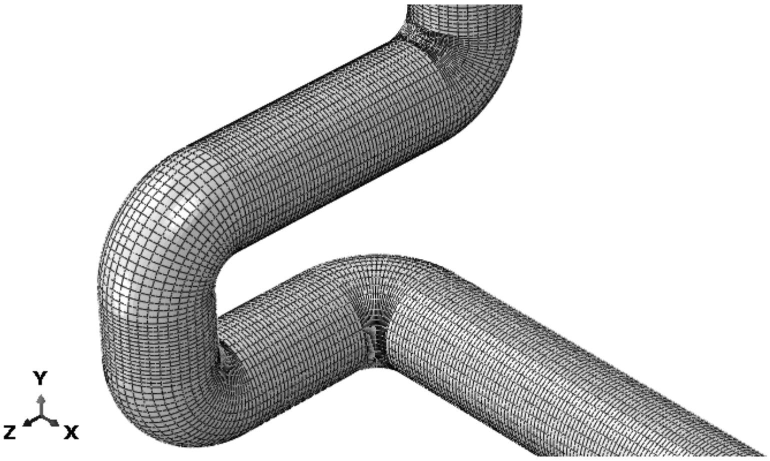

Figure 7.13: *Visual of the water domain mesh*

7.2.2 CASA

Table 7.8 shows the first six eigenfrequencies simulated by CASA, where its corresponding mode shapes are shown in Figure 7.14 to Figure 7.19.

Table 7.8: *Eigenfrequencies of the multi-planar jumper simulated with the CASA model*

Mode	CASA [Hz]
1	0.158
2	0.260
3	0.327
4	0.393
5	0.437
6	0.620

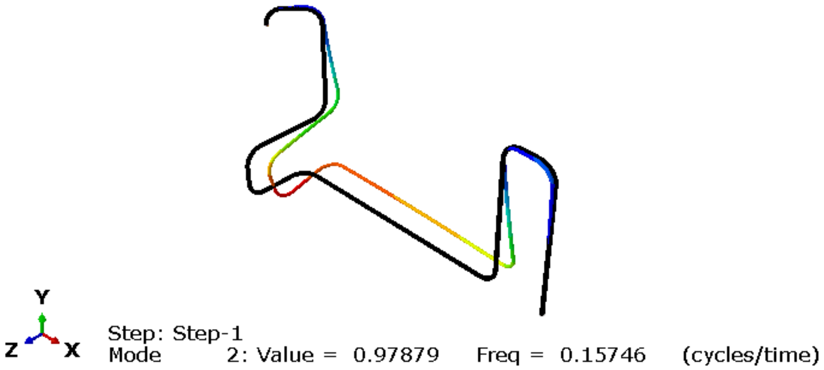

Figure 7.14: *Mode one of the multi-planar jumper. Twisting about the x-axis*

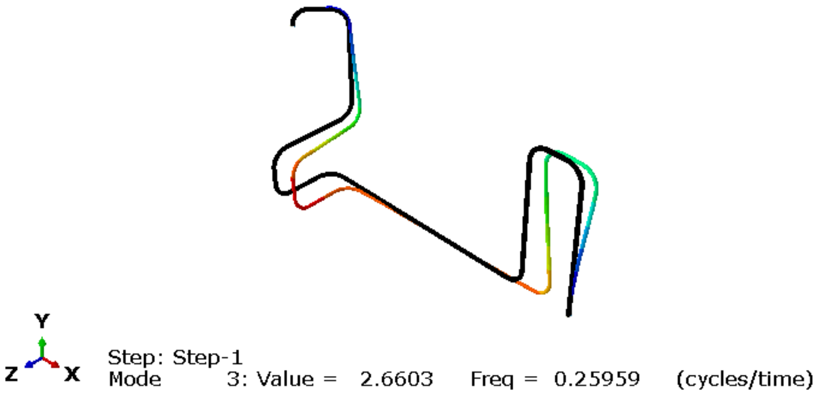

Figure 7.15: *Mode two of the multi-planar jumper. Displacement in the x-direction*

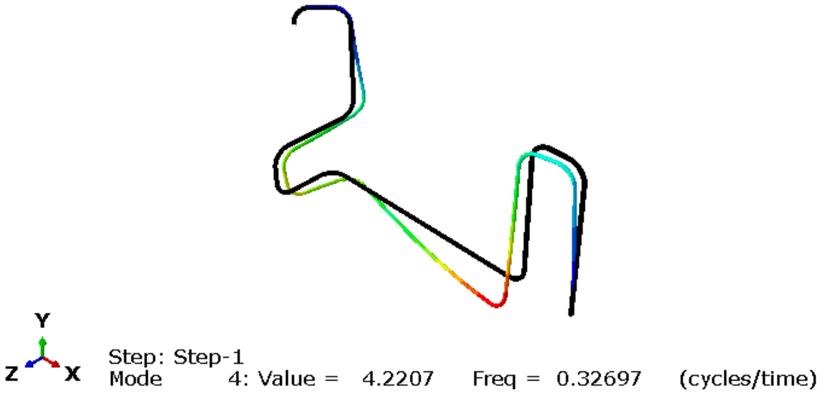

Figure 7.16: *Mode three of the multi-planar jumper. Twisting about the y-axis*

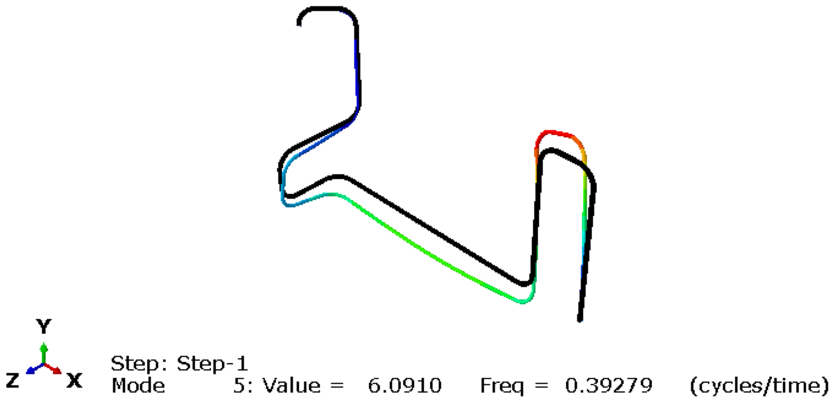

Figure 7.17: *Mode four of the multi-planar jumper. The bottom horizontal bends in the y-direction, while the right vertical bends in the x- and z-direction.*

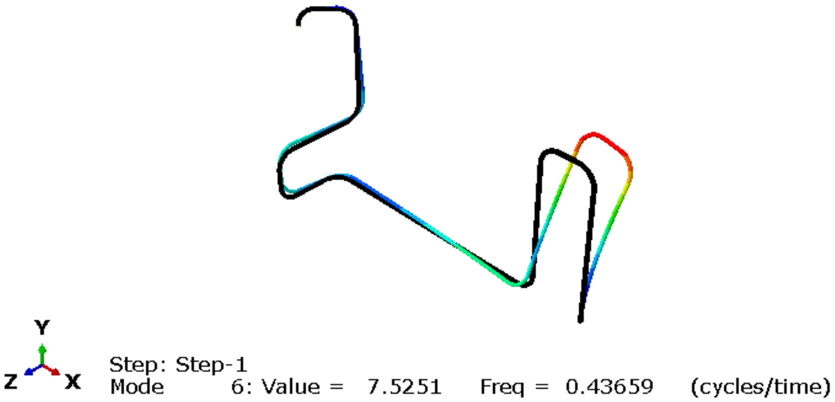

Figure 7.18: *Mode five of the multi-planar jumper. The bottom horizontal twists about the y-axis, while the right vertical bends in the x- and z-direction.*

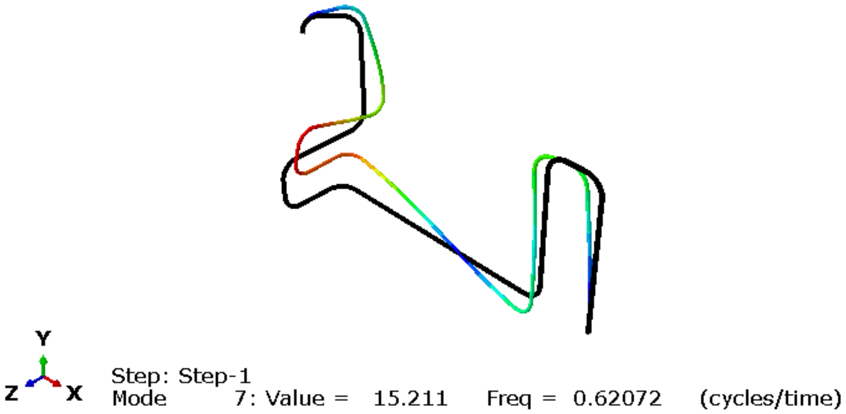

Figure 7.19: *Mode six of the multi-planar jumper. Twisting about the z-axis.*

7.2.3 Shell elements

For the shell models, the lumped mass, increased density, and nonstructural mass approaches are tested. The added mass coefficients are set equal to one, making the total added mass, calculated with Equation (2.26), 19510 kg. The model is meshed with 68688 nodes, making the added mass per node for the lumped mass approach 0.2841 kg. The increased density is set to 16950 kg/m^3.

Table 7.9: *The first six eigenfrequencies of the lumped mass, increased density and nonstructural mass approach simulated with shell elements*

	Eigenfrequencies [Hz]		
Mode	Lumped mass	Increased density	Nonstructural mass
1	0.153	0.152	0.153
2	0.248	0.246	0.248
3	0.321	0.319	0.321
4	0.384	0.382	0.384
5	0.432	0.430	0.432
6	0.603	0.599	0.603

Table 7.10: *Comparison of the results simulated with the three added mass models with shell elements in Table 7.9 to the CASA results in Table 7.8*

	% Difference to CASA		
Mode	Lumped mass	Increased density	Nonstructural mass
1	2.7	3.3	2.7
2	4.7	5.3	4.7
3	1.8	2.4	1.8
4	2.3	2.9	2.3
5	1.0	1.6	1.0
6	2.9	3.5	2.9

Table 7.9 shows the first six eigenfrequencies obtained via the three added mass approaches. Table 7.10 shows the per cent comparisons to CASA. The mode shapes estimated using the three added mass approaches follow the same order as estimated with CASA. The added mass approaches using shell elements provide good results compared to CASA. The lumped and nonstructural mass approaches give almost identical results, while the increased density approach has slightly different results. The second mode shape, where the jumper vibrates in the x-direction, as shown in Figure 7.15, has the most significant error margins. The lumped and nonstructural mass approaches produce results with a 4.67 % and 4.68 % error margin, respectively, while the increased density approach produces results with a 5.28 % error margin.

7.2.4 Beam elements

Table 7.11: *The first six eigenfrequencies simulated with the increased density and nonstructural mass approach for the beam models, and ABAQUS/Aqua approach for the elbow models*

	Eigenfrequencies [Hz]		
Mode	Nonstructural mass	Increased density	Elbow
1	0.158	0.157	0.158
2	0.257	0.255	0.262
3	0.329	0.327	0.329
4	0.391	0.388	0.393
5	0.436	0.433	0.437
6	0.636	0.632	0.630

Table 7.11 shows the first six eigenfrequencies obtained via the three added mass approaches. Table 7.12 shows the per cent comparisons to CASA. The mode shapes estimated with the three added mass approaches are in the exact order as estimated with CASA. Compared to the added mass results with shell elements, Table 7.12 shows more promising results. In the *PIPE31* models, the highest error percentage occurred in the sixth eigenvalue, which was 2.35 %. However, in the elbow model, all errors were below 1.5 % for all eigenmodes.

Table 7.12: *Comparison of the results simulated with the three added mass models with beam elements in Table 7.11 to the CASA results in Table 7.8*

	% Difference to CASA		
Mode	Nonstructural mass	Increased density	Elbow
1	0.5	0.1	0.5
2	1.1	1.8	0.9
3	0.6	0.1	0.5
4	0.6	1.2	0.2
5	0.1	0.7	0.2
6	2.4	1.7	1.4

7.3 Cost-effectiveness analysis

The previous sections provide details on the accuracy of adding mass to different elements compared to the CASA. Section 7.1 shows that none of the added mass models could accurately capture the first five eigenvalues. In contrast, Section 7.2 shows that adding mass to a combination of beam and elbow elements using the ABAQUS/Aqua command is the most accurate approach.

The information presented in Table 7.13 displays the duration of each job and the estimated memory usage by ABAQUS. The results demonstrate that the elbow model for the Z-shaped jumper is significantly faster than the CASA model by a factor of over 8500 and five times faster than the shell models. Additionally, the elbow model requires significantly less memory usage than the CASA model by almost 850 times and over nine times less than the shell models. Similar results were found for the non-symmetrical jumper, where the analysis duration with the elbow model is only one second compared to 9960 and 25 seconds for the CASA and the shell models, respectively. Furthermore, the memory usage of the elbow model is over 1000 times less compared to the CASA model and over 40 times less than the shell models.

Table 7.13: *The time and estimated memory usage of each analysis on adding mass with the CASA, shell elements, and beam and elbow elements on submerged multi-planar jumpers performed by ABAQUS*

	Z-haped jumper		Non-symmetrical jumper	
	Wallclock time [s]	Memory [MB]	Wallclock time [s]	Memory [MB]
CASA	17072	97435	9960	96467
Shell	10	1041	25	4066
Elbow	2	115	1	93

When conducting a modal analysis on submerged multi-planar jumpers, it is important to be careful when adding mass to the beam and elbow elements. For the Z-shaped jumper, the added mass approaches are more cost-effective but less reliable than adding mass with the CASA. However, for the non-symmetrical jumper, adding mass to the beam and elbow elements is both cost-effective and equally reliable as adding mass with the CASA method.

-This page is left initially blank-

Chapter 8

Discussion

This chapter discusses the results obtained in the previous chapters.

8.1 MATLAB script

The MATLAB script, found in Chapter B, could not accurately simulate the eigenfrequencies for the jumpers. Despite trying the *eig*, *eigen*, and *eigs* commands, none of them produced accurate results in comparison to ABAQUS. However, the *eigs* command produced eigenfrequencies close to those simulated by ABAQUS for jumpers with four bends or less, and all mode shapes were in the correct order. A Lanczos algorithm was used in ABAQUS to solve the eigenvalues, which MATLAB lacks a built-in command for. One possible solution could be to implement the same script in Python and use the *eigsh* command.

8.2 Torsional inertia for a submerged straight pipe

Chapter 4 shows that none of the three added mass approaches can correctly simulate the torsional eigenvalue with shell elements and that the difference between the added mass approaches and the CASA is over 50 %. The torsional added mass moment of inertia coefficient per unit length of a circular section in an infinite liquid, as the circular section in the infinite liquid medium rotates along its centre, is listed in Blevins (1984) [38]. Blevins (1984) shows an added mass moment of inertia equal to zero for circular bodies. Therefore, in this mode, the pipe exchanges almost no energy with the surrounding water and is expected to yield the same eigenvalues as if the pipe was in the air. The CASA could correctly simulate this condition while the added mass approaches failed. It has been shown that the velocity potential ϕ for a region around a cylinder vibrating laterally in a reservoir containing stationary fluid can be expressed by [18]

$$\phi = \frac{U(t)r^2[x - X(t)]}{[x - X(t)]^2 + y^2} \tag{8.1}$$

where r is the cylinder radius, $X(t) = \int U(t)dt$ is the position of the cylinder, $U(t)$ is the velocity of the cylinder moving along the x-axis, and x and y are the coordinates of points of interest. A careful examination of the derivation of the added mass term, Equation (2.2), reveals that, in that formulation, the velocity potential has been formulated based on the assumption that a submerged pipe would only vibrate in the lateral direction.

There is a more efficient and affordable way to obtain the eigenvalues of a submerged straight pipe rather than using CASA. This involves running two simulations using shell elements. The first simulation extracts the torsional eigenvalue from a vacuum model, while the second retrieves the lateral bending and ovality values from an added mass model. This method provides accurate results compared to using CASA.

8.3 Submerged jumpers with shell elements

Table 6.4 and Table 6.5 show that the three added mass approaches produce almost identical results when used on shell elements. An investigation was conducted to compare the impacts of varying added mass coefficients on the M-shaped jumper. However, the analysis did not reveal any significant dissimilarities or insights. Regardless of the added mass coefficients utilized, the different added mass approaches with shell elements all end up with the same conclusions.

In Chapter 6, specifically in Section 6.1.4 and Section 6.2.3, it is clear that the eigenfrequencies estimated in the in-plane bending modes with shell elements are vastly lower from the CASA estimations. For the in-plane bending modes, the shell models estimates that the jumpers exchange more energy with the surrounding water than the CASA model. The eigenfrequency decrease is likely due to the poor rotary scaling, as the shell models are convergent in terms of discretization.

Rotational inertia is a property of a physical object that describes its resistance to rotational motion. It depends on both the mass of the object and the distribution of that mass relative to the axis of rotation. Rotary inertia is a type of rotational inertia that refers explicitly to the rotational inertia of a spinning disk or, in this case, a cylinder around its axis of rotation. For thin shell elements, the rotary inertia I_3, listed in Equation (2.52), is small or negligible relative to the rotational inertia of the mass at the nodes. Therefore, ABAQUS chose a scaling on the rotary inertia such that it never becomes smaller than a fixed, tiny percentage of the rotational inertia of the mass at the nodes rotating about an axis through the centre of the element [9].

When analyzing the transverse shear response, the rotary inertia I_3 is crucial as it represents the system's mass and is proportional to the cube of the thickness. Other quantities, such as transverse shear stiffness and membrane stiffness, are proportional to the thickness. As the element's thickness approaches zero, transverse shear frequencies increase infinitely since they are inversely proportional to thickness, while membrane frequencies remain constant. Without proper scaling, the stable time increment would go to zero as thickness decreases. In dynamic analyses, the stable time increment is proportional to the inverse of the highest frequency of the element [9]. The primary consideration in choosing appropriate scalings is that the transverse shear frequencies remain below the membrane ones in the limit as the element's thickness goes towards zero.

To better comprehend how rotary scaling affects eigenvalues, let R be the non-dimensional rotary inertia scaling, where $R \geq 1$. When $R = 1$, the true rotary inertia is used. One can imagine the natural frequency ω expressed in relation to mass M and stiffness K as

$$\omega = \sqrt{\frac{K}{M}} \tag{8.2}$$

When the bends are subjected to in-plane bending modes, they stretch on the outside and squeeze on the inside, as shown in Chapter 5, resulting in in-plane bending for the shell elements. For thin shell elements, the rotary inertia is small or negligible relative to the rotational inertia. When the rotary inertia scaling R becomes greater than one, the inertia effects in the mass matrix **M** increase, and the eigenvalues decrease, as shown in Equation (8.2). Using a heavy material model, by adding a high-density value or additional mass, the inertia effects in the mass matrix will increase too much, leading to too low natural frequencies in the in-plane bending modes.

Shell elements typically have a three-dimensional bending stiffness matrix, which includes the through-thickness stiffness terms that are negligible for in-plane bending modes. Therefore, when shell elements are used to calculate the natural frequencies and mode shapes for in-plane bending modes, the through-thickness stiffness terms may introduce additional spurious modes that do not represent the actual physical behaviour of the structure. This can also lead to inaccurate predictions of the in-plane mode shapes.

The jumper is modelled with *S4* elements, a fully integrated finite-membrane-strain shell element [9]. Since the element's stiffness is fully integrated, no spurious membrane or bending zero energy modes exist, and no membrane or bending mode hourglass stabilization is used. It is well known that a standard displacement formulation will exhibit shear locking for applications dominated by in-plane bending deformation. Shear locking occurs when a shell element becomes overly stiff and cannot accurately represent deformations in the in-plane direction. This can happen because shell elements are typically formulated using a two-dimensional approach that assumes the shell is thin and has a constant thickness. However, when the thickness of the shell is comparable to the length of the element, the two-dimensional approach becomes less accurate and shear locking can occur. This can lead to inaccurate predictions of in-plane mode shapes in modal analysis. However, a standard displacement formulation for the out-of-plane bending stiffness is not subject to a similar locking response. Various techniques have been developed to address the shear locking issue, such as reducing the aspect ratio of the shell element, using higher-order elements, or employing special stabilization techniques [68, 69].

8.4 Beam elements in multi-planar jumpers

In Section 7.1, the beam and elbow models estimated eigenvalues vastly differently than CASA. When working with beam elements, the thickness and cross-section of the structure remain constant. However, elbow elements can simulate ovalities in the elbows but not in the straight parts. In the case of the jumpers discussed in Chapter 6 and Section 7.2, the straight pipes did not experience ovalities. For the jumper in Section 7.1, the top horizontals (S2 and S6 in Figure 7.1) are 0.5 m long, with bends on each side measuring 0.156 m, making the straight part 0.344 m long. During bending and twisting modes, the top horizontal straights of the structure experience ovalities. However, the *PIPE31* elements used to model the straight parts cannot account for changes in cross-sections, leading to inaccurate estimations.

In Section 7.1, the added mass models simulated with shell elements estimate bad results in the third and fifth eigenmodes, and the added mass models simulated with beam elements produce good results in these modes. Adding mass with shell elements produces closer results to CASA for all the other modes. The mode shapes of the third and fifth eigenmodes are shown from the x-direction in Figure 8.1 and Figure 8.2, respectively. They show rotation in the top horizontal straight pipes, resulting in in-plane bending modes for the jumper's middle and most significant part. Chapter 4 demonstrates that using the lumped mass, nonstructural mass, and increased density approach with shell elements on a straight pipe leads to incorrect estimates in the torsional mode. Table 4.5 indicates that ABAQUS/Aqua simulation does not increase the rotary inertia when adding mass to a straight pipe. This could be why beam elements performed better than shell elements in the third and fifth eigenmodes.

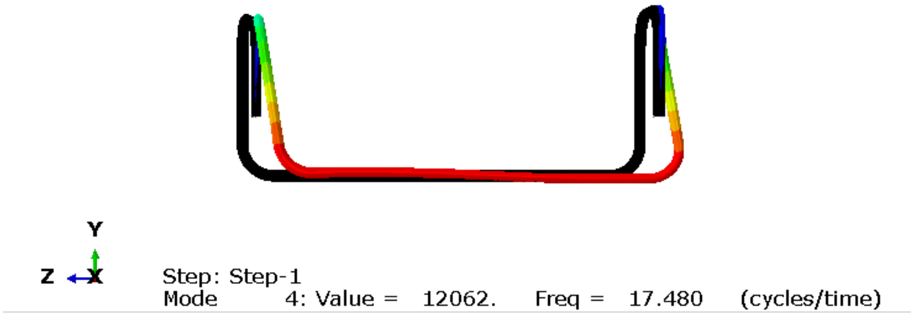

Figure 8.1: *Mode three of the multi-plane jumper from the CASA. Seen in the Y-Z-plane*

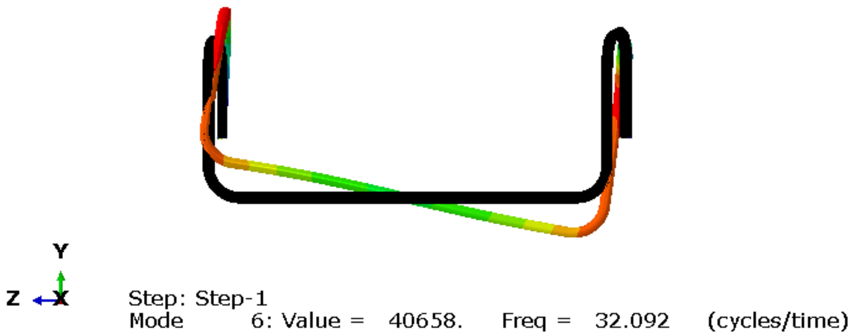

Figure 8.2: *Mode five of the multi-plane jumper from the CASA. Seen in the Y-Z-plane*

The theory behind the added mass models is described in Section 2.1. It is adapted from Blevins' added mass term, initially formulated for analyzing the vibration of a submerged beam [18]. The results shown in Table 7.5 and Table 7.6 indicate that the multi-planar jumper does not behave like a beam but behaves more like a shell model. When conducting a dynamic analysis, the model of the jumper varies depending on the approach taken. The jumper is represented with a consistent cross-section and thickness if beam elements are used. However, if the CASA approach is used, the model includes solid elements that account for variations in the cross-section and thickness. For the multi-planar jumper, it is crucial to account for changes in cross-section and thickness as the structure becomes less rigid and the eigenfrequencies decrease. This causes the jumper to behave more like a stiffened shell model and less like a beam.

A study was conducted to investigate the relationship between the outer diameter to total length (OD/TL) ratio and the jumper's behaviour change. However, the analysis did not uncover any significant findings or new insights into the behaviour of jumpers, despite the different ratios tested. The study showed that shell elements generally produced better results than beam and elbow elements, even when the jumper's behaviour resembled a beam rather than a shell model. Thus, caution must be exercised when using beam and elbow elements for multi-planar jumpers.

Chapter 9

Conclusions

9.1 Concluding remarks

The performance and accuracy of different approaches to adding mass for modelling the dynamic response of submerged structures in the context of FSI were investigated. The investigation included the evaluation of the eigenvalues of submerged pipes and jumpers modelled by different approaches.

For straight pipes, the simulated eigenfrequency corresponding to the torsional mode has a vastly lower eigenfrequency with the lumped mass, nonstructural mass, and increased density approaches with shell elements compared to the CASA. In this mode, the pipe exchange almost no energy with the surrounding water and is expected to yield the same eigenvalue as in the air. Using ABAQUS/Aqua to simulate added mass on beam elements solves the problem. By coding, it is possible to set the twisting moments in the added mass matrix equal to zero. If modelling with shell elements, it is recommended to run two simulations, one with an added mass approach where the lateral bending and ovality values are extracted, and one in a vacuum, where the torsional value is extracted.

The eigenfrequencies increase by modelling a bend with thickness variation to simulate the ovalization, adding mass, and running a modal analysis. The difference between the ovalized pipes compared to the non-ovalized was less than 0.05 % for both the thick and thin pipes. By including the cross-sectional out-of-roundness, the eigenfrequencies decrease, and the differences increase to more than 17 % at its peak for thick pipes and almost 13 % for thin pipes. Compared to non-ovalized pipes simulated with beam elements, the differences increased to 24 % for the thin pipe and 18 % for the thick. The study suggests that modelling the ovalization is essential as it significantly affects the eigenvalues due to the change in cross-section. Therefore, it is highly recommended to consider this factor.

By modelling the subsea jumpers in a 2D plane with shell elements and simulating the submerged eigenvalues with added mass approaches, the in-plane bending values were vastly different compared to the CASA results. However, modelling the submerged jumpers with beam elements produce better results with less than five per cent difference to CASA for any mode. By including elbow elements in the beam models, the per cent differences become less than one per cent compared to CASA. When conducting a modal analysis on a submerged single-planar jumper, adding mass using ABAQUS/Aqua to the beam and elbow elements is recommended. This method is cost-effective and as reliable as using the CASA.

Adding mass with ABAQUS/Aqua to beam and elbow elements produced good results for some multi-planar jumpers. However, caution must be put in as some multi-planar jumper geometries work better with shell elements, even if the jumper behaves more like a beam than a shell model.

9.2 Suggestions for Future Work

Some recommendations for future work are as follows:

Include internal and external pressure in the analysis to observe stiffening and softening effects for the full jumper models. Any change in a pipe's internal or external pressure would change its overall stiffness, affecting its vibration response. For example, in the case of an underwater pipeline, the internal fluid's pressure or the external hydrostatic pressure would affect the apparent stiffness of the pipe, thereby changing the pipe's eigenvalues and dynamic response.

Run added mass simulations with continuum shell elements. Continuum shells discretize an entire three-dimensional body, unlike conventional shells, which discretize a reference surface and are more suitable for simulating the jumper's in-plane bending mode shapes.

Simulate a multi-planar jumper model when the central part is placed horizontally and touching the seabed.

Formulate an analytical added mass term for analyzing the vibration of a submerged jumper with shell elements.

-This page is left initially blank-

References

[1] Wenhua Li, Wenrui Song, Guang Yin, Muk Chen Ong, and Fenghui Han. Flow regime identification in the subsea jumper based on electrical capacitance tomography and convolution neural network. *Ocean Engineering*, 266:113152, 2022. ISSN 0029-8018. doi: https://doi.org/10.1016/j.oceaneng.2022.113152. URL `https://www.sciencedirect.com/science/article/pii/S0029801822024350`.

[2] Jung Kim. Design parameter characteristics in a subsea rigid jumper. *Journal of Applied Mechanical Engineering*, 04, 01 2015. doi: 10.4172/2168-9873.1000162.

[3] Yong Bai and Qiang Bai. *Subsea Engineering Handbook*. Oxford: Elsevier, 1 edition, 2012. ISBN 9780123978059. URL `https://www.elsevier.com/books/subsea-engineering-handbook/bai/978-0-12-397804-2`.

[4] Zhenhui Liu, Laila Aarstad Igeh, Jie Wu, and Muk Chen Ong. Fatigue Damage Assessment to a Rigid Planar Jumper on Model Scale. *Journal of Offshore Mechanics and Arctic Engineering*, 142(1), 07 2019. ISSN 0892-7219. doi: 10.1115/1.4044074. URL `https://doi.org/10.1115/1.4044074`. 011602.

[5] Linda Sieber, Zhenhui Liu, Svein Sævik, and Jonas Ringsberg. Assessment of vortex-induced vibration fatigue of subsea template jumper by using a time domain model. Master's thesis, Norwegian University of Science and Technology, https://hdl.handle.net/11250/2989641, 7 2021.

[6] Sherif S. Sorour, Mostafa Shazly, and Mohammad M. Megahed. Limit load analysis of thin-walled as-fabricated pipe bends with low ovality under in-plane moment loading and internal pressure. *Thin-Walled Structures*, 144:106336, 2019. ISSN 0263-8231. doi: https://doi.org/10.1016/j.tws.2019.106336. URL `https://www.sciencedirect.com/science/article/pii/S026382311930309X`.

[7] S. Sumesh, AR. Veerappan, and S. Shanmugam. Evaluation of postulated cross sections with ovality and thinning for 90¬ pipe bends with circumferential throughwall cracks subjected to in-plane closing bending. *Engineering Failure Analysis*, 75:82–91, 2017. ISSN 1350-6307. doi: https://doi.org/10.1016/j.engfailanal.2016.12.021. URL `https://www.sciencedirect.com/science/article/pii/S1350630716306148`.

[8] Jaswar Koto. *Subsea Connection Jumper - Introduction*. Ocean Aerospace Research Institute, Indonesia, 2 edition, 2017.

[9] Simulia. Abaqus/standard user's manual, version 6.9, 2009.

[10] F. Ross. *Pressure vessels: External Pressure Technology*. Horwood Publishing, 2001.

[11] J.P. Gauthier, A.M. Giroux, S. Etienne, and F.P. Gosselin. A numerical method for the determination of flow-induced damping in hydroelectric turbines. *Journal of Fluids and Structures*, 69:341–354, 2017. ISSN 0889-9746. doi: https://doi.org/10.1016/j.jfluidstructs.2017.01.004. URL `https://www.sciencedirect.com/science/article/pii/S0889974616301773`.

[12] Chirag Trivedi. A review on fluid structure interaction in hydraulic turbines: A focus on hydrodynamic damping. *Engineering Failure Analysis*, 77:1–22, 2017. ISSN 1350-6307. doi: https://doi.org/10.1016/j.engfailanal.2017.02.021. URL `https://www.sciencedirect.com/science/article/pii/S1350630717302704`.

[13] Li Lu, Yi Ren Yang, Peng Li, and Ming Lu Zhang. Added mass, added stiffness and added damping coefficients for a parallel plate-type structure. In *Mechanical, Materials and Manufacturing Engineering*, volume 66 of *Applied Mechanics and Materials*, pages 1738–1742. Trans Tech Publications Ltd, 8 2011. doi: 10.4028/www.scientific.net/AMM.66-68.1738.

[14] Xue-linp. Peng and Hong. Hao. A numerical study of damage detection of underwater pipeline using vibration-based method. *International Journal of Structural Stability and Dynamics*, 12, 05 2012. doi: 10.1142/S0219455412500216.

[15] Xue-Lin. Peng, Hong. Hao, and Zhong-Xian. Li. Application of wavelet packet transform in subsea pipeline bedding condition assessment. *Engineering Structures*, 39:50–65,

2012. ISSN 0141-0296. doi: https://doi.org/10.1016/j.engstruct.2012.01.017. URL `https://www.sciencedirect.com/science/article/pii/S0141029612000570`.

[16] X. Q. Zhu, H. Hao, and X. L. Peng. Dynamic assessment of underwater pipeline systems using statistical model updating. *International Journal of Structural Stability and Dynamics*, 08(02):271–297, 2008. doi: 10.1142/S021945540800265X. URL `https://doi.org/10.1142/S021945540800265X`.

[17] Chunxiao Bao, Hong Hao, and Zhongxian Li. Vibration-based structural health monitoring of offshore pipelines: Numerical and experimental study. *Structural Control and Health Monitoring*, 20, 05 2013. doi: 10.1002/stc.1494.

[18] R.D. Blevins. *Flow-induced Vibration*. Krieger Publishing Company, 2001. ISBN 9781575241838. URL `https://books.google.no/books?id=Wzo8PgAACAAJ`.

[19] Matthew R. Kramer, Zhanke Liu, and Yin L. Young. Free vibration of cantilevered composite plates in air and in water. *Composite Structures*, 95:254–263, 2013. ISSN 0263-8223. doi: https://doi.org/10.1016/j.compstruct.2012.07.017. URL `https://www.sciencedirect.com/science/article/pii/S0263822312003455`.

[20] Cho-Chung Liang, Ching-Chao Liao, Yuh-Shiou Tai, and Wen-Hao Lai. The free vibration analysis of submerged cantilever plates. *Ocean Engineering*, 28(9):1225–1245, 2001. ISSN 0029-8018. doi: https://doi.org/10.1016/S0029-8018(00)00045-7. URL `https://www.sciencedirect.com/science/article/pii/S0029801800000457`.

[21] Ulric S. Lindholm, Daniel D. Kana, Wen-Hwa Chu, and H. Norman Abramson. Elastic vibration characteristics of cantilever plates in water. *Journal of Ship Research*, 9:11–36, 1962.

[22] Kyeong-Hoon Jeong, Gyu-Mahn Lee, and Tae-Wan Kim. Free vibration analysis of a circular plate partially in contact with a liquid. *Journal of Sound and Vibration*, 324(1): 194–208, 2009. ISSN 0022-460X. doi: https://doi.org/10.1016/j.jsv.2009.01.061. URL `https://www.sciencedirect.com/science/article/pii/S0022460X0900128X`.

[23] Jiangang Chen and Zhongqing Su. Identification of corrosion damage in submerged structures using fundamental anti-symmetric lamb waves. *Smart Materials and Structures*, 19:015004, 11 2009. doi: 10.1088/0964-1726/19/1/015004.

[24] Irena Lasiecka and José H. Rodrigues. Weak and strong semigroups in structural acoustic kirchhoff-boussinesq interactions with boundary feedback. *Journal of Differential Equations*, 298:387–429, 2021. ISSN 0022-0396. doi: https://doi.org/10.1016/j.jde.2021.07.009. URL `https://www.sciencedirect.com/science/article/pii/S0022039621004460`.

[25] H.T. Banks, M.A. Demitriou, and R.C. Smith. An h/sup /spl infin///minmax periodic control in a two-dimensional structural acoustic model with piezoceramic actuators. *IEEE Transactions on Automatic Control*, 41(7):943–959, 1996. doi: 10.1109/9.508899.

[26] J. Beale. Spectral properties of an acoustic boundary condition. *Indiana Univ. Math. J.*, 25:895–917, 1976. ISSN 0022-2518.

[27] H.T. Banks and R.C. Smith. Feedback control of noise in a 2-d nonlinear structural acoustics model. *Discrete and Continuous Dynamical Systems*, 1(1):119–149, 1995. doi: 10.3934/dcds.1995.1.119. URL `https://doi.org/10.3934/dcds.1995.1.119`.

[28] Fariba Fahroo and Chunming Wang. A new model for acoustic-structure interaction and its exponential stability. *Quarterly of Applied Mathematics*, 57(1):157–179, 1999. ISSN 0033-569X. doi: 10.1090/qam/1672195. URL `https://doi.org/10.1090/qam/1672195`.

[29] P. M. Morse, K. U. Ingard, and F. B. Stumpf. Theoretical Acoustics. *American Journal of Physics*, 38(5):666–667, 05 1970. ISSN 0002-9505. doi: 10.1119/1.1976432. URL `https://doi.org/10.1119/1.1976432`.

[30] I Author Lasiecka and GC Reviewer Gaunaurd. Mathematical Control Theory of Coupled PDEs. *Applied Mechanics Reviews*, 56(1):B3–B3, 01 2003. ISSN 0003-6900. doi: 10.1115/1.1523354. URL `https://doi.org/10.1115/1.1523354`.

[31] Y.H. Wu, C.Y. Dong, and H.S. Yang. Isogeometric fe-be coupling approach for structural-acoustic interaction. *Journal of Sound and Vibration*, 481:115436, 2020. ISSN 0022-460X. doi: https://doi.org/10.1016/j.jsv.2020.115436. URL `https://www.sciencedirect.com/science/article/pii/S0022460X20302686`.

[32] C.G. Rodriguez, P. Flores, F.G. Pierart, L.R. Contzen, and E. Egusquiza. Capability of structural–acoustical fsi numerical model to predict natural frequencies of submerged structures with nearby rigid surfaces. *Computers Fluids*, 64:117–126, 2012.

ISSN 0045-7930. doi: https://doi.org/10.1016/j.compfluid.2012.05.011. URL `https://www.sciencedirect.com/science/article/pii/S0045793012002113`.

[33] Pejman Razi and Farid Taheri. A vibration-based strategy for health monitoring of offshore pipelines' girth-welds. *Sensors*, 14(9):17174–17191, 2014. ISSN 1424-8220. doi: 10.3390/s140917174. URL `https://www.mdpi.com/1424-8220/14/9/17174`.

[34] Pejman Razi and Farid Taheri. On the vibration simulation of submerged pipes: Structural health monitoring aspects. *Journal of Mechanics of Materials and Structures*, 10: 105–122, 08 2015. doi: 10.2140/jomms.2015.10.105.

[35] M. Zeinoddini, G.A.R. Parke, and M.Sadrossadat. Free-spanning submarine pipeline response to severe ground excitations: Water-pipeline interactions. *PIPELINE SYSTEMS ENGINEERING AND PRACTICE*, 3, 11 2012. doi: 10.1061/(ASCE)PS.1949-1204.0000098.

[36] Ming Zhang and Qing guang Chen. Numerical investigation of the added mass effect of submerged blade disk structures: From simplified models to francis turbine runners. *Alexandria Engineering Journal*, 61(4):3013–3020, 2022. ISSN 1110-0168. doi: https://doi.org/10.1016/j.aej.2021.08.026. URL `https://www.sciencedirect.com/science/article/pii/S111001682100541X`.

[37] MathWorks. Matlab version: 9.13.0 (r2022b), 2022. URL `https://www.mathworks.com`.

[38] R.D. Blevins. *Formulas for Natural Frequency and Mode Shape*. R.E. Krieger, 1984. ISBN 9780898747911. URL `https://books.google.no/books?id=ZexnjgEACAAJ`.

[39] J.N. Newman. *Marine Hydrodynamics*. Mit Press. Wei Cheng Cultural Enteroprise Company, 1977. ISBN 9780262140263. URL `https://books.google.co.uk/books?id=nj-k_lAmaBYC`.

[40] Lund University. *CALFEM – A Finite Element Toolbox Version 3.6*. 2022. Available at `http://www.byggmek.lth.se/Calfem`.

[41] J.S. Przemieniecki. *Theory of Matrix Structural Analysis*. Dover Civil and Mechanical Engineering. Dover, 1985. ISBN 9780486649481. URL `https://books.google.no/books?id=Jd6iOk4wvtQC`.

[42] André Teófilo Beck and Cláudio R.A. da Silva. Timoshenko versus euler beam theory: Pitfalls of a deterministic approach. *Structural Safety*, 33(1):19–25, 2011. ISSN 0167-4730. doi: https://doi.org/10.1016/j.strusafe.2010.04.006. URL `https://www.sciencedirect.com/science/article/pii/S0167473010000597`.

[43] Edgar Matas Hidalgo. *Study of optimization for vibration absorbing devices applied on airplane structural elements*. PhD thesis, UPC, Escola Tècnica Superior d'Enginyeries Industrial i Aeronàutica de Terrassa, Departament de Projectes d'Enginyeria, Jun 2014. URL `http://hdl.handle.net/2099.1/26029`.

[44] Maurice Petyt. *Introduction to Finite Element Vibration Analysis*. Cambridge University Press, 2 edition, 2010. doi: 10.1017/CBO9780511761195.

[45] Robert D. Cook, David S. Malkus, Michael E. Plesha, and Robert J. Witt. *Concepts and Applications of Finite Element Analysis, 4th Edition*. Wiley, 4 edition, October 2001. ISBN 0471356050.

[46] T. Aksu. A finite element formulation for free vibration analysis of shells of general shape. *Computers Structures*, 65(5):687–694, 1997. ISSN 0045-7949. doi: https://doi.org/10.1016/S0045-7949(96)00423-3. URL `https://www.sciencedirect.com/science/article/pii/S0045794996004233`.

[47] Jingjuan Zhai, Guozhong Zhao, and Linyuan Shang. Integrated design optimization of structural size and control system of piezoelectric curved shells with respect to sound radiation. *Structural and Multidisciplinary Optimization*, 56:1–18, 12 2017. doi: 10.1007/s00158-017-1721-5.

[48] N. Kumbasar and T. Aksu. A finite element formulation for moderately thick shells of general shape. *Computers Structures*, 54(1):49–57, 1995. ISSN 0045-7949. doi: https://doi.org/10.1016/0045-7949(94)00304-L. URL `https://www.sciencedirect.com/science/article/pii/004579499400304L`.

[49] T. Zimmermann. The finite element method. Linear static and dynamic finite element analysis Thomas J.R. Hughes (Prentice Hall, Englewood Cliffs, NJ, 1987) 803 pp. *Computer Methods in Applied Mechanics and Engineering*, 65(2):191, November 1987. doi: 10.1016/0045-7825(87)90013-2.

[50] Demetres Briassoulis. On the basics of the shear locking problem of c0 isoparametric plate elements. *Computers Structures*, 33(1):169–185, 1989. ISSN 0045-7949. doi: https://doi.org/10.1016/0045-7949(89)90139-9. URL `https://www.sciencedirect.com/science/article/pii/0045794989901399`.

[51] D. Briassoulis. Thin element applications of a new formulation for c0 structural elements. *Computers Structures*, 37(6):1097–1103, 1990. ISSN 0045-7949. doi: https://doi.org/10.1016/0045-7949(90)90021-S. URL `https://www.sciencedirect.com/science/article/pii/004579499090021S`.

[52] H. D. Hibbit. Special structural elements of piping analysis. In *Pressure Vessels and Piping: Analysis and Computers*, New York, 1974. ASME.

[53] H. Ohtsubo and O. Watanabe. Flexibility and stress factors for pipe bends—an analysis by the finite ring method. In *ASME paper 76-PVP-40*, 1976.

[54] H. Takeda, S. Asai, and K. Kwata. A new finite element for structural analysis of piping systems. In *Proceedings of the Fifth SMIRT Conference*, Berlin, 1979.

[55] K. Bathe and C. Almeida. A simple and effective pipe elbow element—linear analysis. *Journal of Applied Mechanics-transactions of The Asme - J APPL MECH*, 47, 03 1980. doi: 10.1115/1.3153645.

[56] Nils Erik Anders Rønnquist, Federico Perotti, and Luca Martinelli. Global analysis of submerged floating tunnels under hydrodynamic loading. Master's thesis, Norwegian University of Science and Technology, 6 2020.

[57] O. C Zienkiewicz. The finite element method : its basis and fundamentals, 2005.

[58] Roger Ohayon. Symmetric variational formulation of harmonic vibrations problems by coupling primal and dual principles. Application to fluid-structure coupled systems. *La Recherche Aerospatiale*, 3:207–2011, 1979. URL `https://hal.science/hal-04105338`.

[59] Oskar Ullestad and Zhenhui Liu. The application of the coupled acoustic-structural approach (casa) method on the free vibration of submerged structures. 2023. submitted for review.

[60] Wen Hwa Chu. Vibrations of fully submerged cantilever plates in water. *Schiffstechnik*, 15(78):–, 1968. URL `https://repository.tudelft.nl/islandora/object/uuid%3Abbd2ee9a-e527-4b51-8890-7dd12c7e5244`.

[61] Cong Gao, Hang Zhang, Haichao Li, Fuzhen Pang, and Hongfu Wang. Numerical and experimental investigation of vibro-acoustic characteristics of a submerged stiffened cylindrical shell excited by a mechanical force. *Ocean Engineering*, 249:110913, 2022. ISSN 0029-8018. doi: https://doi.org/10.1016/j.oceaneng.2022.110913. URL `https://www.sciencedirect.com/science/article/pii/S0029801822003493`.

[62] David Valentín, Alexandre Presas, Eduard Egusquiza, Carme Valero, and Mònica Egusquiza. Experimental Study of a Vibrating Disk Submerged in a Fluid-Filled Tank and Confined With a Nonrigid Cover. *Journal of Vibration and Acoustics*, 139(2), 02 2017. ISSN 1048-9002. doi: 10.1115/1.4035105. URL `https://doi.org/10.1115/1.4035105`. 021005.

[63] Howard Wang, Jerry Huang, Sungho Lee, Paulo Gioielli, Wan Kan, Don Spencer, and Mohammed Islam. VIV Response of a Subsea Jumper in Uniform Current. Volume 4B: Pipeline and Riser Technology, 06 2013. doi: 10.1115/OMAE2013-11417. URL `https://doi.org/10.1115/OMAE2013-11417`. V04BT04A043.

[64] Klaus-Jurgen Bathe, Carlos A. Almeida, and Lee W. Ho. A simple and effective pipe elbow element—some nonlinear capabilities. In K.J. BATHE, editor, *Nonlinear Finite Element Analysis and Adina*, pages 659–667. Pergamon, 1983. ISBN 978-0-08-030566-0. doi: https://doi.org/10.1016/B978-0-08-030566-0.50009-6. URL `https://www.sciencedirect.com/science/article/pii/B9780080305660500096`.

[65] R. Bruschi, A. Parrella, G.C. Vignati, and L. Vitali. Crucial issues for deep water rigid jumper design. *Ocean Engineering*, 137:193–203, 2017. ISSN 0029-8018. doi: https://doi.org/10.1016/j.oceaneng.2017.03.059. URL `https://www.sciencedirect.com/science/article/pii/S0029801817301762`.

[66] Wenhua Li, Qing Zhou, Guang Yin, Muk Chen Ong, Gen Li, and Fenghui Han. Experimental investigation and numerical modeling of two-phase flow development and flow-induced vibration of a multi-plane subsea jumper. *Journal of Marine Science*

and Engineering, 10(10), 2022. ISSN 2077-1312. doi: 10.3390/jmse10101334. URL `https://www.mdpi.com/2077-1312/10/10/1334`.

[67] Roberto Bruschi, Lorenzo Bartolini, Caterina Molinari, Giulio C. Vignati, and Luigino Vitali. VIV Basics for Subsea Spool/Jumper Design. volume Volume 5A: Pipeline and Riser Technology of *International Conference on Offshore Mechanics and Arctic Engineering*, 05 2015. doi: 10.1115/OMAE2015-41094. URL `https://doi.org/10.1115/OMAE2015-41094`. V05AT04A006.

[68] Richard H. Macneal. A simple quadrilateral shell element. *Computers Structures*, 8(2): 175–183, 1978. ISSN 0045-7949. doi: https://doi.org/10.1016/0045-7949(78)90020-2. URL `https://www.sciencedirect.com/science/article/pii/0045794978900202`.

[69] Eduardo N. Dvorkin and Klaus-Jürgen Bathe. A continuum mechanics based four-node shell element for general non-linear analysis. *Engineering Computations*, 1(1): 77–88, 1984. ISSN 0264-4401. doi: 10.1108/eb023562. URL `https://doi.org/10.1108/eb023562`.

Appendices

Appendix A

MATLAB plots

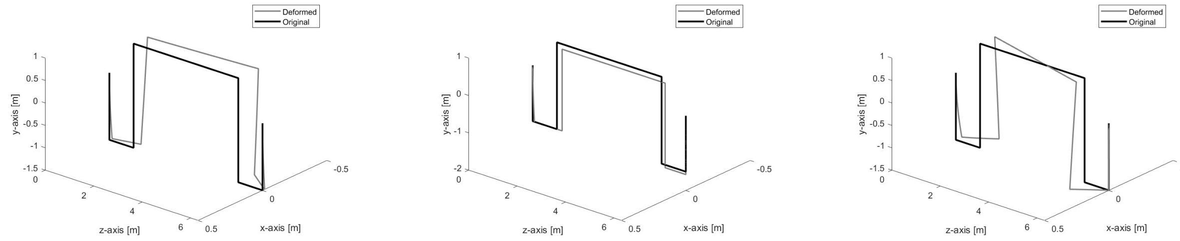

*(**a**) Mode 1* *(**b**) Mode 2* *(**c**) Mode 3*

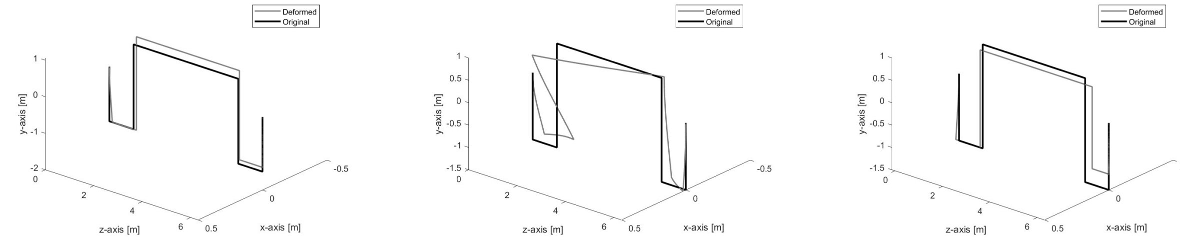

*(**d**) Mode 4* *(**e**) Mode 5* *(**f**) Mode 6*

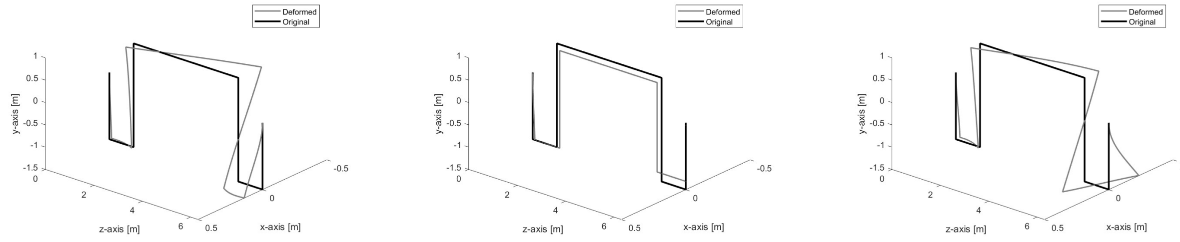

*(**g**) Mode 7* *(**h**) Mode 8* *(**i**) Mode 9*

Figure A.1: *The first nine mode shapes of the submerged M-shaped single-planar jumper, simulated with MATLAB*

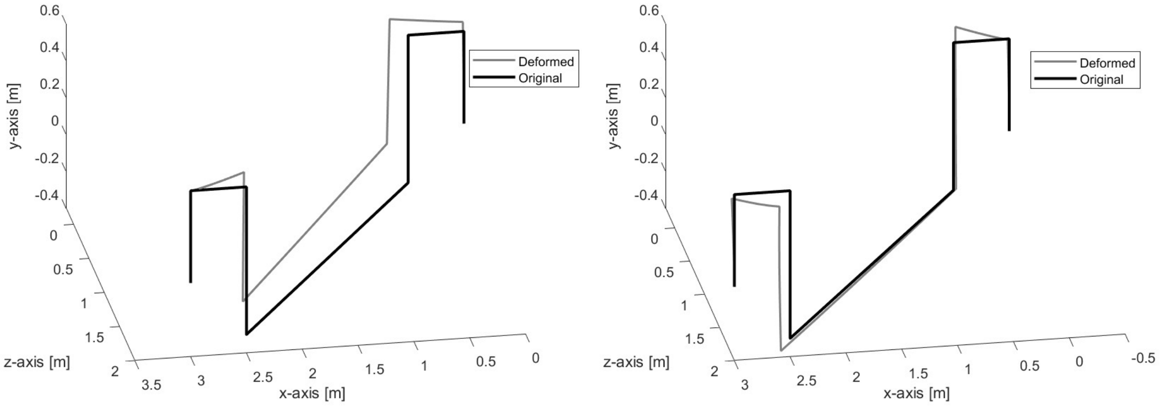

***(a)** Mode 1* ***(b)** Mode 2*

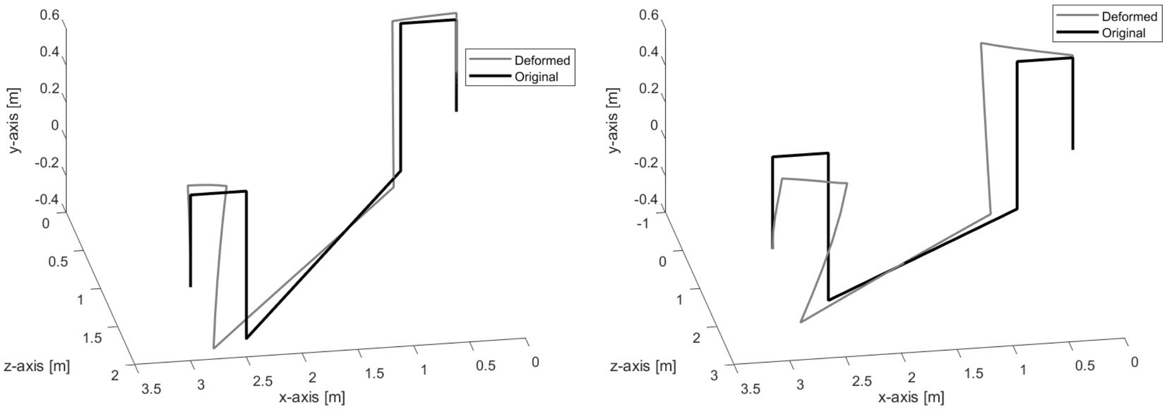

***(c)** Mode 3* ***(d)** Mode 4*

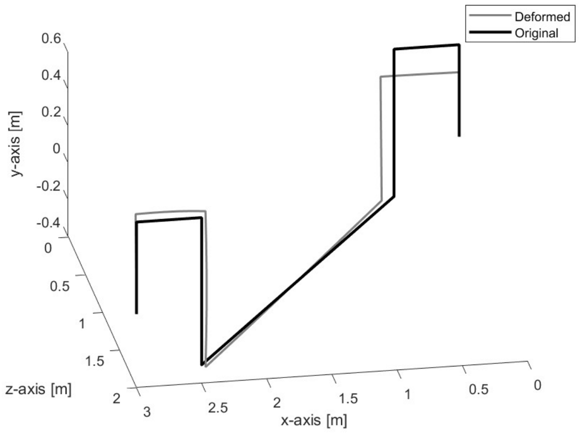

***(e)** Mode 5*

Figure A.2: *The first five mode shapes of the submerged Z-shaped multi-planar jumper, simulated with MATLAB*

Appendix B

MATLAB script

Listing B.1: *Matlab code for the submerged straight pipe*

```
%Two straight pipes connected with a 90 deg bend

clear all

%Chose number of elements per local pipe
nElm = 20;

%Chose number of eigenvalues and mode shapes to calculate
k = 10;

%Chose plotted mode shape
ModeShapeNr = 1;

% Scale the displacements
scale_factor = 1;

%Input properties
E = 206e9; %Pa
rho_p = 7850; %kg/m^3
D = 0.052; %m
```

```
t = 0.002; %m
v = 0.3;
%G = 2.61e10; %Pa

%Lengts of the Z—haped multiplanar jumper
Lengths = [0 0.5 0.5 0.8 2 0.8 0.5 0.5]; %[m]
%Bends about z axis
alpha = [0 90 0 —90 0 90 0 —90]; %[deg]
%Bends about y axis
beta = [0 0 0 0 90 0 0 0]; %[deg]
%Bends about x axis
%gamma = [0 0 0 0 0 0 0 0]; %[deg]

%Lengts of the nonsymmetrical multiplanar jumper
%Lengths = [0 20 7 20 31 7 7 13.4 13 7 2.286]; %[m]
%Bends about z axis
%alpha = [0 90 0 —90 0 0 90 0 90 0 —90]; %[deg]
%Bends about y axis
%beta = [0 0 0 0 0 90 0 —90 0 45 0]; %[deg]
%Bends about x axis
%gamma = [0 0 0 0 0 0 0 0 0 0 0]; %[deg]

%Geometry of the S—shaped jumper
%Lengths = [0 3 14.5 5 15.4 2]; %[m]
%alpha = [0 90 0 —90 0 —90]; %[deg]
%beta = [0 0 0 0 0 0]; %[deg]
%gamma = [0 0 0 0 0 0]; %[deg]

%Geometry of the M—shaped jumper
%Lengths = [0 1.495 1 2.323 4.327 2.323 1 1.495]; %[m]
%alpha = [0 0 90 180 90 0 90 180]; %[deg]
%beta = [0 0 0 0 0 0 0 0]; %[deg]
```

```
%gamma = [0 0 0 0 0 0 0 0]; %[deg]

L_tot = sum(Lengths);

%Number of element and node calculations
nNodes = nElm + 1;
nDof = nNodes*6;

nElm_tot = nElm * (length(Lengths)-1);
nNodes_tot = nElm_tot + 1;
nDof_tot = nNodes_tot*6;

%Geometric calculations
d = D-2*t;
A = pi/4 * (D^2-d^2);
Vol = A * L_tot;
m_tot = rho_p * Vol;
L = L_tot / (nElm_tot);
m = m_tot / L_tot;
I_y = pi/64*(D^4-d^4);
I_z = I_y;
J = I_y + I_z;
G = E/(2*(1+v));
%v = E/(2*G)-1;

%Added Mass
rho_f = 1000; %[kg/m^3]
m_added_mass = rho_f*pi*(D^2)/4*L_tot;
rho_new = (m_tot + m_added_mass) / Vol;

% Start and end coordinates of each local pipe
xCoord = cumsum(Lengths .* cosd(alpha));
```

```
yCoord = cumsum(Lengths .* sind(alpha));
zCoord = cumsum(Lengths .* sind(beta));

% Making a coordiates matrix for the plot
Coord = zeros(nElm * (length(Lengths) - 1) + 1, 3);
for i = 1:length(Lengths)-1
    dx = (xCoord(i+1) - xCoord(i)) / nElm;
    dy = (yCoord(i+1) - yCoord(i)) / nElm;
    dz = (zCoord(i+1) - zCoord(i)) / nElm;

    startIdx = (i - 1) * nElm + 1;
    endIdx = i * nElm;

    Coord(startIdx:endIdx, 1) = dx * (0:nElm-1) + xCoord(i);
    Coord(startIdx:endIdx, 2) = dy * (0:nElm-1) + yCoord(i);
    Coord(startIdx:endIdx, 3) = dz * (0:nElm-1) + zCoord(i);
end

Coord(end, :) = [xCoord(end), yCoord(end), zCoord(end)];

%Local Element Mass Matrix
M_11 = [1/3 0 0 0 0 0;
        0 13/35+6*I_y/(5*A*L^2) 0 0 0 11*L/210+I_y/(10*A*L);
        0 0 13/35+6*I_y/(5*A*L^2) 0 -11*L/210-I_y/(10*A*L) 0;
        0 0 0 J/(3*A) 0 0;
        0 0 -11*L/210-I_y/(10*A*L) 0 L^2/105+2*I_y/(15*A) 0;
        0 11*L/210+I_y/(10*A*L) 0 0 0 L^2/105+2*I_y/(15*A)];

M_21 = [1/6 0 0 0 0 0;
        0 9/70-6*I_z/(5*A*L^2) 0 0 0 13*L/420-I_z/(10*A*L);
        0 0 9/70-6*I_z/(5*A*L^2) 0 -13*L/420+I_z/(10*A*L) 0;
        0 0 0 J/(6*A) 0 0;
```

```
        0 0 13*L/420—I_z/(10*A*L) 0 —L^2/140—I_y/(30*A) 0;
        0 —13*L/420+I_z/(10*A*L) 0 0 0 —L^2/140—I_y/(30*A)];

M_22 = [1/3 0 0 0 0 0;
        0 13/35+6*I_y/(5*A*L^2) 0 0 0 —11*L/210—I_y/(10*A*L);
        0 0 13/35+6*I_y/(5*A*L^2) 0 11*L/210+I_y/(10*A*L) 0;
        0 0 0 J/(3*A) 0 0;
        0 0 11*L/210+I_y/(10*A*L) 0 L^2/105+2*I_y/(15*A) 0;
        0 —11*L/210—I_y/(10*A*L) 0 0 0 L^2/105+2*I_y/(15*A)];


M_12 = transpose(M_21);

Me_pipe = (rho_p*A*L) * [M_11 M_12; M_21 M_22];

%Lumped added mass matrix
Me_added = rho_new*A*L/2*[M_11 M_12; M_21 M_22];
Me_added(4,4) = 0;
Me_added(10,4) = 0;
Me_added(10,10) = 0;
Me_added(4,10) = 0;

Me = Me_pipe + Me_added;

r_g = sqrt(I_y/A); %Raduis of gyration
Theta = 24*(1+v)*(r_g/L)^2;

%Local Element Stiffness Matrix
K_11 = [E*A/L 0 0 0 0 0;
        0 12*E*I_z/(L^3*(1+Theta)) 0 0 0 6*E*I_z/(L^2*(1+Theta));
        0 0 12*E*I_y/(L^3*(1+Theta)) 0 —6*E*I_y/(L^2*(1+Theta)) 0;
        0 0 0 G*J/L 0 0;
```

```
        0 0 -6*E*I_y/(L^2*(1+Theta)) 0 (4+Theta)*E*I_y/(L*(1+Theta)) 0;
        0 6*E*I_z/(L^2*(1+Theta)) 0 0 0 (4+Theta)*E*I_z/(L*(1+Theta))];

K_22 = [E*A/L 0 0 0 0 0;
        0 12*E*I_z/(L^3*(1+Theta)) 0 0 0 -6*E*I_z/(L^2*(1+Theta));
        0 0 12*E*I_y/(L^3*(1+Theta)) 0 6*E*I_y/(L^2*(1+Theta)) 0;
        0 0 0 G*J/L 0 0;
        0 0 6*E*I_y/(L^2*(1+Theta)) 0 (4+Theta)*E*I_y/(L*(1+Theta)) 0;
        0 -6*E*I_z/(L^2*(1+Theta)) 0 0 0 (4+Theta)*E*I_z/(L*(1+Theta))];

K_21 = [-E*A/L 0 0 0 0 0;
        0 -12*E*I_z/(L^3*(1+Theta)) 0 0 0 -6*E*I_z/(L^2*(1+Theta));
        0 0 -12*E*I_y/(L^3*(1+Theta)) 0 6*E*I_y/(L^2*(1+Theta)) 0;
        0 0 0 -G*J/L 0 0;
        0 0 -6*E*I_y/(L^2*(1+Theta)) 0 (2-Theta)*E*I_y/(L*(1+Theta)) 0;
        0 6*E*I_z/(L^2*(1+Theta)) 0 0 0 (2-Theta)*E*I_z/(L*(1+Theta))];

K_12 = transpose(K_21);

Ke = [K_11 K_12; K_21 K_22];

% Transformation Matrix
for i = 1:length(Lengths)-1
    % Rotation about z-axis
    Te_z = [cosd(alpha(i)) -sind(alpha(i)) 0; sind(alpha(i)) cosd(alpha(i)) 0; 0 0 1];

    % Rotation about y-axis
    Te_y = [cosd(beta(i)) 0 sind(beta(i)); 0 1 0; -sind(beta(i)) 0 cosd(beta(i))];

    % Rotation about x-axis
```

```
    Te_x = [1 0 0; 0 cosd(gamma(i)) -sind(gamma(i)); 0 sind(gamma(i)) cosd(gamma(i))];

    % Combined transformation matrix
    Te = Te_z * Te_y * Te_x;

    T{i} = blkdiag(Te, Te, Te, Te);

    % Rotated Matrices
    K_t{i} = transpose(T{i}) * Ke * T{i};
    M_t{i} = transpose(T{i}) * Me * T{i};
end

%Assembly of global matrices
K(nDof_tot,nDof_tot)=0.0;
M(nDof_tot,nDof_tot)=0.0;

p=0;
q=0;
s=1;

for ne=1:length(Lengths)-1
    for pe=1:nElm
        for ii=1:12
            for jj=1:12
                K(p+ii,q+jj) = K(p+ii,q+jj) + K_t{1,s}(ii,jj);
                M(p+ii,q+jj) = M(p+ii,q+jj) + M_t{1,s}(ii,jj);
            end
        end
        p=p+6;
        q=q+6;
    end
```

```
    s=s+1;
end

%Boundary Conditions
for i = 1:6
   K(i,i)=1e30;
   K(nDof_tot-i+1,nDof_tot-i+1)=1e30;
end

%Calculating eigenvalues
[eigenvectors,eigenvalues] = eigs(K,M,k,'smallestabs');   %eigs works better for sparse matrices

fprintf('Natural frequencies [Hz]: \n')
frequencies = sqrt(diag(eigenvalues)) / (2*pi);
disp(frequencies)

for i=1:nNodes_tot

    % plot the corresponding disp.
    k1=1+(i-1)*6;
    k2=2+(i-1)*6;
    k3=3+(i-1)*6;

    for j=1:k
        X(i,j)=eigenvectors(k1,j); % extract x-component of nodal displacements
        Y(i,j)=eigenvectors(k2,j); % extract y-component of nodal displacements
        Z(i,j)=eigenvectors(k3,j); % extract z-component of nodal displacements
    end
```

```
end

% Scale the displacements
X = X * scale_factor;
Y = Y * scale_factor;
Z = Z * scale_factor;

% Modal displacement vector for the desired mode
deformed_y = Coord(:,1) + X(:, ModeShapeNr);  % calculate x-coordinate of
    deformed nodes
deformed_x = Coord(:,2) + Y(:, ModeShapeNr);  % calculate y-coordinate of
    deformed nodes
deformed_z = Coord(:,3) + Z(:, ModeShapeNr);  % calculate z-coordinate of
    deformed nodes

plot3(deformed_z, deformed_y, deformed_x, 'color', [.5 .5 .5],'LineWidth'
    ,1.5)
hold on
plot3(Coord(:,3), Coord(:,1), Coord(:,2), 'k', 'LineWidth', 2)
%xlim([-0.5 0.5])
%zlim([-20,20])
legend({'Deformed', 'Original'},'Location','northeast')
xlabel('x-axis [m]')
ylabel('z-axis [m]')
zlabel('y-axis [m]')

view([95 -35])
```